



PHD-THESIS

---

# Photonic Pressure Measurement

---

**Author:**  
André Kussicke

**Supervisor:**  
Matthias Bernien  
**Second Examiner:**  
Wolfgang Kuch

Date of submission: xx.xx.2022

# Contents

<b>1</b>	<b>Introduction and motivation</b>	<b>3</b>
1.1	QuantumPascal project . . . . .	3
1.2	Pressure standards at the PTB . . . . .	4
1.3	Development of photon based methods at the PTB . . . . .	6
<b>2</b>	<b>Theory part I: Absorption spectroscopy</b>	<b>8</b>
2.1	Absorbtion . . . . .	8
2.1.1	Lambert-Beer law . . . . .	8
2.1.2	Infrared spectroscopy . . . . .	9
2.1.3	Rotation spectra . . . . .	9
2.1.4	Vibration spectra . . . . .	11
2.1.5	Rotational and vibrational spectra . . . . .	13
2.1.6	HITRAN database . . . . .	14
2.2	Spectral line shapes . . . . .	15
2.2.1	Natural line broadening . . . . .	15
2.2.2	Temperature dependent line broadening . . . . .	16
2.2.3	Pressure dependent line broadening and line shift . . . . .	17
2.2.4	Combined effects . . . . .	19
2.3	Multipass absorption cells . . . . .	20
2.3.1	White cell . . . . .	20
2.3.2	Herriott-cell . . . . .	21
2.4	Quantum cascade lasers . . . . .	24
<b>3</b>	<b>Theory part II: Refractometry</b>	<b>27</b>
3.1	Ideal and real gases . . . . .	27
3.2	Lorentz Lorenz equation . . . . .	28
3.3	Refractometry . . . . .	29
3.3.1	Dual Farby-Pérot cavity based refractometry . . . . .	30
<b>4</b>	<b>Theory part III: Optical resonators</b>	<b>31</b>
4.1	Fabry-Pérot resonators . . . . .	31
4.1.1	Longitudinal resonator modes . . . . .	31
4.1.2	Gaussian Beam propagation . . . . .	34
4.1.3	Transversal Resonator modes . . . . .	34
4.1.4	Mode-matching . . . . .	36
4.2	Laser-frequency stabilization . . . . .	38
4.2.1	Lock-In technique . . . . .	38
4.2.2	Pound-Drever-Hall procedure . . . . .	38

---

<b>5 Absorption spectroscopy</b>	<b>39</b>
5.1 Laser characterization . . . . .	42
5.1.1 Laser tuning range . . . . .	43
5.1.2 Absolute emission frequency . . . . .	44
5.2 Determination of the required Laser linewidth . . . . .	47
5.3 Reducing Laser-linewidths and Laser locking . . . . .	51
5.4 Frequency calibration . . . . .	53
5.5 Temperature assessment . . . . .	56
5.6 Pressure assessment . . . . .	57
5.6.1 Thermal transpiration effects . . . . .	58
5.7 TDLAS measurements . . . . .	59
5.7.1 Pressure dependent transmission and absorption signals . . . . .	59
5.7.2 Comparison with simulation and fitting models . . . . .	60
5.7.3 Carbon monoxide line strengths . . . . .	63
5.8 TDLAS as a pressure standard . . . . .	66
5.8.1 Outlook and improvements . . . . .	67
<b>6 Refractometry</b>	<b>68</b>
6.1 Experimental setup: Refractometer . . . . .	68
6.1.1 Optics and electronics . . . . .	68
6.1.2 Vacuum system . . . . .	71
6.2 Resonator choice . . . . .	72
6.2.1 Measurement of the coefficient of thermal expansion (CTE) . . . . .	73
6.3 GAMOR method . . . . .	75
6.4 Free-Spectral-Range of the Invar resonator . . . . .	78
6.5 Temperature and pressure assessment . . . . .	80
6.6 Refractivities of Helium, Nitrogen and Argon . . . . .	82
6.7 Pressure induced cavity deformation . . . . .	84
6.7.1 Deformation of a specific cavity with COMSOL . . . . .	84
6.7.2 Experimental determination of the deformation . . . . .	88
6.8 Temperature effects: PV-work . . . . .	90
6.9 Ring comparison . . . . .	93
<b>7 Gas permeability measurements of cavity-spacer materials</b>	<b>96</b>
7.1 Theory . . . . .	96
7.2 Experimental setup and procedure . . . . .	97
7.2.1 Sample preparation . . . . .	98
7.3 Experimental results . . . . .	98

# 1. Introduction and motivation

The introducing chapter of this thesis is dedicated to impart an overview of vacuum metrology and the current state of the art when it comes to mechanical pressure standards in the vacuum region. With the prospect of photon based alternatives, the project and thesis goals are discussed.

## 1.1 QuantumPascal project

The QuantumPascal project is a joint research project of eleven European metrological institutes and one industrial partner (See Fig. 1.1). The idea of the project is to develop new photon-based methods to measure gas pressures precisely and thereby counteract the decade long stagnation in improving the widely used mechanical counterparts like piston gauges or mercury manometers.

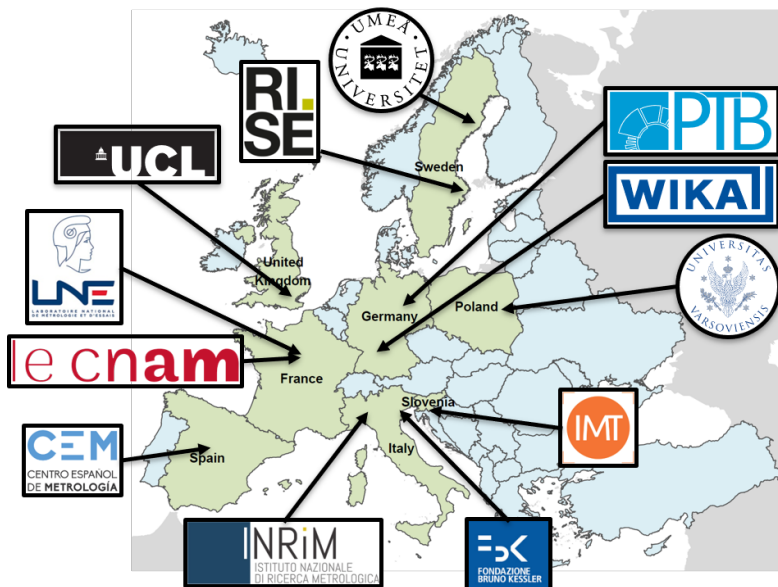


Figure 1.1: Shown are all participating institutes, universities and companies of the QuantumPascal project. Each partner focusses either on developing new photonic pressure standards or calculating relevant theoretical gas properties.

By developing new quantum based pressure standards and calculating the required thermodynamic and electromagnetic gas properties, the project seeks to pave the way towards a quantum-based realisation of the pascal via the ideal or real gas law. The gas pressure is then accessed with gas

density measurements opposed to the classical way of determining the pressure mechanically by measuring the force that acts on a defined area.

$$P = \frac{F}{A} \xrightarrow[\text{change}]{\text{System}} P = \rho k_B T \quad (1.1)$$

Many industrial sectors, like the semiconductor industry, greatly benefit from improved gas-pressure measurements within their production routine. The required measurement device calibration is ultimately provided by the respective national metrological institute. But also other applications, like the scientific backtracing of greenhouse gases, can advance in accuracy and diversity if new and improved gas density measurement systems are created. Switching from mechanical pressure standards to photon based standards is justified by a chain of arguments which evolve around the outstanding potential to improve the overall measurement uncertainties. With the new definition of the SI-system in May 2019 many natural constants, like the Boltzmann constant  $k_b$ , were assigned an uncertainty of zero. Since most photonic methods measure gas densities that are related to gas pressure via the ideal or real gas law, the new definition of the SI-system also benefits optical gas pressure measurements. The recent advancement in Laser technology also justifies a change from mechanical to optical standards. On one hand the development of quantum cascade lasers in 1994 by J. Faist et al [24] created a vast amount of Laser sources in the molecular fingerprint region of the EM-spectrum. Thus allowing the construction of partial pressure standards for virtually any gas of the region when absorption spectroscopy is used as a primary measurement technique. On the other hand the frequency of laser light can be stabilized with an uncertainty of up to  $\delta\nu = 10^{-17}$  [28]. But also other relevant optical properties apart from the frequency of light have been theoretically determined with excellent uncertainties. One important example is the refractivity of helium which is known with a relative uncertainty of  $10^{-6}$  and therefore makes refractivity measurements an outstanding candidate for new gas pressure standards.

## 1.2 Pressure standards at the PTB

The PTB (Physikalisch-Technische-Bundesanstalt) is the national metrology institute of Germany. The working groups 3.33 ("Pressure") and 7.54 ("Vacuum metrology") currently realize the pressure scale from atmospheric pressure up to the ultra high vacuum region with different mechanical pressure standards. Four different methods and their respective relative uncertainties are shown in Fig. 1.2.

A **mercury manometer** is used to determine the pressure difference  $P_1 - P_2$  that is present between the two surfaces of a mercury filled, U-shaped tube. The height difference of the two liquid columns can be measured precisely with interferometric methods and is directly proportional to the applied pressure difference  $\Delta P$ :

$$\Delta P = \rho \cdot g \cdot h \quad (1.2)$$

with the gravitational constant  $g$  and  $\rho$  the density of mercury. The manometer can be used for pressure measurements from atmospheric pressure down to 100 Pa. The relative uncertainty of the mercury manometer surpasses most other gauges and goes as low as  $10^{-6}$  at atmospheric pressure. The pressure balance is only limited by the density measurement of mercury and the temperature stability of the tube.

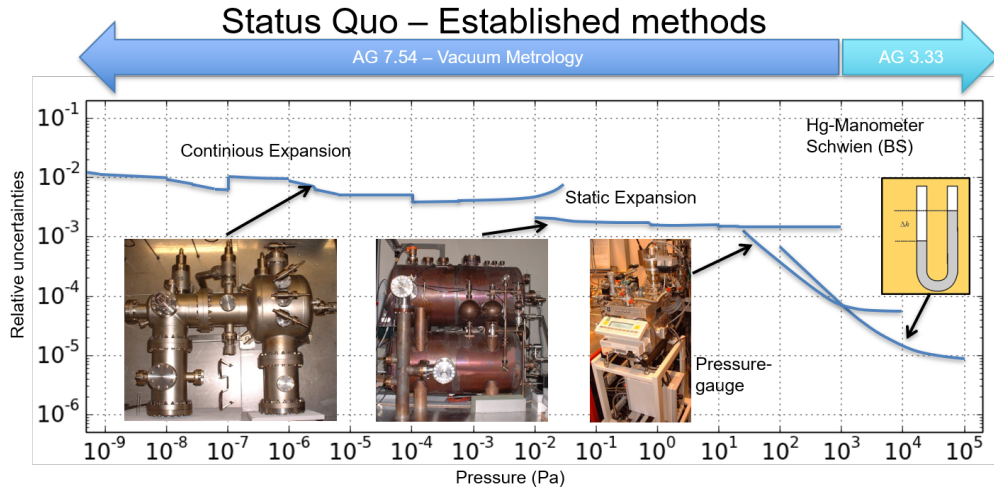


Figure 1.2: Shown are the mechanical pressure standards which are used by the PTB with their respective relative uncertainties, aswell as the vacuum range they cover. Graphic taken from [50].

A **pressure gauge** is a primary pressure standard that can generate a gas pressure between 10 Pa and 10 kPa. To generate the pressure, a well known rotating piston is positioned inside a tightly fitted tube. One surface of the piston is directly in contact with the measurement gas while the second cross sectional surface of the piston is en-capsulated in an evacuated glass bell. Once the downwards acting weight force of the piston equals the pressure that the gas asserts on the surface area of the piston, a well defined pressure difference  $P_1 - P_2$  is created between the two sides of the piston. Since the pressure  $P_1$  on the encapsulated side is known, e.g. by calibration with a mercury manometer, the piston gauge can be used to calibrate commercially available pressure measurement devices. The relative uncertainties of a piston gauge go as low as  $10^{-5}$  but require precise alignment of the piston since additional frictional or electrical forces have to be avoided.

The **static expansion** is a primary pressure standard that can generate gas pressures between  $10^{-2}$  Pa and 1 kPa. The combined gas law:

$$\frac{P_1 \cdot V_1}{T_1} = \frac{P_2 \cdot V_2}{T_2} \quad (1.3)$$

is used to determine the target pressure  $P_1$ . This target pressure is experimentally generated by expanding a compressed gas at a pressure  $P_2$  from a well known small volume  $V_2$  into a large volume  $V_1$ . The relative uncertainty of the static expansion is in the order of  $10^{-3}$  for most of the covered vacuum region. A limiting factor is often the temperature stability of the system, especially in the expansion chambers.

The **continuous expansion** is used in the high and ultra high vacuum region. The generated pressure is scaled down by continuously expanding the measurement gas into a vacuum pump via two precisely defined conductances. The first orifice connects the gas filled expansion chamber (with a pressure  $P_1$ ) with the measurement chamber, in which the target pressure  $P_2$  is going to be generated. The second orifice has a much larger conductance than the first one ( $C_2 \gg C_1$ ) and connects the measurement chamber with the vacuum pump ( $P_3$ ). A continuous flow is created and the pressure significantly decreases after each orifice. Under isothermal conditions

the flow through both conductances has to be equal. Since the expansion chamber is under high pressure ( $P_1 \gg P_2 \gg P_3$ ) it follows a simple formula to determine the target pressure  $P_2$  in the measurement chamber [33].

$$(P_1 - P_2)C_1 = (P_2 - P_3)C_2 \xrightarrow[\substack{\text{with} \\ P_1 \gg P_2 \gg P_3}]{} P_2 = P_1 \frac{C_1}{C_2} \quad (1.4)$$

By choosing a reasonable combination of orifices, the continuous expansion can generate UHV pressures up to  $10^{-9}$  Pa and achieve relative uncertainties between  $10^{-2}$  and  $10^{-3}$ . Limiting factors of the method are the gas dependant leak rate of the very small conductance ( $C_1$ ) as well as temperature stability of the system.

All four methods full fill the requirements of a well designed pressure standard: The pressure can be determined from a simple physical context, allowing high control of potential error sources and thus benefiting repeatability and overall performance.

### 1.3 Development of photon based methods at the PTB

The newly founded working group 7.55 ("Photonic pressure measurements") is dedicated to developing new pressure standards within the QuantumPascal project. Two independent systems are developed, both with promising prospects regarding the overall measurement uncertainty of pressure measurements. Figure 1.3 shows an uncertainty comparison of the existing mechanical pressure standards (in blue) and a selection of photonic pressure standards (in red). The relative uncertainties of the quantum based methods are estimated based on existing setups at other metrology institutes and the green arrows indicate the potential of further decreasing those by improving the respective experimental setup. The absorption spectroscopy setup, as well as the refractometer will be developed and build at the PTB.

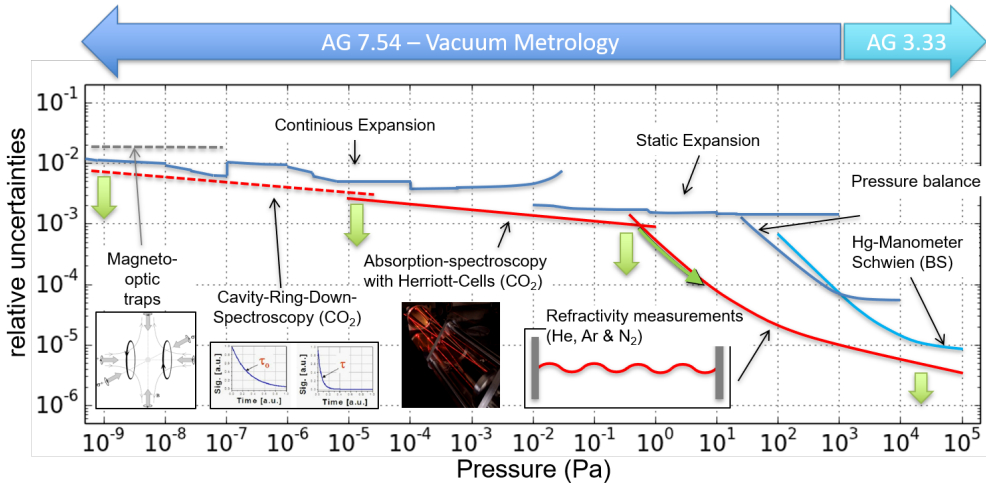


Figure 1.3: Comparison of the uncertainties of the established mechanical pressure standards at the PTB and the potential uncertainties of the new photonic pressure standards, of which some are being build during the QuantumPascal project by the AG 7.55. Image taken from [50].

A **refractometer** can be used as a photon based pressure standard. The operating principle

relies on the pressure dependent refractive index of gases, which can be measured using lasers. Therefore a Laser with the wavelength  $\lambda$  is locked to a gas filled resonator with a length  $L$ , so that the standing wave condition is fulfilled:

$$L = \frac{\lambda}{2 \cdot n} \cdot \text{integer} \quad (1.5)$$

The lock depends on the refractive index of the gas and to upkeep the standing wave inside the resonator, the laser wavelength has to be adjusted according to the pressure induced change in the refractivity. The laser frequency change  $\Delta f$  is proportional to the change in refractivity:

$$\frac{\Delta f}{f} \propto (n - 1) \quad (1.6)$$

This simple correlation can be combined with the Lorentz-Lorenz equation to determine the density of the gas.

$$\rho = \frac{3 \cdot \epsilon_0}{\alpha} \cdot \frac{n^2 - 1}{n^2 + 2} \quad (1.7)$$

Once the gas density is obtained, the pressure of the gas filled resonator can be calculated using the ideal or real gas law. Potentially problematic are the temperature stability of the system, the gas purity and the length stability of the resonator.

An **absorption spectroscopy** setup can be combined with an optical multipass cell to form an effective pressure standard. The Lambert Beer law of absorption describes how much light intensity is absorbed by a medium, in this case a gas, after the light travelled through a fixed distance  $L$  of that medium.

$$I = I_0 \cdot e^{-\alpha \rho L} \Leftrightarrow \rho = -\ln(\frac{I}{I_0}) / (\alpha L) \quad (1.8)$$

The amount of remaining light intensity depends on the coefficient of absorption  $\alpha$  as well as the gas density  $\rho$ . Solving for the gas density and combining the Lambert-Beer law with the ideal gas law, makes absorption spectroscopy a promising new optical pressure standard. The challenges are to generate reasonably long optical path lengths to enable low gas density measurements in the high vacuum region as well as narrowing the linewidth of the commonly used quantum cascade lasers. This thesis is dedicated to developing, building and improving a fully automatic optical pressure standard at the PTB, by using absorption spectroscopy together with a multipass cell type which was designed by D.R Herriott in 1965.

## 2. Theory part I: Absorption spectroscopy

### 2.1 Absorbtion

#### 2.1.1 Lambert-Beer law

The Lambert-Beer law describes the intensity loss of a monochromatic electromagnetic wave which travels through an absorbing material. The fraction ( $dI$ ) of the total intensity ( $I$ ) that is lost while the radiation travels the distance  $dz$  in the optical media is given by:

$$dI(\nu) = -\alpha(\nu)I(\nu)dz \quad (2.1)$$

The coefficient  $\alpha(\nu)$  specifies the intensity fraction  $\frac{dI}{I}$  that is lost during the process. Assuming that extinction processes like scattering are negligible,  $\alpha(\nu)$  becomes the coefficient of absorbtion. Integrating (2.1) yields the Lambert-Beer:

$$I(\nu) = I_0(\nu) e^{-\alpha(\nu)z} \quad (2.2)$$

where  $I(\nu)$  is the intensity of the radiation that is transmitted through the absorbing material. The coefficient of absorbtion is proportional to the molecular density of the absorbing media:  $n$ . Therefore the Lambert-Beer law of absorbtion, for a single absorbtion line at the wavenumber  $\nu_0$ , is given by:

$$I(\nu) = I_0(\nu) e^{-\alpha(\nu-\nu_0)nz} \quad (2.3)$$

In the case of tuneable-diode-laser-absorption-spectroscopy (TDLAS), the frequency of the measurement laser is tuned over an isolated absorption line while the integrated absorbance  $A_{line}$ :

$$A_{line} = \int_{-\infty}^{+\infty} -\ln \left( \frac{I(\nu)}{I(\nu_0)} \right) d\nu \quad (2.4)$$

is measured with photosensitive detectors. The Lambert-Beer-Law of absorption is therefore often given in its frequency integrated variant to accommodate for the described measurement principle. Integrating over the absorption coefficient:  $\alpha(\nu - \nu_0)$  in the wave number domain yields the line strength  $S$  of the absorption line [42]:

$$S = \int_{-\infty}^{+\infty} \alpha(\nu - \nu_0) d\nu \quad (2.5)$$

which is commonly listed in databases like HITRAN to allow for an efficient comparison of individual spectroscopic measurements. With 2.4 and 2.5] the integrated absorption law in its logarithmic form can be written as:

$$A_{line} = S \cdot n \cdot z \quad (2.6)$$

The molar density  $n$  can be expressed by the ideal gas law leading to the final result:

$$A_{line} = S \frac{P}{k_B T} \cdot z \quad (2.7)$$

where  $P$  and  $T$  are the gas pressure and temperature.

### 2.1.2 Infrared spectroscopy

The infrared region of the electromagnetic spectrum is commonly separated into three individual sections. The near-infrared connects directly to the visible part of the spectrum and covers a large wavelength region from 800nm to  $2.5\mu\text{m}$ . The mid-infrared includes the so called molecular-fingerprint region, which contains a significant amount of molecular ro-vibrational transitions. The mid-infrared is therefore especially relevant for molecular spectroscopy applications and it spans the wavelength region from  $2.5\mu\text{m}$  to around  $10\mu\text{m}$ . The far-infrared connects the mid infrared and the microwave region, which begins at 1mm.

### 2.1.3 Rotation spectra

Diatom molecules with a permanent dipole moment, for example carbon monoxide or hydrogen fluoride, have a pure rotational spectrum. If these molecules are irradiated with microwaves, the photon energy can be absorbed and an electronic transition between rotational energy levels is induced. Assuming a rigid rotation, where the atoms oscillate around a common centre of mass, one can describe the energy levels and transition energies in quantum mechanical terms. The kinetic energy of a rotation is given by:

$$E_{rot} = \frac{1}{2} I \cdot \omega^2 = \frac{J^2}{2I} \quad (2.8)$$

with the oscillation frequency  $\omega$ , the angular momentum  $J$  and the moment of inertia  $I$ :

$$I = \frac{M_1 \cdot M_2}{M_1 + M_2} \cdot R^2 = M \cdot R^2 \quad (2.9)$$

where the respective atomic masses ( $M_1$  and  $M_2$ ), the reduced mass  $M$  and the distance between the atoms  $R$  are introduced. The angular momentum is quantized and eigenvalue equations can be applied for the absolute square of the operator.

$$\mathbf{J}^2 |m, j\rangle = \hbar^2 j(j+1) |m, j\rangle \text{ with } j = \{0, 1, 2, \dots\} \quad (2.10)$$

Hence the rotational energy can be rewritten as:

$$E_{rot} = \frac{\hbar^2 j(j+1)}{2M \cdot R^2} \quad (2.11)$$

The transition energy between two rotational levels  $E_j$  and  $E_{j+1}$  is then given by:

$$\Delta E = E_{j+1} - E_j = \frac{\hbar^2(j+1)}{M \cdot R^2} \quad (2.12)$$

The unit  $\text{cm}^{-1}$  is commonly used in spectroscopic applications since it is proportional to the photon energy and allows an intuitive and direct comparison of individual electromagnetic transitions.

Based on this idea, the equation 2.11 can be expressed in spectroscopic terms by deviding it by  $h \cdot c$ . The resulting energy levels are called term-values.

$$F_{rot} = \frac{E_{rot}}{h \cdot c} = B_e \cdot j(j+1)$$

$$B_e = \frac{\hbar^2}{2hcMR^2} \text{ in cm}^{-1} \quad (2.13)$$

The rotation constant  $B_e$  is molecule specific and depends on the respective molecular mass and nuclei distance of the atoms. The transition energy  $\Delta E$  of two adjacent rotational energy levels, increases linearly with the angular momentum quantum number  $j$  and the necessary photon energy is typically in the microwave region.

The centrifugal force that acts on the nuclei, while they are rotating around a common center of mass, induces an additional spatial separation of the cores. Thus the moment of inertia is increased and the total energy  $E_{rot}$  is lowered. The generated potential energy is similar to that of a tensioned spring and can be added to the total rotation energy (equation 2.13) as a correction factor. A detailed calculation is shown in [17]. The term-values, up to a quadratic order of  $J^2$ , become:

$$F_{rot} = B_e \cdot j(j+1) - C_e \cdot j^2(j+1)^2 + \dots$$

$$C_e = \frac{\hbar^3}{4\pi ckM^2R_e^6} \quad (2.14)$$

A second rotation constant  $C_e$  is introduced which depends on the spring-constant  $k$  and the equilibrium inter nuclear distance  $R_e$ . Figure 2.1 shows the rotational spectrum of carbon monoxide for the first ten angular momentum quantum numbers.

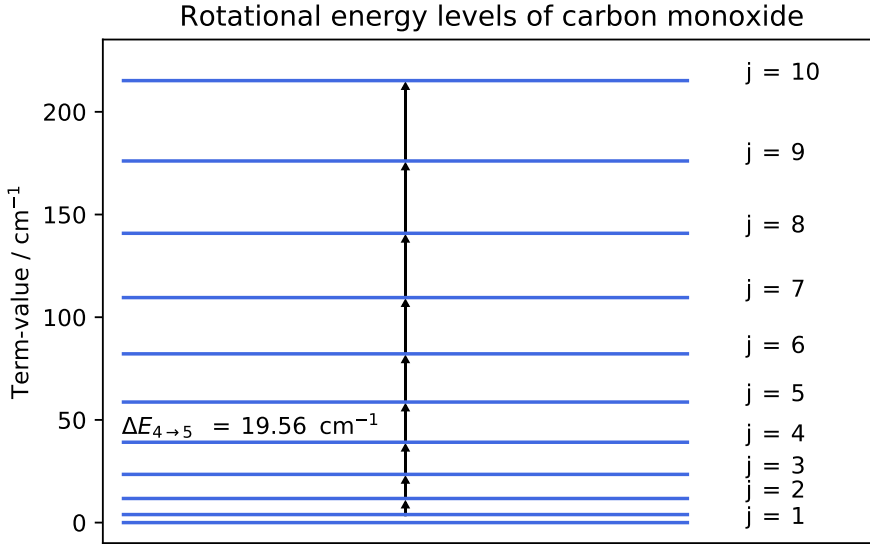


Figure 2.1: Shown are the rotational term-values of carbon monoxide for  $j = \{0, \dots, 10\}$ . The rotational constants  $B_e$  and  $C_e$  were calculated using the atomic masses of carbon and oxygen (12 and 16 atomic masses), an inter nuclear distance of 112 pm and an approximated spring constant of  $k = 2.3 \cdot 10^{-23} \frac{N}{m}$ .

### 2.1.4 Vibration spectra

The vibrational energy levels of molecules can be determined by solving the Schrödinger using the Born Oppenheimer approximation. The movement of the nuclei is slow compared to the electrons velocity, meaning that the electrons can adjust immediately to new nuclei distances. Resulting in minimal perturbation of the electrons by the nuclei. Based on this argument the electronic and nuclear wave-functions can be separated and solved individually.

$$\Psi_{\text{total}} = \Psi_{\text{nuclei}}(R_j) \cdot \Psi_{e^-}(r_j, R_j) \quad (2.15)$$

The vibration is carried out by the nuclei of the molecule and the respective Schrödinger equation, in center of mass coordinates, becomes:

$$\left( \frac{\hbar^2}{2M} \Delta^2 + E_{\text{pot}} \right) \cdot \Psi_{\text{nuclei}}(R) = E \cdot \Psi_{\text{nuclei}}(R) \quad (2.16)$$

A separation of variables (angle and radius) can be performed to determine the behavior of the radial nuclear wave function ( $S(R)$ ) and its energy eigenvalues.

$$\frac{1}{R^2} \frac{d}{dR} \left( R^2 \frac{dS}{dR} \right) + \frac{2M}{\hbar^2} (E - E_{\text{pot}} - E_{\text{rot}}) S = 0 \quad (2.17)$$

For a pure vibration the rotational energy  $E_{\text{rot}}$  (see eq. 2.11) is zero and the potential energy acting on the nuclei can be approximated with a Morse-potential:

$$E_{\text{pot}} = D_e \left( 1 - e^{-\alpha(R-R_e)} \right)^2 \quad (2.18)$$

with the bond-dissociation energy  $D_e$ , the equilibrium distance of the nuclei  $R_e$  and the constant  $\alpha = \sqrt{\frac{k_e}{D_e}}$  described by the force-constant  $k_e$ .

The Schrödinger equation can be solved analytically after inputting the Morse potential and the resulting energy eigenvalues and vibrational term-values are:

$$E_{vib} = \hbar\omega(\nu + \frac{1}{2}) - \frac{\hbar^2\omega^2}{4D_e}(\nu + \frac{1}{2})^2 \quad (2.19)$$

$$F_{vib} = \frac{E_{vib}}{\hbar \cdot c} = \omega_e(\nu + \frac{1}{2}) - \chi_e\omega_e(\nu + \frac{1}{2})^2 \quad (2.20)$$

During the calculation the vibrational quantum number  $\nu$  and the vibration frequency  $\omega$  have been introduced. With the dipole selection rule:  $\nu = \{0, \pm 1, \pm 2, \dots\}$  one can determine the transition energies of two adjacent vibrational energy levels:

$$\Delta F = \frac{\Delta E}{h \cdot c} = \omega_e - 2\omega_e\chi(\nu + 1) \quad (2.21)$$

In contrast to the energy level splitting of the purely rotational spectra, the vibrational energy level distance  $\Delta F$  decreases in magnitude as the vibrational quantum number increases. Figure 2.2 shows the vibrational spectrum of carbon monoxide. The transition energies between two adjacent vibrational states are almost 2 orders of magnitude larger than those of two adjacent rotational energy levels (for  $j, \nu \leq 10$ ).

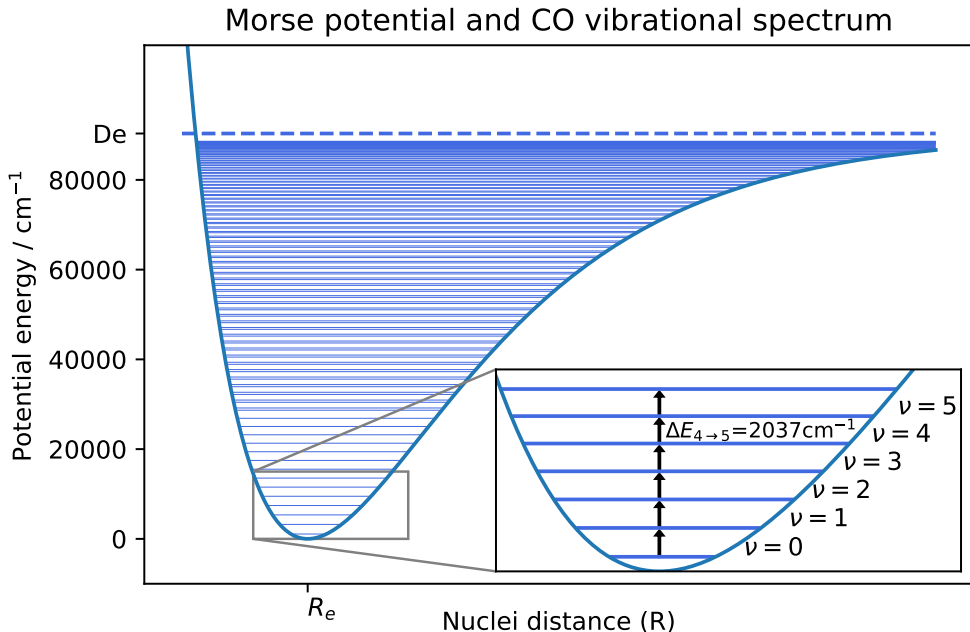


Figure 2.2: Shown is a Morse potential with several vibrational energy levels. The transition energy  $\Delta E$  decreases for increasing vibrational quantum numbers  $\nu$ . Vibrational energy levels beyond the dissociation energy  $D_e$  do not exist.

### 2.1.5 Rotational and vibrational spectra

Naturally, molecules rotate and vibrate simultaneously resulting in a combined ro-vibrational absorption spectrum. The term-values can be approximated by the total energy of the motion which is given by the sum of the rotation and the vibration energy of the molecule (eq. 2.20 and eq. 2.14):

$$\begin{aligned} E &= E_{rot} + E_{vib} \\ F &= \omega_e(\nu + \frac{1}{2}) - \chi_e \omega_e (\nu + \frac{1}{2})^2 + B_e \cdot j(j+1) - C_e \cdot j^2(j+1)^2 \end{aligned} \quad (2.22)$$

The ro-vibrational term-values are completely defined by the four molecular constants ( $\omega_e$ ,  $\chi_e$ ,  $B_e$  and  $C_e$ ) and the two quantum numbers  $\nu$  and  $j$ . The individual energy levels of the spectrum are separated into 3 branches, based on transition rules ( $\Delta j = 0, \pm 1$  and  $\Delta \nu = \pm 1$ ) and transition energies.

The **Q-branch** includes ro-vibrational transitions for which only the vibrational quantum number changes ( $\Delta \nu = \pm 1$ ), while the rotational quantum number remains the same ( $\Delta j = 0$ ). The photon energy, that is required to induce a Q-branch transition, is therefore identical to the respective vibrational term-values  $\Delta F_{vib}$ . (see eq. 2.21). Thus the Q-branch only consists of a single absorption line which is energetically located in between the P- and the R-branch transitions.

The **P-branch** transitions requires less energy than the Q-branch transition, since the rotational quantum number  $j$  changes by -1, resulting in an overall energy decrease.

The **R-branch** contains all ro-vibrational transitions, where the rotational quantum number is increased by +1 during the transition. The required energy is larger than the respective purely vibrational transition energy.

Figure 2.3 shows the rotational and vibrational term-values of carbon monoxide with an exemplary Q-, R- and P-branch transition.

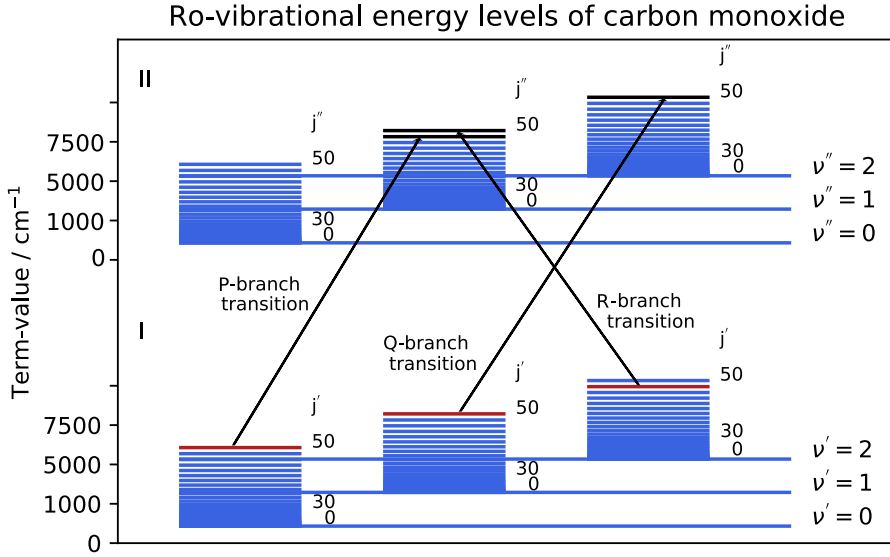


Figure 2.3: Shown are the ro-vibrational states I and II with their respective quantum numbers:  $j'$ ,  $\nu'$ , and  $j''$ ,  $\nu''$ . Three possible transitions are indicated with arrows and each can be related to one of the three branches respectively. The shown P-branch transition (with  $\Delta j_{(50 \rightarrow 49)} = -1$  and  $\Delta \nu_{(0 \rightarrow 1)} = +1$ ) requires less energy than the Q-branch transition (with  $\Delta j_{(50 \rightarrow 50)} = 0$  and  $\Delta \nu_{(1 \rightarrow 2)} = +1$ ) which is energetically equal to the pure vibrational transition with  $\Delta \nu_{(1 \rightarrow 2)} = +1$ . The R-branch transition (with  $\Delta j_{(49 \rightarrow 50)} = +1$  and  $\Delta \nu_{(2 \rightarrow 1)} = -1$ ) requires the highest energy.

### 2.1.6 HITRAN database

The high-resolution transmission molecular absorption database, short HITRAN, is a database that contains spectroscopic parameters of roughly 50 molecules and their respective isotopes. Some important parameters that are included for most absorption lines are: the central wavelength ( $\nu_{ij}$ ), the line strength (S), the self and air broadened linewidth ( $\gamma_{self}$  and  $\gamma_{air}$ ) and the pressure shift  $\delta_{air}$ . The database is updated continuously with the most recent and most accurate experimental results which were generated by various experimental setups e.g Fourier transform infrared spectroscopy but also other like cavity ring-down spectroscopy or tunable diode Laser absorption spectroscopy. The database is maintained by the Harvard and Smithsonian center for astrophysics and a publishable summary of the recent changes is disclosed every four years. With the most recent publication being submitted in 2016 [48]. Figure 2.4 shows an exemplaric absorption spectrum of CO and its isotopes in the mid infrared region, which was taken from the HITRAN database.

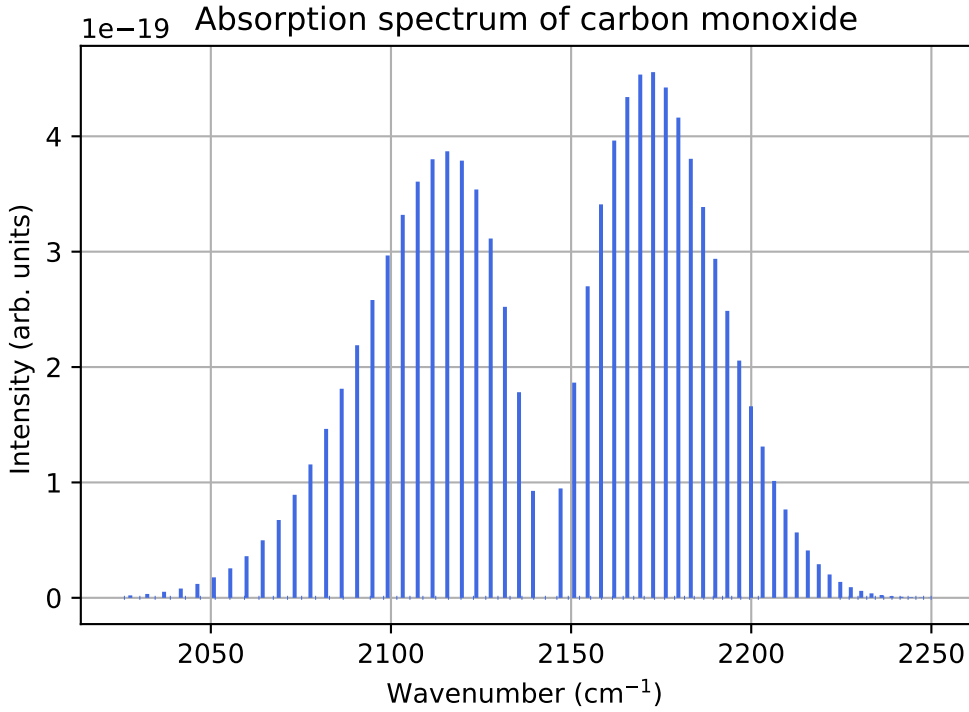


Figure 2.4: Shown are the P- and R-branch of CO in the mid infrared region. The data was taken from the HITRAN database [47] [48].

## 2.2 Spectral line shapes

Line shapes and especially line widths of radiating transitions are described by the full-width-half-maximum (FWHM) of the respective line shape function. The corresponding line shape function on the other hand can greatly depend on environmental influences such as temperature and pressure but it is also influenced by natural radiation characteristics of atoms.

### 2.2.1 Natural line broadening

The natural line width is the minimal finite linewidth that any spectral line has, independent of environmental influences. An excited atom or molecule that emits lights can be described in classical terms by a damped dipole oscillation and this damped radiation process is responsible for the existence of the natural line width.

In the classical model the oscillator has the mass  $m$  and the Eigenfrequency  $\omega_0 = \sqrt{d/m}$ , which is related to the spring constant  $d$ . Solving the differential equation of the damped harmonic oscillator:

$$\ddot{x} + \gamma\dot{x} + \omega_0^2 x = 0 \quad (2.23)$$

yields the solution for the time dependent behavior of the oscillation  $x(t)$ :

$$x(t) = x_0 e^{-\frac{\gamma t}{2}} (\cos(\omega t) + \frac{\gamma\omega}{2} \sin(\omega t)) \quad (2.24)$$

with the damping coefficient  $\gamma$  and the frequency  $\omega = \sqrt{\omega_0^2 - (\frac{\gamma}{2})^2}$ . In general  $\gamma \ll \omega_0$  holds true and 2.24 can be further simplified to:

$$x(t) \approx x_0 e^{-\frac{\gamma t}{2}} \cos(\omega_0 t) \quad (2.25)$$

The exponentially decreasing amplitude of the oscillation is responsible for a spectral broadening of the emitted light around the central frequency  $\omega_0$  and the Fourier-transformation of 2.25 will give rise about the exact spectral line shape of the observed electro-magnetic transition. The spectral amplitude  $A(\omega)$  is given by:

$$\begin{aligned} A(\omega) &= \frac{1}{\sqrt{2\pi}} \int_0^\infty x_0 e^{-\frac{\gamma t}{2}} \cos(\omega_0 t) e^{-i\omega t} dt \\ A(\omega) &= \frac{x_0}{\sqrt{8\pi}} \left( \frac{1}{i(\omega_0 - \omega) + \frac{\gamma}{2}} + \frac{1}{i(\omega_0 + \omega) + \frac{\gamma}{2}} \right) \\ A(\omega) &\approx \frac{x_0}{\sqrt{8\pi}} \left( \frac{1}{i(\omega_0 - \omega) + \frac{\gamma}{2}} \right), \text{ for } (\omega - \omega_0) \ll \omega_0 \end{aligned} \quad (2.26)$$

and it can be used to calculate the spectral intensity  $I(\omega)$ , which is proportional to  $|A(\omega)|^2$ .

$$I(\omega) \propto |A(\omega)|^2 = \frac{\gamma/2\pi}{(\omega - \omega_0)^2 + (\frac{\gamma}{2})^2} \quad (2.27)$$

The natural line shape function  $I(\omega)$  has a characteristic Lorentz shape and its FWHM is defined as the natural linewidth of the respective EM-transition. Due to the finite radiation time of the atoms, any absorption or emission line has a natural line width which is furthermore independent of any environmental influences.

The existence of the natural line width can also be explained using Heisenberg's uncertainty principle, where the energy uncertainty is rewritten as frequency uncertainty:

$$\Delta\nu \geq \frac{1}{2\pi\Delta t} \quad (2.28)$$

The principle in this form states, that the frequency uncertainty of a radiating transition between an excited state, with the energy  $E_i$  and the life time  $\tau_i = \Delta t$ , and the ground state will be greater than zero. Which is due to the fact that all excited states have finite life times. Radiating transitions between two excited states have greater natural line widths since their individual energy uncertainties are additive.

### 2.2.2 Temperature dependent line broadening

The natural line broadening is present for every radiative transition and is usually superimposed with additional line broadening effects. One additional effect is the temperature broadening (also called Doppler broadening) effect of a transition line. It is present for in many absorption and emission lines of gasses and usually dominates the pressure broadening effect at low pressure values.

Considering an ideal gas with radiating atoms, the gas-particles are generally moving with a velocity  $\vec{v} > 0$  while they emit light with the central frequency  $\omega_0$ . For a static observer

(i.e another atom) this movement results in a frequency shift of the incoming light due to the Doppler-effect:

$$\omega_{obs} = \omega_0 + \vec{k} \cdot \vec{v} \quad (2.29)$$

The same holds true for atoms which move with a velocity  $\vec{v}$  and absorb light during the movement. Their absorption frequency is shifted according to the Doppler-effect and only light with the frequency  $\omega = \omega_{obs}$  can induce the atomic transition.

If the system is in thermal equilibrium the gas-particle velocities can be described by the Maxwell-distribution. The density of absorbing gas-molecules which are in the atomic state  $E_i$  is then given accordingly by:

$$n_i(v_z)dv_z = \frac{N_i}{\sqrt{2k_b T/m}} e^{-(\frac{v_z}{\sqrt{2k_b T/m}})^2} dv_z \quad (2.30)$$

The spectral intensity  $I(\omega)$  is proportional to  $n(\omega)$ , which can be calculated by inserting 2.29 into 2.30. The calculation yields:

$$I(\omega) = I(\omega_0) e^{-\left(\frac{c(\omega-\omega_0)}{\omega_0 \sqrt{2k_b T/m}}\right)^2} \quad (2.31)$$

The resulting line shape is a Gaussian function with the corresponding Doppler broadened line width  $\Delta\omega = \frac{\omega_0}{c} \sqrt{(8k_b T \ln 2)/m}$ . In contrary to the natural line width, the Doppler line width depends on multiple environmental factors including the temperature, particle mass and the central frequency  $\omega_0$ .

### 2.2.3 Pressure dependent line broadening and line shift

If the atoms of a radiating gas are introduced to foreign gas molecules, their individual energy levels are shifted whenever the two species interact with each other. This energy shift greatly depends on the electrical properties of the two interacting particles and their distance  $R$  to each other. If one considers a radiating transition between the energy levels  $E_i$  and  $E_k$  of the host atoms, one can observe positive and negative energy shifts relative to the initial energy of the two states. This is due to the different types of electrostatic interactions between the native and the perturbing molecules. Van der Waals forces, generated by the interaction with the perturbing molecules, will result in a negative energy shift of  $E_i$  and  $E_k$ . While positive energy shifts are introduced by electrostatic repulsion. The distortion of the energy levels is usually greater for higher levels which results in a net change of the central transition frequency  $\nu_0$  [37]. The schematic potential curves of  $E_i$  and  $E_k$  are presented in Figure 2.5 for different values of  $R$  and the altered transition frequencies that are generated due to the quasi collision of the particles. If the system is in thermal equilibrium the relative core distances are distributed around a mean value  $R_m$ , which eventually results in the broadening of the transition line around a central transition frequency  $\nu_m$ .

In 1932 F. Weisskopf described the collision dependent line broadening and line shift in classical terms [60]. He considered a damped harmonic oscillator with an additional collision dependent damping constant. The collision of the two particles contributes to a phase change  $\Theta$  of the oscillating native gas particle. The phase change introduces a change of oscillation frequency while the atoms collide. This makes the frequency a time dependent variable. The waveform  $x(t)$  that describes the time dependent behavior of the collision damped oscillator is then given by:

$$x(t) = x_0 \cdot e^{-i \int_0^t \omega(t') dt'} \quad (2.32)$$

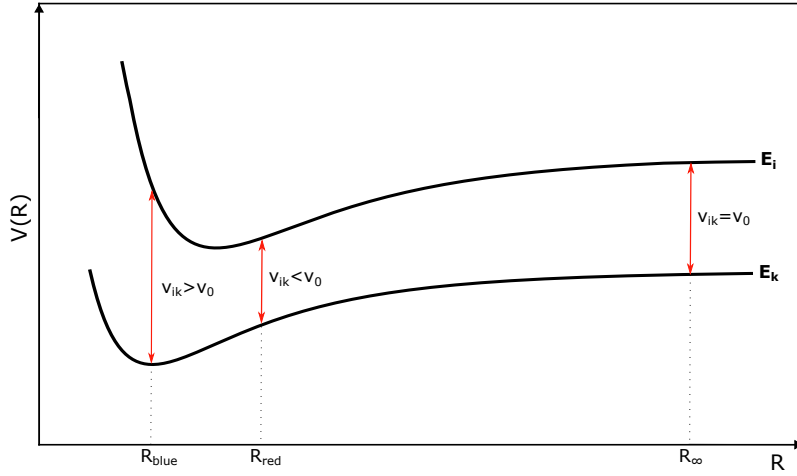


Figure 2.5: Shown are the (Lenard-Jones) potential-curves of the two energy levels  $E_i$  and  $E_k$  while they are subject to the perturbation of a foreign atom. If the atoms are reasonably separated (for  $R = R_\infty$ ) the transition frequency  $\nu_{ik}$  remains unchanged and is equal to  $\nu_0$ . In most cases the transition frequency is shifted to the red (for  $R = R_{red}$ ) while in rare occasions blue shifts are also present (for  $R = R_{blue}$ ).

A Fourier-transformation of eq: 2.32 yields the spectral amplitude  $A(\omega)$  and the squared absolute value of  $A(\omega)$  is proportional to the desired spectral line shape  $I(\omega)$ :

$$I(\omega)d\omega = \frac{2e^2\omega^4}{3c^3}\frac{1}{2\pi} \left| \int_{-\infty}^{\infty} x_0 \cdot e^{-i\int_0^t \omega(t')dt'} \cdot e^{i\omega t} dt \right|^2 d\omega \quad (2.33)$$

The prefactor in eq: 2.33 is determined classically from the radiation characteristics of an oscillating charge. Solving the integral yields the final Lorentzian-shaped result for the collision broadened line intensity  $I(\omega)$  :

$$I(\omega) = \frac{2\omega^4 e^2 x_0^2}{3\pi c^3} \cdot \frac{(1-A)/\tau_c}{((1-A)/\tau_c)^2 + (B/\tau_c - (\omega - \omega_0))^2} \quad (2.34)$$

with the factors A and B that describe the phase shifts which occur due to the collisions:  $A = \int_{-\infty}^{\infty} \rho(\Theta) \cos(\Theta) d\Theta$  and  $B = \int_{-\infty}^{\infty} \rho(\Theta) \sin(\Theta) d\Theta$ . The coefficient  $\rho(\theta) d\theta$  is the probability that a phase shift occurs within the phase interval  $\Delta\Theta = \Theta + d\Theta$  and  $\tau_c$  is the mean free time between collisions. The full calculation with an additional overview of the quantum mechanical approach for the problem is described in detail in [12].

The frequency shift  $\Delta\nu$  and the half-width  $\delta\nu$  are related to the coefficients A and B are given by:

$$\Delta\nu = \int_0^\infty \rho(\Theta) \cdot (1 - \cos(\Theta)) / \tau_c d\Theta \quad (2.35)$$

$$\delta\nu = \int_0^\infty \rho(\Theta) \cdot \sin(\Theta) / \tau_c d\Theta \quad (2.36)$$

Both, the line width and the line shift are proportional to the particle density. The function  $\frac{\rho(\Theta) d\Theta}{\tau_c}$  can be understood as the number of collisions during the mean free time  $\tau_c$ , which greatly depends on the gas density. The gas density on the other hand is related to the gas pressure and temperature via the ideal gas law, which is the reason why the collision broadening is often called pressure broadening.

#### 2.2.4 Combined effects

Under realistic measurement conditions (e.g at room temperature and atmospheric pressure), the actual spectral line shape will be influenced by the temperature and pressure simultaneously. The line shape function can then be described by a Voigt-profile to accommodate for both effects. A Voigt profile results from the convolution of a Gaussian and a Lorentzian function:

$$V(\omega, P, T) = G(\omega, T) * L(\omega, P) = \int_{-\infty}^{\infty} G(\tau, T) \cdot L(\omega - \tau, P) d\tau \quad (2.37)$$

Figure 2.6 shows a comparison of three previously described spectral line shape functions.

Although a Voigt profile is a good first approximation of the physical situation, it has become apparent over the last decades that it does not adequately describe the experimentally generated results. For a more detailed description one has to also consider the mutual interference of the Doppler and collision broadening, which both depend on the particle velocity. This can, for example, lead to a particle being

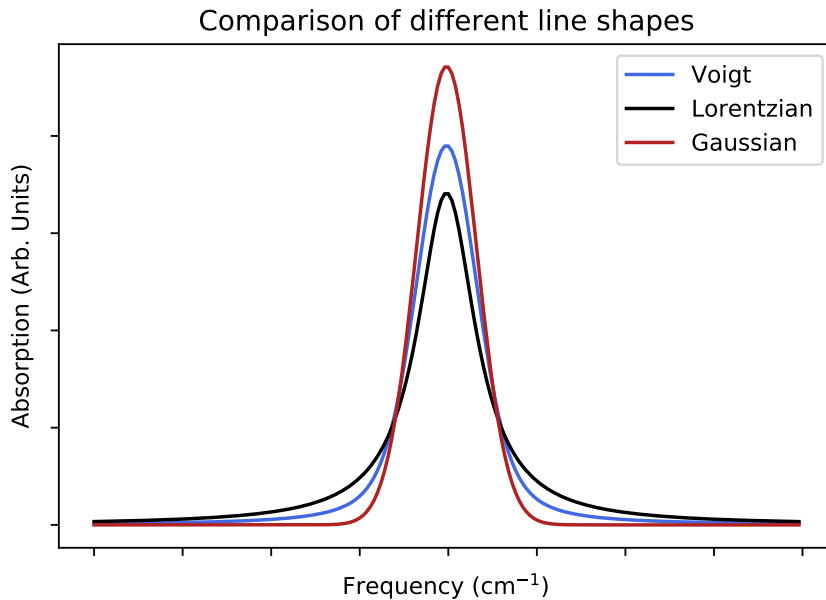


Figure 2.6: Shown are the Voigt-, Lorentzian- and Gaussian-spectral-line-shapes with area normalized profiles.

## 2.3 Multipass absorption cells

Multi pass absorption cells are used to increase the optical pathways within an absorption spectroscopy setup. While the light travels through the active medium more and more light intensity is lost due to absorption processes. To be able to detect low gas densities (eg of atmospheric greenhouse gases) one requires great optical path lengths since the two physical properties are inversely proportional to each other.

$$\rho = -\ln\left(\frac{I}{I_0}\right)/(\alpha \cdot L) \quad (2.38)$$

There are many different types of multipass absorption cells and their basic principle, as well as their main advantages and disadvantages are being discussed in the upcoming chapters.

### 2.3.1 White cell

The White cell was designed in 1942 by John U. White and consists of three spherical, concave mirrors [61]. Two adjacent mirrors ( $A_1$  and  $A_2$ ) are positioned opposite to a larger mirror  $B$ . The distance between the mirrors is equal to their radius of curvature. The light is reflected ( $n \cdot 4$ ) times within the White-cell. The integer number  $n$  can be increased or decreased by tilting the mirrors  $A_1$  and  $A_2$ . Thereby the position of the center of curvature, on the surface of mirror  $B$ , can be adjusted to allow fewer or additional reflections. The basic operating principle of the multi reflection cell is shown in 2.7 together with the individual center curvature which are indicated in a red circles. A white-cell is capable of achieving several meters of optical path length with a simple design that requires no significant alignment of the mirrors.

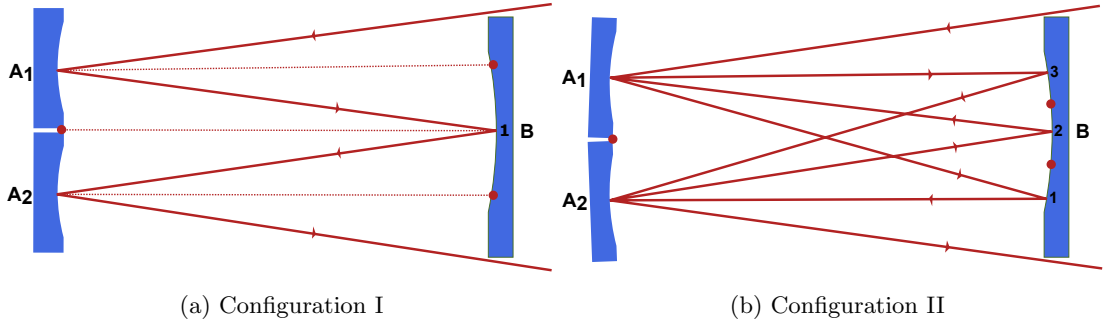


Figure 2.7: Shown is the basic operating principle of a White-cell, together with two possible configurations. **Configuration I:** The mirrors are close to parallel to each other and a total of four reflections are achieved. **Configuration II:** The mirrors  $A_1$  and  $A_2$  are slightly tilted to the center of mirror  $B$ . A total of twelve reflections are achieved in this arrangement. The reflection sequence is specified by arrows and an additional enumeration (1-3) on Mirror B.

### 2.3.2 Herriott-cell

Herriott-cells are another commonly used type of optical multipass cells. They were invented in 1965 by Donald R. Herriott and consist of two spherical mirrors with identical focal lengths. One of the mirror has a small hole, usually between 2 and 5 mm in diameter, which is utilized to couple Laser light into the cell. The light enters the cell, is reflected from both mirror surfaces and exits the multipass cell through the same hole under a different angle, which allows for a simple spatial separation of the in and out coupled laser rays. The number of reflections on each mirror and the overall optical path length, depend on the focal lengths of the mirrors and their distance D to each other. Path lengths between a couple centimeters and several hundred meters are possible, depending on the design of the Herriott-cell. Figure 2.8 shows the basic operating principle of a Herriott-Cell.

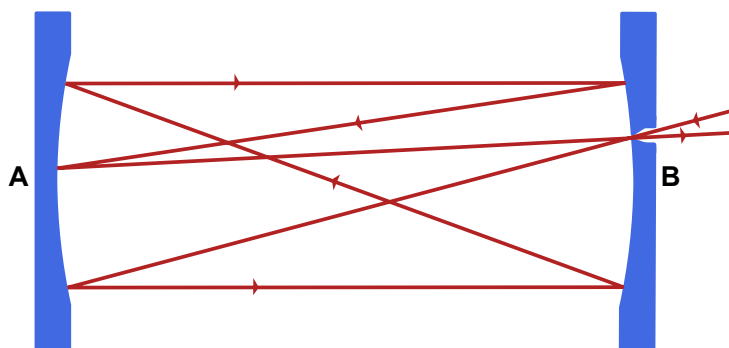


Figure 2.8: Shown is the basic design of a Herriott-Cell. The mirrors A and B have identical optical properties and the number of reflections on each mirror depends on the distance between the mirror and their radius of curvature.

Depending on the Laser's angle of incident and the distance between the mirrors, the spot pattern on the Herriott-cell mirrors are either elliptical or spherical. This allows for an exact geometrical calculation of the total optical path length, which is an important property for absorption processes. Fig2.9 introduces the necessary geometry to determine the total optical path length for a spherical spot pattern.

The "Top-View" shows the two spherical mirrors M1 and M2 in the x-z plane, which are positioned on the z-axis at a given distance D. The center of the coordinate system  $(x, y, z) = (0, 0, 0)$  is identical to the center of the spherical mirror containing the small hole used for in-coupling the laser into the cell. The hole is located at  $x_0 = r_S$ . The bold, purple and orange arrows show the Laser entering and leaving the Herriott-Cell and for a spherical spot pattern the beams are overlapping in the x-z plane.

The Front view on the right in Fig 2.9 shows the x-y plane and illustrates the directional change of the reflected Laser beams inside of the cell. The number of reflections are labeled from 0 to 2N and change in color between red and green depending on the mirror from which the last ray was reflected. For consecutive reflections (e.g from N=1 to N=2) the Laser beam ends on the same x-position at which the following reflection starts. The end-coordinates for the first reflection

are therefore labeled as  $x = r_{x1}$  and  $y = r_{y1}$  with  $rs^2 = r_{x1}^2 + r_{y1}^2$ . The overall initial and final reflections are again shown by the bold, purple and orange arrows. The last reflected laser beam (orange) leaves the Herriott-Cell at the same x-position at which the first one (purple) entered.

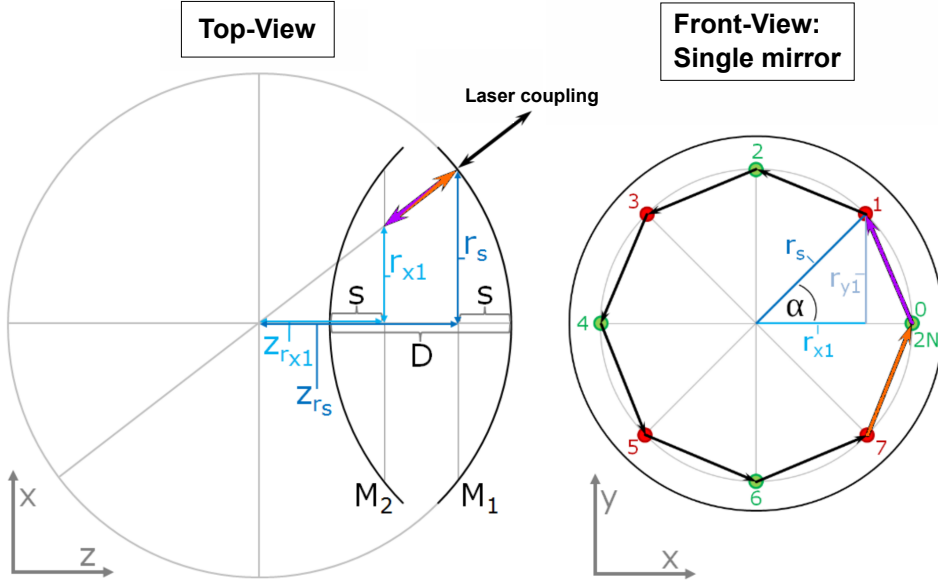


Figure 2.9: Shown on the left is the geometrical Top-view of a exemplaric Herriott-Cell configuration with a spherical spot pattern. On the right is the Front-view illustrating the directional change of the Laser beam after each reflection on the two mirrors.

The projection of the in- and out-coupled beam onto the x-z axis (Top-view in 2.9) shows, that for a spherical spot pattern, the respective beams must be overlapping in the respective plane. Assuming that the final beam is reflected on the mirror surface instead of leaving the cell through the hole, it would have to be reflected perpendicularly on the mirror surface to "re-enter" the Herriott Cell as the orange Laser Beam. Meaning that the in-coupled Laser beam always points to the center of the sphere or rather to the center of origin of the chosen coordinate system. This remains true even if the distance between the mirrors  $D$  is increased or decreased and results in an characteristic property of Herriott-Cells: for a spherical spot pattern one has to re-align only the y-component of the in-coupled beam, when the mirror distance is changed. Using this information one can calculate  $r_{x1}$  with the intercept theorem:

$$\frac{r_{x1}}{r_s} = \frac{z_{rx1}}{z_{rs}} \quad (2.39)$$

where  $z_{rx1}$  is the end position of the in-coupled, "purple" laser beam on the mirror without a hole and  $z_{rs}$  is the end position of the out-coupled, "orange" Laser beam on the mirror with the small hole. One can observe that:

$$z_{rx1} = R - D + s \quad \text{and} \quad z_{rs} = R - s \quad (2.40)$$

where  $s$  is the spatial depths of the mirror which depends on its radius of curvature and the spot pattern:

$$s = R - \sqrt{R^2 - r_s^2} \quad (2.41)$$

Equation 2.39 can then be rewritten as:

$$\begin{aligned}\frac{r_{x1}}{r_s} &= \frac{R - D + s}{R - s} \\ &= \frac{R - s + 2s - D}{R - s} \\ &= 1 + \frac{2s - D}{R - s}\end{aligned}\quad (2.42)$$

Going back to the front view of figure 2.9 one can see that for a closed, spherical configuration the angle  $\alpha$  has to add up for each consecutive reflection, so that:

$$2N\alpha = 2\pi \quad \text{and} \quad \cos \alpha = \frac{r_{x1}}{r_s} \quad (2.43)$$

if the aforementioned condition was not true, the Laser beam would not be able leave the Herriott-Cell after one roundtrip ( $U=1$  or  $2N$  reflections for the example shown in figure 2.9). Using eq. 2.43 to rewrite 2.42 one obtains the mirror distance  $D$  as follows:

$$\cos \alpha = \frac{R - D + s}{R - s} \quad (2.44)$$

$$D = (R - s)(1 - \cos \alpha) + 2s \quad (2.45)$$

For a spherical spot pattern of the Herriott-Cell, the reflected Laser beams all travel an identical path between the two mirrors. The total optical path length can therefore be determined by summing over all single passes within the Cell. For one roundtrip  $U=1$  with  $2N$  reflections the total optical path length is given as:

$$L = 2N \cdot L_{singlepass} \quad (2.46)$$

The geometrical pathlength of  $L_{singlepass}$  is:

$$L_{singlepass} = \sqrt{\Delta x^2 + \Delta y^2 + \Delta z^2} \quad (2.47)$$

where the respective Cartesian components can be determined with the help of figure 2.9.

$$\begin{aligned}\Delta x &= r_s \cdot (1 - \cos \alpha) \\ \Delta y &= r_s \cdot \sin \alpha \\ \Delta z &= D - 2s = \sqrt{R^2 - r_s^2} \cdot (1 - \cos \alpha)\end{aligned}\quad (2.48)$$

so that  $L_{singlepass}$  can be rewritten as:

$$\begin{aligned}L_{singlepass} &= \sqrt{[r_s \cdot (1 - \cos \alpha)]^2 + [r_s \cdot \sin \alpha]^2 + [\sqrt{R^2 - r_s^2} \cdot (1 - \cos \alpha)]^2} \\ &= \sqrt{2r_s^2 \cdot (1 - \cos \alpha) + (R^2 - r_s^2) \cdot (1 - \cos \alpha)^2} \\ &= \sqrt{2r_s^2 \cdot (1 - \cos(\pi \frac{U}{N})) + (R^2 - r_s^2) \cdot (1 - \cos(\pi \frac{U}{N}))^2}\end{aligned}\quad (2.49)$$

the overall optical path length  $l$  then becomes:

$$l = 2N \cdot \sqrt{2r_s^2 \cdot (1 - \cos(\pi \frac{U}{N})) + (R^2 - r_s^2) \cdot (1 - \cos(\pi \frac{U}{N}))^2} \quad (2.50)$$

## 2.4 Quantum cascade lasers

Quantum cascade Lasers were theoretically predicted in the 1960s and experimental realized in 1994 by J.Faist et al [24]. Due to their working principle and gain material composition these semiconductor lasers can emit Laser light in a vast majority of the infrared- and terahertz-region of the electromagnetic spectrum. Since many molecules have absorbtion lines in these regions of the spectrum, quantum cascade Lasers have become the state-of-the-art light source for many spectroscopic applications.

The working principle of a quantum cascade Laser is based on the quantum confinement of electrons in the conduction band of a semiconductor super lattice. The required quantum well can be created by placing a thin layer of a material with a lower band-gap between two sheets of a semiconductor material with a high band-gap (e.g by using GaAs and GaAlAs). This quantum well confines the movement of the electrons along the surface normal of the sheets (z-direction). The layer thickness of the materials is generally in the order of a few nanometres (or less) and one can assume a one dimensional potential well to solve the corresponding Schrödinger equation and determine the energy eigenvalue of the quantum well:

$$(\mathcal{H}_e(\mathbf{r}) + V_{con}(z))\Psi(\mathbf{r}) = E\Psi(\mathbf{r}) \quad (2.51)$$

with the confinement potential for an infinitely high well:

$$V_{con}(z) = \begin{cases} 0 & \text{for } -\frac{L_c}{2} < z < \frac{L_c}{2} \\ \infty & \text{for } |z| > \frac{L_c}{2} \end{cases}$$

where  $L_c$  is the width of the quantum well in the z-direction. The potential is symmetric around  $z=0$  and one can separate the solutions for the spatial wave functions and energy eigenvalues into odd and even states. The energy eigenvalues are given by:

$$\begin{aligned} E_{z,\text{even}} &= \frac{\hbar^2\pi^2}{2m_e L_c^2} (2n-1)^2 \\ E_{z,\text{odd}} &= \frac{\hbar^2\pi^2}{2m_e L_c^2} (2n)^2, \text{ for } n = 0, 1, 2, \dots \end{aligned} \quad (2.52)$$

The results show that the electrons have quantized eigenvalues within the valence and conduction band of the semiconductor and the energy of the states depends on the widths ( $L_c$ ) of the sandwiched semiconductor sheet. One can further generalize the results of 2.52 by adding the energy of the motion perpendicular to the z-direction. The total energy then becomes:

$$E = \frac{\hbar^2}{2m_e} \left( \frac{n^2\pi^2}{L_c^2} + k_\perp^2 \right), \text{ for } n = 0, 1, 2, \dots \quad (2.53)$$

It follows that the quantum confinement along the z-direction creates several equally spaced semiconductor sub-bands which are separated by  $\frac{\hbar^2\pi^2}{2m_e L_c^2}$ . (More realistic cases, for finite quantum wells, are showcased in [30]). Radiative and non radiative transitions between these sub-bands of the semiconductor are called intersubband transitions. The intersubband transition energy can be altered by adjusting the width ( $L_c$ ) of the sandwiched semiconductor materials. Fig. 2.10 illustrates the differences between intersubband transitions, which are used to drive QCLs and interband transitions which are the underlying principle of arbitrary laser diodes.

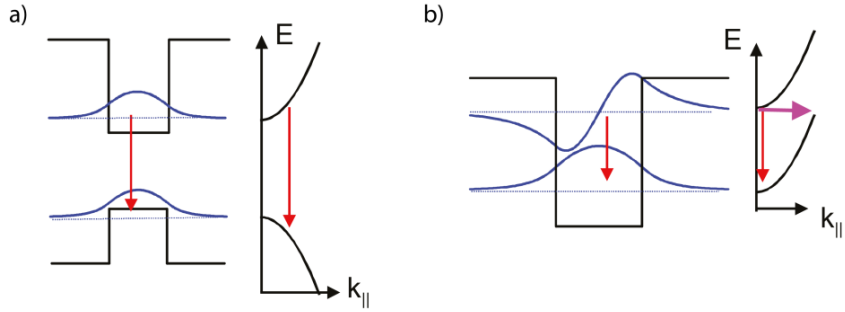


Figure 2.10: Conceptional difference between interband (a) and intersubband transitions (b). Interband transitions occur between the inversely shaped conduction and valence band. Intersubband transitions on the other hand appear between the (almost) parallel subbands of the conduction band of the semiconductor. The curvature of the bands also influences the gain of the respective lasers. Parallel bands result in a narrow, almost delta shaped, gain function while the gain of traditional interband lasers is step shaped due to the inverse curvature of the conduction and valence band. Image taken from: [23]

By clever engineering one can use the sub bands to create an effective four level laser system within the conduction band of a semiconductor super lattice. Generally, three quantum wells are combined with an injection and a relaxation area which together form one of the many unit cells of a QCL. While the quantum wells provide the three required energy levels of the Laser system, the injection area supplies the system with the necessary electrons and the relaxation depopulates the lowest energy level after the laser transition is complete.

To create a population inversion between laser levels, electron tunneling from the injection area into a quantum well and from a well into the relaxation area is used. The tunneling speeds can be engineered to be much faster than depopulating effects, like elastic or inelastic scattering, occur. This results in a constant population of the highest energy level of the unit cell, while simultaneously the electrons from the lowest energy level are depopulated quickly.

Fig. 2.11 shows an exemplaric QCL heterostucture where a population inversion between the energy levels three and two is achieved by minimizing the spatial overlap of the two states. This can be achieved by adjusting the width of the quantum wells as well as the semiconductor barriers that separate them. The transition time  $\tau_{32}$  therefore becomes around one order of magnitude slower than the depopulation rate  $\tau_2$  and the condition for a population inversion  $\tau_{32} > \tau_2$  is fulfilled. By applying a bias voltage along the z-axis of the semiconductor super lattice, the potential gets the characteristic stair-case-shape and allows the electrons to cascade through multiple unit cells.

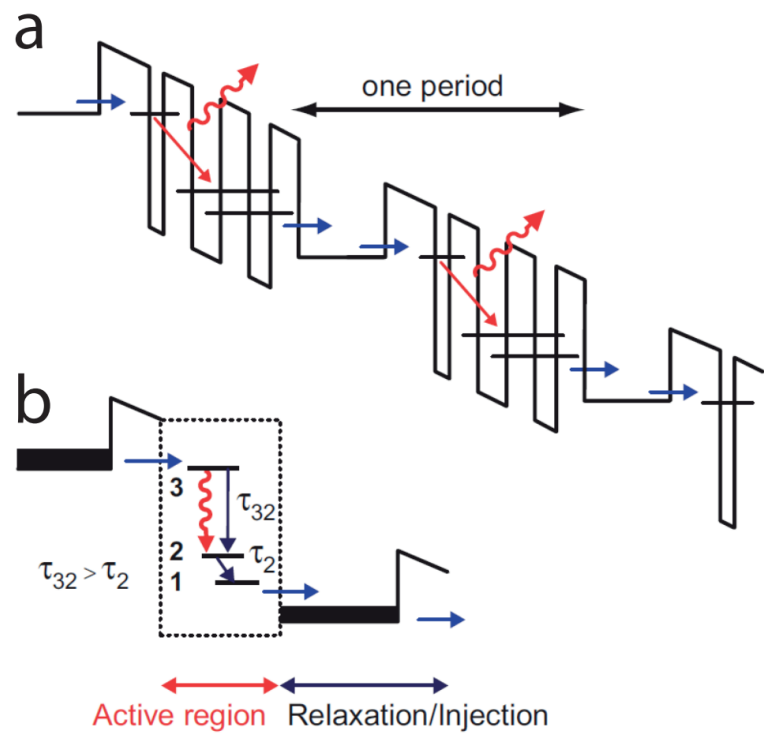


Figure 2.11: a) Periodic structure of a Quantum cascade Laser. b) Simplified unit cell of a QCL, containing all relevant energy levels and transition times. Source: [23]

## 3. Theory part II: Refractometry

### 3.1 Ideal and real gases

With the redefinition of the SI-system in 2019, gas density measurements became an interesting contestor to classical pressure assessments via measurements of the mechanical force that is acting on a surface area. Important natural constants like the Boltzmann constant  $k_b$ , the Avogadro constant  $N_a$  and the gas constant  $R$  were assigned uncertainties of zero after the redefinition. Which makes the ideal gas law:

$$\begin{aligned} p &= \rho_N k_B T, \text{ with } \rho_N = \frac{v N_a}{V} \\ p &= \rho_v R T, \text{ with } R = k_b N_a \end{aligned} \quad (3.1)$$

an appealing foundation for the construction of density based pressure-standards for the vacuum region, which are also traceable as long as the density  $\rho$  can be assessed in a traceable manner.

The ideal gas law eq.:3.1 is a simplistic approach, that does not account for electromagnetic particle-particle interactions (e.g van der Waals forces) or quadratic long-range interactions [34], which both depend on the particle density. By expanding the ideal gas law in a Taylor series for  $\rho_v$  one can account for additional density dependent effects and obtains the real gas law:

$$p = \rho_v R T (1 + B(T) \rho_v + C(T) \rho_v^2 + \dots) \quad (3.2)$$

with the second and third density virial coefficients  $B(T)$  and  $C(T)$ . The higher order virial coefficients account for multi molecule collisions, which are unlikely to occur in the vacuum regime and are therefore often times neglected for said pressure region. Figure3.1 illustrates the relation between the gas density and the partial pressure of Nitrogen for a fixed temperature of 300 K. The difference between the real and ideal Nitrogen gas is shown by the residuals from the upper plot. At atmospheric pressure the difference between the two is around 200 ppm. For pressures above  $10^6$  Pa (10 Bar), the influence of the quadratic third virial coefficient is clearly visible. The respective values for the second and third density virials were taken from: [53].

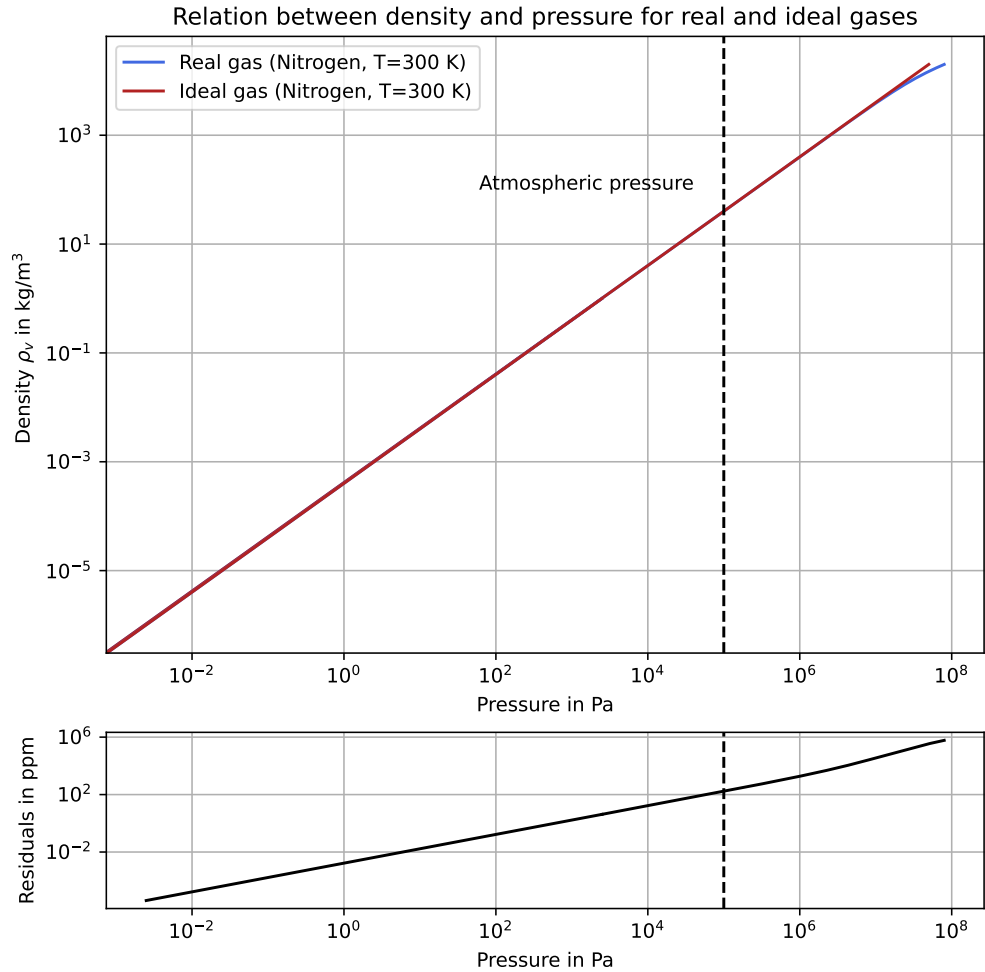


Figure 3.1: Top: Comparison between ideal and real Nitrogen gas at 300 K.  
Bottom: Residuals between the ideal and real Nitrogen gas.

## 3.2 Lorentz Lorenz equation

If light travels through a gaseous medium it can be absorbed or dispersed. In the case of absorption the light is in resonance with an electromagnetic transition of an atom or molecule and the respective photon energy is transferred to the molecule. In the case of dispersion the molecules are polarized and start oscillating at a frequency similar to that of the photon [34]. This results in net reduction of the traveling speed of the photon which can be described by the frequency dependent refractive index  $n(\nu)$  of the gas:

$$c = \frac{c_0}{n(\nu)} \quad (3.3)$$

where  $c_0$  is the speed of light in vacuum. The electric polarizability of a gas describes how susceptible a molecule or atom is to have a dipole moment induced by an external electrical-

or photon-field. For a gaseous medium, every molecule has its own internal electrical field and is furthermore exposed to the electric fields of the surrounding molecules and any additional external field, which can modify the internal state of the molecules. The properties of the matter can then be determined by averaging over all the electrical fields within it. The Lorentz-Lorenz equation relates the polarizability with the refractive index of gas and a detailed field-theory based derivation is given in [6]. The Lorentz-Lorenz equation is given as:

$$\frac{\alpha}{3\epsilon_0}\rho_N = \frac{N_A\alpha}{3\epsilon_0}\rho_v = A_R\rho_v = \frac{n^2 - 1}{n^2 + 2} \quad (3.4)$$

With the dynamic polarizability  $\alpha$ , the dynamic molar polarizability  $A_R$  and the absolute dielectric permittivity in vacuum  $\epsilon_0$ . The Lorentz-Lorenz equation does not include magnetic effects on the gas molecules nor the inter molecular effects that the gas molecules have on each other. The inter molecular effects again depend on the gas density and can be including by expanding equation 3.4 in a Taylor series for  $\rho_v$ :

$$\frac{n^2 - 1}{n^2 + 2} = A_R\rho_v(1 + b_R(T)\rho_v + c_R(T)\rho_v^2 + \dots) \quad (3.5)$$

where  $b_R$  and  $c_R$  are the second and third, temperature dependent, refractivity virial coefficients.

For gases and wavelengths in the visible spectrum, the refractive index  $n$  is generally close to 1 ( $n = 1.000282$  for nitrogen at  $15^\circ\text{C}$  and  $\nu = 627 \text{ nm}$ ,[43]). Knowing this, one can use the two simplifications:

$$n^2 - 1 \approx 2(n - 1) \text{ and } n^2 + 2 \approx 3 \quad (3.6)$$

to approximate the Lorentz-Lorenz equation (3.4) to:

$$n - 1 \approx \frac{\alpha}{2\epsilon_0}\rho_N \quad (3.7)$$

which directly relates the gas density  $\rho_N$  to the refractivity  $n-1$  of the gas.

### 3.3 Refractometry

Since both, the Lorentz-Lorenz equation and the real gas law, depend on the gas density one can combine the two equations to derive a protocol to measure the pressure  $P$  as a function of the frequency dependent refractivity:  $n(\nu)-1$ . Devices that utilize this relationship between the two properties are called refractometers.

One approach to measure the refractive index of a gas is to use Fabry-Pérot cavities. The resonator can be filled with a gas at a fixed pressure  $P$  and the resonance frequencies of the Fabry-Pérot can be compared for the evacuated and gas-filled state of the system. For a simplistic, non-deformable cavity following the methodology presented in [34], one would obtain the latter experimental property:

$$\mu_{\kappa=0} = \frac{\left(\frac{\nu_0}{\nu_p}\right)^2 - 1}{\left(\frac{\nu_0}{\nu_p}\right)^2 + 2} \quad (3.8)$$

where  $\kappa = 0$  is the assumed zero compressibility of the cavity material,  $\nu_0$  is the resonance frequency of the FP-cavity in an evacuated state and  $\nu_p$  is the resonance frequency of the

FP-cavity in the gas-filled state.

Combining the real gas law (equation 3.2) with the Lorentz-Lorenz equation (3.5) then yields an experimental approach to realize a refractometry based pressure standard:

$$P = \frac{RT}{A_R} \left( \mu_{\kappa=0} + \mu_{\kappa=0}^2 \frac{(B - b_R)}{A_R} + \mu_{\kappa=0}^3 \frac{C - 2Bb_R + 2b_R^2 - c_R}{A_R^2} + \dots \right) \quad (3.9)$$

However, the pressure induced deformation of the resonator length can not be ignored if the lowest measurement uncertainties are desired. For a linear, homogeneous deformation of the resonator, with  $\kappa > 0$ , one can describe the pressure induced length change of the resonator as:

$$l_P = l_0 + l_0 \kappa P \leftrightarrow \frac{l_P}{l_0} = 1 + \kappa P \quad (3.10)$$

where  $l_P$  and  $l_0$  are the resonator lengths with and without an applied gas pressure  $P$  respectively and  $\kappa$  is the effective length compressibility. Equation 3.8 can then be reworked to also account for the deformation of the system:

$$\mu_\kappa = \frac{\left(\frac{\nu_0}{\nu_p}\right)^2 - 1}{\left(\frac{\nu_0}{\nu_p}\right)^2 + 2} = \frac{n^2 \cdot (1 + \kappa P)^2 - 1}{n^2 \cdot (1 + \kappa P)^2 + 2} \approx \frac{n^2 \cdot (1 + 2\kappa P) - 1}{n^2 \cdot (1 + 2\kappa P) + 2} \quad (3.11)$$

In the last step quadratic terms in  $\kappa$  were discarded since the compressibility for glasses (e.g Quartz glass:  $\kappa \approx 2.7 \cdot 10^{-10}$  m/Pa) is very small. The working equation for the refractometry based pressure standard then becomes:

$$P = \frac{RT}{A_R + \frac{2\kappa RT}{3}} \left( \mu_\kappa + \mu_\kappa^2 \frac{(B - b_R - \frac{2\kappa RT}{3})}{A_R + \frac{2\kappa RT}{3}} + \dots \right) \quad (3.12)$$

after combining equations 3.11, 3.2) and 3.5 up to the second order of the Taylor expansions.

### 3.3.1 Dual Farby-Pérot cavity based refractometry

For experimental dual-FPC based approaches to refractometry it is convenient to measure the refractivity  $n-1$  of the investigated gas, based on a shift to a beat measurement  $\frac{\Delta f}{\nu_0}$  instead of two individual Laser frequency measurements. This has practical reasons, since beat frequencies, up to several GHz, can be measured and evaluated with relatively cheap equipment like high-speed beat detectors, frequency counters and spectrum analyzers. State of the art RF-electronics can also be read at a high speed and basically allow for real-time investigations of the chosen system.

The beat frequency  $\Delta f$  between the two lasers, which are phase locked to the resonance frequencies of the respective measurement and evacuated reference FP-cavity, shifts if additional gas is introduced or removed from one of the FP-cavities. When mode jumps take place, the mode number  $\Delta q$  has to be adjusted accordingly and one can assess the refractivity of the investigated gas as a function of the change in beat frequency between the two laser fields:

$$n - 1 = \frac{\Delta f + \Delta q_m}{1 - \delta f + \epsilon_m} \quad (3.13)$$

## 4. Theory part III: Optical resonators

### 4.1 Fabry-Pérot resonators

A Fabry-Pérot interferometer (FPI) is a basic optical resonator that consist of two plan-parallel mirrors which are often times attached to a deformation resistant spacer material with a constant length L. FPI's are commonly used for high resolution spectroscopy or as Laser resonators. The incident light is reflected between the two highly reflective mirrors, which results in multi-beam interference inside the resonator. The interference is constructive when the resonance condition is met and the longitudinal resonator modes (frequencies at which constructive interference is possible) are given as:

$$\nu_q = \frac{qc}{2nL} \quad (4.1)$$

where q is the (integer) mode number, c is the speed of light, L the length of the cavity and n the refractive index of the gas inside the FPI. Only light with the proper frequencies  $\nu_q$  is transmitted through the resonator which makes FPI's great optical filters. The quality of this filter is described by the free spectral range (FSR) and the finesse of the resonator. The FSR is the frequency difference between two consecutive longitudinal resonator modes and is given by:

$$\Delta\nu = \nu_{q_{i+1}} - \nu_{q_i} = \frac{c}{2nL} \quad (4.2)$$

The finesse describes the spectral broadening of the resonator modes in relation to the free spectral range. The finesse correlates directly with the reflectivity of the mirrors and is given by:

$$F = \frac{\Delta\nu}{\nu_{FWHM}} = \frac{\pi\sqrt{r}}{1-r} \quad (4.3)$$

#### 4.1.1 Longitudinal resonator modes

If the multiple reflection of a plane wave between two plane-parallel partially reflecting layers is considered, the finesse and the free spectral range can be derived directly from wave theory. The incident wave:

$$E = E_0 e^{i(\omega t - kx)} \quad (4.4)$$

hits the reflecting surfaces at an angle  $\alpha = 0$  and is split into two partial beams at each mirror. One partial beam is reflected and one is transmitted through the mirror (see figure 4.1). The initial partial Beam  $E_1$  transmitted through the FPI experienced no reflections inside the resonator but was transmitted through both mirrors. Its amplitude is therefore given by

$$E_1 = E_0 t^2 e^{ikL}$$

where  $t$  is the transmittance of the mirror given by  $t = \frac{E_t}{E_0}$ . Due to the finite distance  $L$  between the two mirrors, each round-trip of the partial wave inside the cavity accumulates an additional phase  $e^{i\delta}$  with  $\delta = 2kL$ . The second partial beam ( $E_2$ ) that is transmitted through the FPI has experienced two transmission and two reflections. Its amplitude can again be written as:

$$E_2 = E_0 t^2 e^{i\frac{\delta}{2}} r^2 e^{i\delta}$$

with the similarly defined mirror reflectance  $r = \frac{E_r}{E_0}$ .

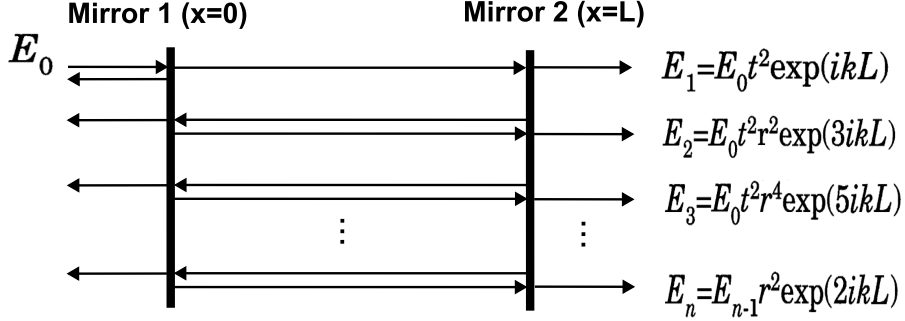


Figure 4.1: Illustrated are the reflections and transmissions of a simple FPI. Image taken and reworked from: [36]

For many spectroscopic applications the light that is transmitted through the resonator is of greatest interest, since it represents the frequencies of the light that can freely path through the optical filter (longitudinal resonator modes). Summing over all partial waves, including the correct phase shift, yields the total transmitted amplitude [16][36].

$$E_t = \sum_{n=1}^{\infty} E_n = E_0 t^2 e^{i\frac{\delta}{2}} \sum_{n=1}^{\infty} r^{2(n-1)} e^{i\delta(n-1)} = E_0 t^2 e^{i\frac{\delta}{2}} \sum_{n=0}^{\infty} (r^2 e^{i\delta})^n$$

This geometrical sum can be written in closed form as:

$$E_t = \frac{E_0 t^2 e^{i\frac{\delta}{2}}}{1 - r^2 e^{i\delta}} \quad (4.5)$$

The corresponding transmitted total intensity is given by the Airy function as following:

$$\begin{aligned} I_t &= E_t E_t^* = E_0 E_0^* t^4 \frac{1}{(1 - r^2 e^{i\delta})(1 - r^2 e^{-i\delta})} \\ &= I_0 t^4 \frac{1}{1 + r^4 - 2r^2 \cos(\delta)} \\ &= \frac{I_0}{1 + \left(\frac{2r}{1-r^2}\right)^2 \sin^2(\frac{\delta}{2})} = \frac{I_0}{1 + F^* \cdot \sin^2(\frac{\delta}{2})} \end{aligned} \quad (4.6)$$

in the last step the trigonometric identity  $\cos(2x) = 1 - \sin^2(x)$  was used together with the conservation of energy which states:  $r^2 + t^2 = 1$ . The introduced factor  $F^* = \left(\frac{2r}{1-r^2}\right)^2$  is the

Finesse coefficient. Figure 4.2 shows the Airy function for different resonator configurations. The points of greatest interest are the maxima at which all light is transmitted through the cavity and the distance between the individual peaks which defines the FSR or the spectral resolution if the FPI is used as a spectrometer.

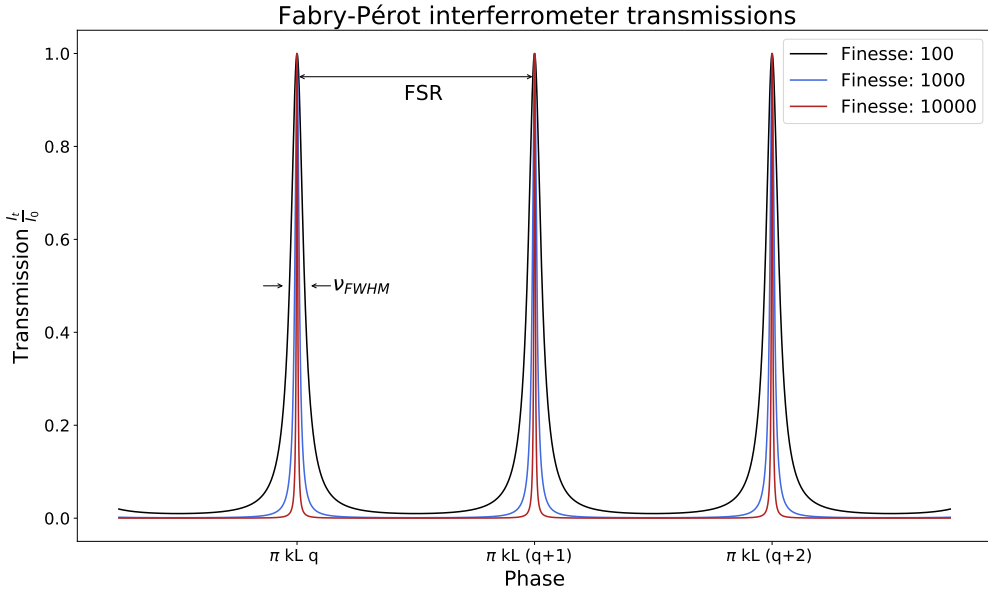


Figure 4.2: Shown are three different FPI resonator configurations with different values for their finesse and their respective longitudinal resonator modes.

Two consecutive waves with the wave vectors  $k_q$  and  $k_{q+1}$  have a phase difference of  $\pi$ . Using  $\nu = \frac{c}{2\pi}k$  one can again calculate the FSR:

$$\begin{aligned}\pi &= (k_{q+1} - k_q)L = \Delta k L \\ &= \frac{2\pi\Delta\nu}{c}L \Rightarrow \Delta\nu = \frac{c}{2L}\end{aligned}\quad (4.7)$$

Using the definition of the finesse which is given as the ratio of the FSR to the frequency widths  $\nu_{FWHM}$  of the resonator modes at half their maximal Intensity, so  $\frac{I_t}{I_0} = \frac{1}{2}$ , one can derive an expression for the finesse directly from eq. 4.6:

$$\frac{1}{2} = \frac{1}{1 + F^* \cdot \sin^2(k'L)} \text{ with } F^* \cdot \sin^2(k'L) \stackrel{!}{=} 1 \quad (4.8)$$

This can only be achieved for reasonably small wave vectors  $k'$  and therefore large mirror reflectivities. For small  $k'$  one can rewrite [36]:

$$F^* \cdot \sin^2(k'L) \approx F^*(k'L)^2 = F^* \left( \frac{\pi\nu_{FWHM}}{c} L \right)^2$$

With the definition of the finesse coefficient  $F^*$  introduced in 4.6 one can derive an expression for the required frequency widths  $\nu_{FWHM}$ .

$$\nu_{FWHM} = \frac{c}{\sqrt{F^*} L \pi} = \frac{c(1 - r^2)}{2rL\pi} \quad (4.9)$$

The finesse  $F$  can be calculated with the results from eq.(4.7) and eq.(4.9):

$$F = \frac{\Delta\nu}{\nu_{FWHM}} = \frac{r\pi}{1-r^2} \quad (4.10)$$

### 4.1.2 Gaussian Beam propagation

Due to their optical properties, Fabry-Pérot resonators are commonly used as a frequency reference for Laser systems. The Laser light (generally) has a Gaussian beam profile with varying coherence length, depending on the laser type used. In practice FPI's are therefore often realized with at least one spherical mirror which is used to refocus the light and greatly simplifies the optical alignment and stability of the cavity. To form a stable resonator the condition:

$$0 \leq g_1g_2 \leq 1 \quad (4.11)$$

For the case  $g_1g_2 = 1$  (plan-plan) the resonator is theoretically still stable but creates infinitely large beam spots at the mirrors which makes the configuration practically unstable. The beams, reflected back and forth within these resonator types, retain their Gaussian profile. However, inherent properties such as the beam radius and the position of the beam waist are influenced by the mirrors curvature and have to be taken into account during optical alignment to ensure optimal coupling into the resonator. The beam radius  $\omega(z)$  of the Gaussian beam, along the optical axis, is given by:

$$\omega(z) = \omega_0 \sqrt{1 + \left(\frac{z}{z_R}\right)^2} \quad \text{with} \quad z_R = \frac{\pi\omega_0^2}{\lambda} \quad (4.12)$$

where  $\omega_0$  is the beam waist and  $z_R$  is the Rayleigh length. To couple light into a e.g confocal resonator efficiently, the beam profile outside and inside of the resonator have to match. In the case of the aforementioned confocal configuration this can be achieved by creating a focus of the Laser beam at  $L/2$ , the center of the cavity, which can be realized experimentally with a set of lenses.

### 4.1.3 Transversal Resonator modes

In addition to the Gaussian mode, higher-order transverse electromagnetic modes ( $\text{TEM}_{mn}$ ) can also be formed inside the resonator. Their electrical field can described by the Hermite-Gauss polynomials ( $H_n$ , where  $n$  is the respective polynomial order) and is given by:

$$E_{mn}(x, y, z) = E_0 \frac{\omega_0}{\omega(z)} H_m\left(\frac{\sqrt{2}x}{\omega(z)}\right) H_n\left(\frac{\sqrt{2}y}{\omega(z)}\right) \\ \cdot \exp[-(x^2 + y^2)\left(\frac{1}{\omega^2(z)} - \frac{ik}{2}R(z)\right) + ikz - i(m+n+1)\tan^{-1}\left(\frac{z}{z_0}\right)] \quad (4.13)$$

with the radius of curvature of the wavefront  $R(z) = z + \frac{z_0^2}{z}$  and the transversal mode numbers  $m$  an  $n$ .

The frequencies of the transversal modes are given as:

$$\nu_{qmn} = \frac{c}{2L} \left( q + \frac{1}{\pi} (m+n+1) \cos^{-1}(\sqrt{g_1g_2}) \right) \quad (4.14)$$

For  $m = n = 0$  one obtains the  $\text{TEM}_{00}$  mode which is equivalent to the Gaussian mode. For experimental applications it is often times desirable to only excite the  $\text{TEM}_{00}$  mode inside the resonator, since the overall transmitted intensity is highest and the Laser beam retains its optical properties. Figure 4.3 shows the first 16 TEM modes, starting with the  $\text{TEM}_{00}$  up to the  $\text{TEM}_{33}$ -mode.

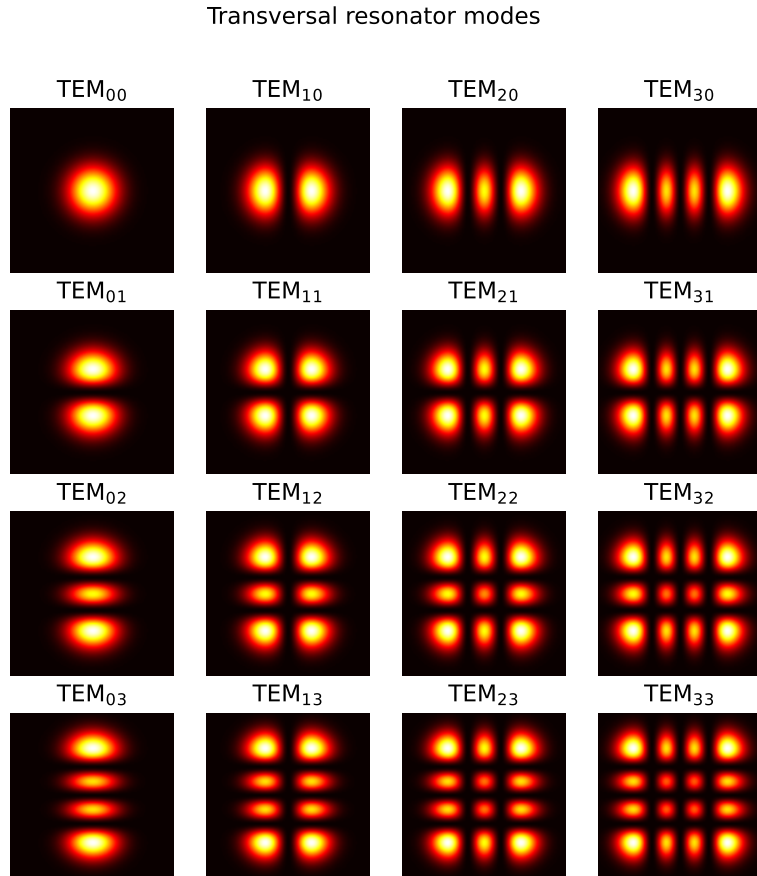


Figure 4.3: Shown are the first 16 TEM-modes. Starting from the  $\text{TEM}_{00}$ - and going up to the  $\text{TEM}_{22}$ -mode.

#### 4.1.4 Mode-matching

In the context of refractometry, it is often times important to only excite the  $\text{TEM}_{00}$  with the chosen Laser source. This is required to correctly identify the Laser frequency and avoid complications with Laser-locking techniques. Higher order modes are generally only excited if the incident Laser beam spatially overlaps with them, which can be avoided by proper Laser alignment. If the beam propagation and spatial profile of the Laser light match with spatial profile of the  $\text{TEM}_{00}$  inside the resonator, only the  $\text{TEM}_{00}$  mode will be excited inside the cavity. With knowledge of the radius of curvature of the cavity mirrors, the mirror distance and cavity type (spherical-spherical or plan-spherical mirrors) one can ideally mode-match the Laser with the resonator. Figure 4.4 illustrates the basic operating principle of spatial mode-matching.

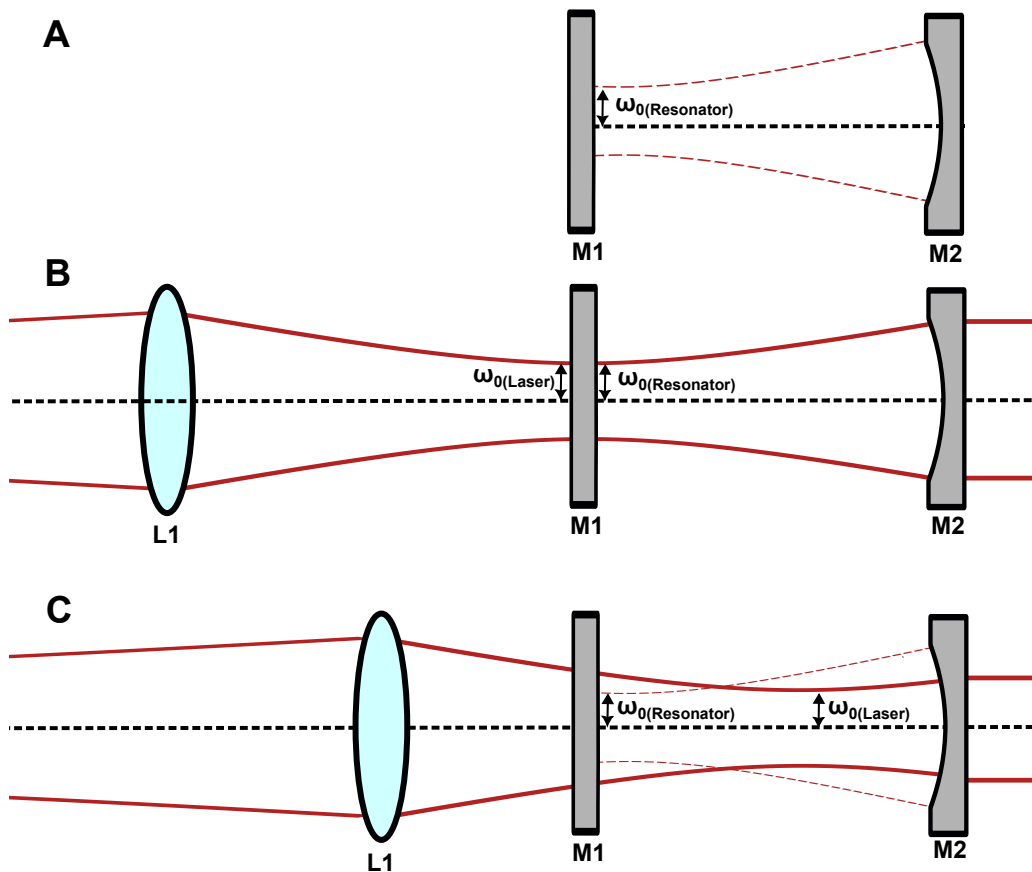


Figure 4.4:

- A) Plan-spherical resonator shown together with the ideal Gaussian beam propagation.
- B) Mode matched Laser and resonator.
- C) Sub-par matching of the spatial profiles of the Laser and the resonator.

**Case A** shows the stable configuration for a  $\text{TEM}_{00}$  mode in a plan-spherical resonator and the respective beam waist  $\omega_0$ (resonator), which is located at the planar mirror.

For **case B** a Laser together with a focusing lens L1 is added. The Laser is mode matched with the resonator for a properly chosen focusing lens. The beam waist of the Laser ( $\omega_0(\text{Laser})$ ) and the beam waist of the resonator are located at the same position along the propagation axis of the light.

**Case C** illustrated the sub-par matching of the Laser and the resonator. This configuration can results in less Laser light intensity being transmitted through the resonator and additional, unwanted resonator modes being excited inside the cavity.

For invisible lasers, it is useful to look at the intensity transmitted through the resonator while the laser is de-tuned in frequency. The laser can then be adjusted so that only the longitudinal modes are visible in the spectrum. This can be achieved with a simple experimental setup, which only requires a photodetector, a Laser and the FPI. Figure 4.5 shows a simulated detector signal, which can be observed when the Laser is de-tuned in its frequency by applying a voltage ramp to the Laser-driver. The first spectrum is typical for a miss aligned Laser with respect to the cavity. The spectrum on the right shows the signal for a almost perfectly mode matched Laser. The  $\text{TEM}_{00}$  modes have the highest possible intensity and no higher order modes are visible.

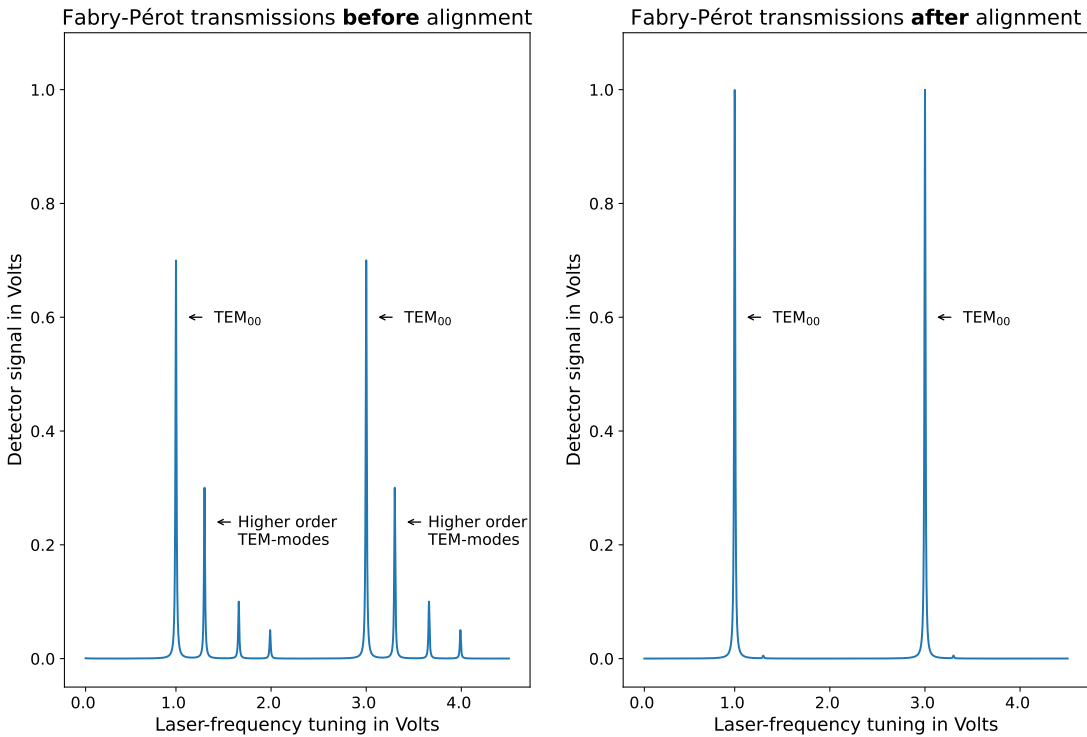


Figure 4.5: Shown are the transmission spectra of a theoretical FPI before and after aligning the Laser to the cavity.

## 4.2 Laser-frequency stabilization

A general approach to stabilize the frequency of a tunable Laser is to use an external cavity as a frequency filter. Only a few equally spaced modes, given by the free spectral range of the resonator, form standing waves inside of the cavity. Which means that an intensity build up inside the cavity can only occur if the line profile of the laser overlaps with one of the resonator modes. For the resonant case one can measure the intensity that is transmitted through the cavity and utilize it to create a feedback-loop for laser-frequency-stabilization. The total transmitted intensity is depending on the frequency difference between the laser and the selected single cavity mode and can be measured with a photosensitive detector. For a large relative difference between the two frequencies the transmitted intensity is small and vice versa. Based on this relation it becomes possible to create a feedback loop between laser and detector. Whenever the detector signal drops one can tune the frequency of the laser until the maximum transmitted intensity is restored. This general approach has several disadvantages. A few of them are: It is a priori not possible to know if the laser shifts to higher or lower frequencies when the detector intensity drops and it is also not possible to differentiate between laser-intensity-fluctuations and actual frequency shifts [5].

### 4.2.1 Lock-In technique

### 4.2.2 Pound-Drever-Hall procedure

The Pound-Drever-Hall technique is a commonly used technique to stabilize the frequency of a laser fast and effectively.

## 5. Absorption spectroscopy

During this thesis, two independent pressure standards were designed, constructed, automated and characterized. One experimental setup utilizes Tuneable-Diode-Laser-Absorption-Spectroscopy (TDLAS) to measure important gas parameters like the line strength as well as partial pressures of relevant climate gases like carbon monoxide. The second pressure standard is a dual-cavity refractometer which can be used for static and dynamic partial pressure assessments of different gasses including, but not limited to: Helium, Nitrogen and Argon. The systems cover a conjoint pressure range between  $10^{-3}$  and  $10^5$  Pa, where the TDLAS system covers the lower pressure range up to  $10^2$  Pa and the refractometer the higher range from 1 Pa up to atmospheric pressure. This leaves a small pressure range where both system can be compared to each other.

### Experimental setup: TDLAS

The Tuneable Diode Laser absorption spectroscopy setup, built during this thesis, utilizes Quantum cascade lasers as a tuneable light source and Herriott-Cells to increase the optical path length that the laser light travels through the absorbing medium. The emission frequency of the QCL can be tuned over several absorption lines of the fundamental band of Carbon monoxide between 2155 and  $2170\text{ cm}^{-1}$ <sup>1</sup>. The frequency dependent absorption signals are measured with fast and highly sensitive photodetectors and can then be integrated to get the measurement parameter  $A_{line}$  used in:

$$A_{line} = S \cdot \frac{p}{k_B T} \cdot L \quad (5.1)$$

If the pressure P, the temperature T and the optical pathlength L are known during the measurement one can determine the linestrength S of the respective ro-vibrational transition. On the other hand, knowledge of the linestrength parameter can be utilized to perform high precision pressure assessments, potentially covering a wider pressure range than the pressure sensor used for the linestrength measurements.

Figure 5.1 illustrates the general experimental setup used for all TDLAS measurements including all optical and electrical components used. The following section will be used as a general description of the experimental setup and will be followed by a more detailed analysis of the individual experimental challenges.

---

<sup>1</sup>Inverse centimeter is a frequency unit commonly used by the spectroscopic community and will be used during this thesis to simplify data comparisons

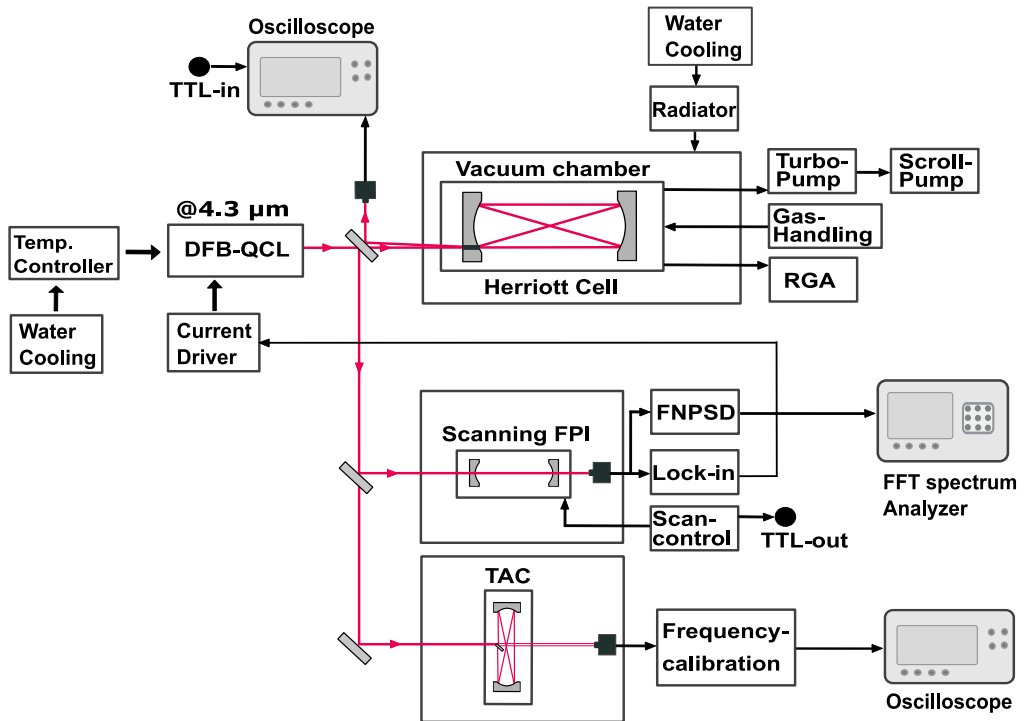


Figure 5.1: Experimental setup with all optical and electrical components used for TDLAS

A **DFB-QCL** (Alpes Model:) is used as a light source in the mid infrared region ( $4.3\mu\text{m}$  /  $2160\text{cm}^{-1}$ ). Electrical noise has a significant influence on the laser linewidths, which in turn is relevant for the determination of the integrated absorbance. It is therefore crucial to minimize all electrical noise when applying voltage or current ramps to the laser in order to scan over it's frequency. Therefore a **low noise current driver** (ppq-Sense: Model QubeCl 500) is used to drive the QCL and optimize its performance. The QCL has an internal Peltier element which can be used to modulate the laser temperature between  $-20^\circ$  and  $25^\circ$  Celsius. The thermometric cooler is mounted onto a water-cooled heat sink which dissipates the generated heat away from the QCL.

To further reduce the Laser linewidths, the QCL emission is phase-locked to a **Fabry-Pérot cavity** mode (Thorlabs: Model: SA200-30C). The laser-locking is achieved digitally, with a Field-Programmable-Gate-Array chip (FPGA) (Toptica: Model: Digilock), that allows the implementation of the **Lock-In** and Pound-Drever-Hall techniques. The FPGA voltage output is connected to the current modulation input of Laser driver and creates a feedback loop between the signal that is transmitted through the FPI cavity and the emission frequency of the QCL. (The Laser frequency can be adjusted by increasing or decreasing the current that is applied to the Laser). The pid controller of the FPGA modulates the output frequency of the QCL until it perfectly overlaps with the transmission frequency of the  $\text{TEM}_{00}$ -mode of the FPI. By constantly forcing the QCL emission frequency onto the narrow FPI-maximum transmission frequency, one can very effectively reduce the Laser linewidths even further.

---

The disadvantage of locking a laser to stable frequency reference is, that it can not be tuned directly anymore. This is due to the pid controller of the FPGA that constantly counteracts any external frequency modulation, including those that are applied directly to the Laser driver modulation input by current or voltage ramps. For TDLAS however the tuning of the laser frequency over the absorption line is required and one has to achieve it by indirectly tuning the Laser frequency. This is done by modulating the lengths of the FPI cavity to which the QCL is locked to. The **scanning-FPI** includes a piezoelectric transducer which can be compressed and expanded to reduce or increase the FPI lengths. By changing the lengths of the FPI, the Free Spectral Range (FSR) of the FPI changes ( $\Delta\lambda_{FSR} = \frac{\lambda^2}{n \cdot L}$ ) and therefore the frequency position of the  $TEM_{00}$  mode to which the laser is locked changes as well. This procedure allows for a smooth indirect tuning of phase-locked QCL. The voltage ramp, that is applied to the FPI piezoelectric transducer can then be used as a trigger input for the absorption measurement.

The Laser light exiting the QCL is split, using beam splitters. A small portion of the light is used to stabilize the Laser-frequency using the Lock-In technique and measure the relative frequency change. Most of the light however is coupled into the **Herriott-Cell**, where the absorbing gas is present and the measurements are performed. Depending on the configuration of the Herriott Cell and the respective distance of the Herriott-Cell mirrors to each other, optical path length between 2 and 100m can be achieved. The Herriott Cell is integrated into a 40 liter stainless steel **vacuum chamber**, that is evacuated with a turbomolecular pump and a membrane pump. The Light that exits the Herriott Cell is focused onto a detector (Thorlabs: Model PDA07P2) and filtered using a **Lock-In amplifier** (Stanford Research Systems: Model: SR850).

Since the absorption signal  $A_{line}$  is integrated over the frequency that the laser scanned, it is necessary to have precise information of the relative frequency change during the QCL-scan. Therefore a second transversally coupled Herriott-Cell (**TAC**) is used as an interferometer. The optical path length of the TAC is well known. And by measuring the interference fringe distances one can very precisely determine the relative frequency change.

The **measurement gas** (CO with a purity of 3.7 or 4.7) is injected into the measurement chamber through a needle valve which allows the setting of very small partial pressures. After connecting the gas bottle to the system the connecting tubes were purged with CO more than five times to eliminate potential gas impurities. The exhaust of the membrane pump was directly connected to the ventilation port of the laboratory to avoid accumulation of CO in the optical pathway (outside of the Herriot Cell) and inside the laboratory. A **mass spectrometer/RGA** (MKS: Model: Vision-2000) is connected to the vacuum chamber to measure the overall Measurement gas composition and to detect vacuum leaks or gas impurities.

Three different **pressure sensors** are used to assess the pressure when linestrength measurements are performed. A spinning rotor gauge (SRG) (Ph-instruments: Model: VIM-2) is used for the low pressure range between  $10^{-5}$  and  $10^2$  Pa. A capacitive diaphragm gauge (CDG) (MKS: Model: AA06A, 1 Torr) covers  $10^{-1}$  to  $10^2$  Pa and the quartz based pressure standard (Paroscientific: Model: Model 745) is operational between 1 and  $10^5$  Pa.

The Vacuum chamber, as well as all optical component are placed within a **thermostatized environment**. The volume is thermally insulated with the help of styrofoam plates and the temperature within the volume is controlled and stabilized with a water cooled bath (PolyScience: Mode: AP15R) and several radiators. Temperature measurements are performed with two cali-

brated 25 ohm Standard Platinum Resistance Thermometers (**SPRTS**) (Fluke: Model:5686-B) and a measurement bridge (Isotech: Model: MircoK 70) together with four additional **PT-100** sensors (Ludwig Schneider: Model: Physics 1000). All sensors are positioned around the vacuum chamber and are in direct contact with the stainless steel, to ensure the best thermal contact and precise gas temperature measurements.

## 5.1 Laser characterization

As a preparatory measurement, the performance of the Quantum cascade Laser was investigated to ensure a stable and mode-hop free operation within the desired frequency regions. For this purpose, the laser current was increased at a constant laser temperature until an emission could be measured with a power meter (Thorlabs: Model:PM400K5). The power meter was positioned 1 cm in front of the QCL and a current of 250 mA was not exceeded for safety reasons. Figure 5.2 shows the optical power of the laser in comparison to the applied current and the compliance voltage. The maximum optical power at a constant laser temperature of -20°C and a current of 250 mA is around 100 mW. One can also observe that the QCL can be tuned mode hop-free within the tested parameters since no characteristic power drop with increasing current can be observed. Due to their high compliance voltage of 9-15V Quantum Cascade Laser usually require specific Laser drivers, since the widely available Laser-diode-drivers often only support a compliance voltage of 5V.

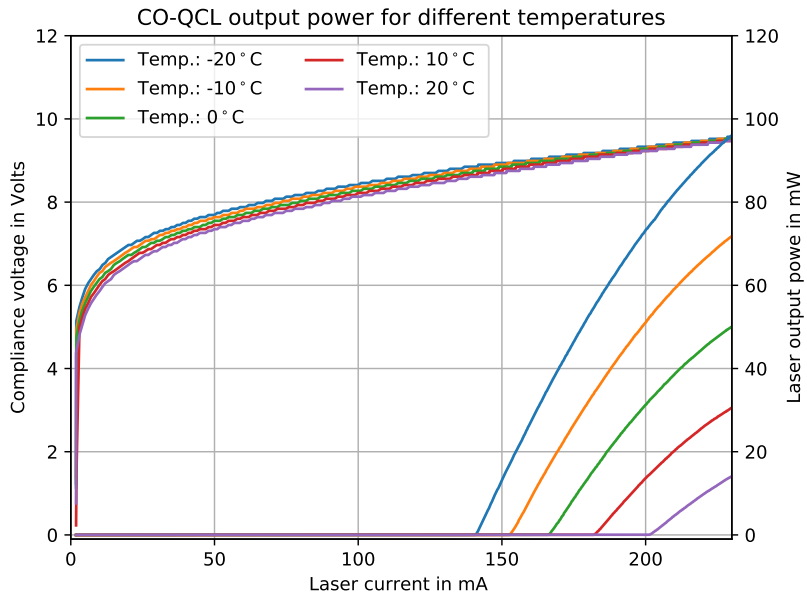


Figure 5.2: QCL output power in comparison to the applied current and compliance voltage for different Laser temperatures between -20 and +20°C.

### 5.1.1 Laser tuning range

Two additional important properties of Quantum Cascade Lasers are: their absolute emission frequency and their maximum tuning range. Both of these properties were investigated thoroughly with the experimental setup described in 5.1. The tuning range of the Laser is limited by the Laser driver, which has a wide-modulation input channel that translates a voltage ramp of 1V into a current ramp of 0.1 mA. Another modulation input has a finer translation of 0.01mA/V which is suitable for Laser locking. The maximum voltage that can be applied to the Laser driver is 2V.

To investigate what a Voltage ramp of 2V translates to in terms of Laser frequency modulation, one can use a FPI as a frequency reference and monitor the transmission signal of the cavity. Figure 5.3 shows the transmission of the FPI, when a triangle function with a 2V amplitude is applied to the modulation input of the Laser Driver. Up to seven individual  $\text{TEM}_{00}$  modes are visible, if the Laser is properly aligned and mode matched with the resonator. At a cavity lengths of 10 cm the free spectral range is equal to 1.5 GHz, which results in a total current-tuning range above 10.5 GHz.

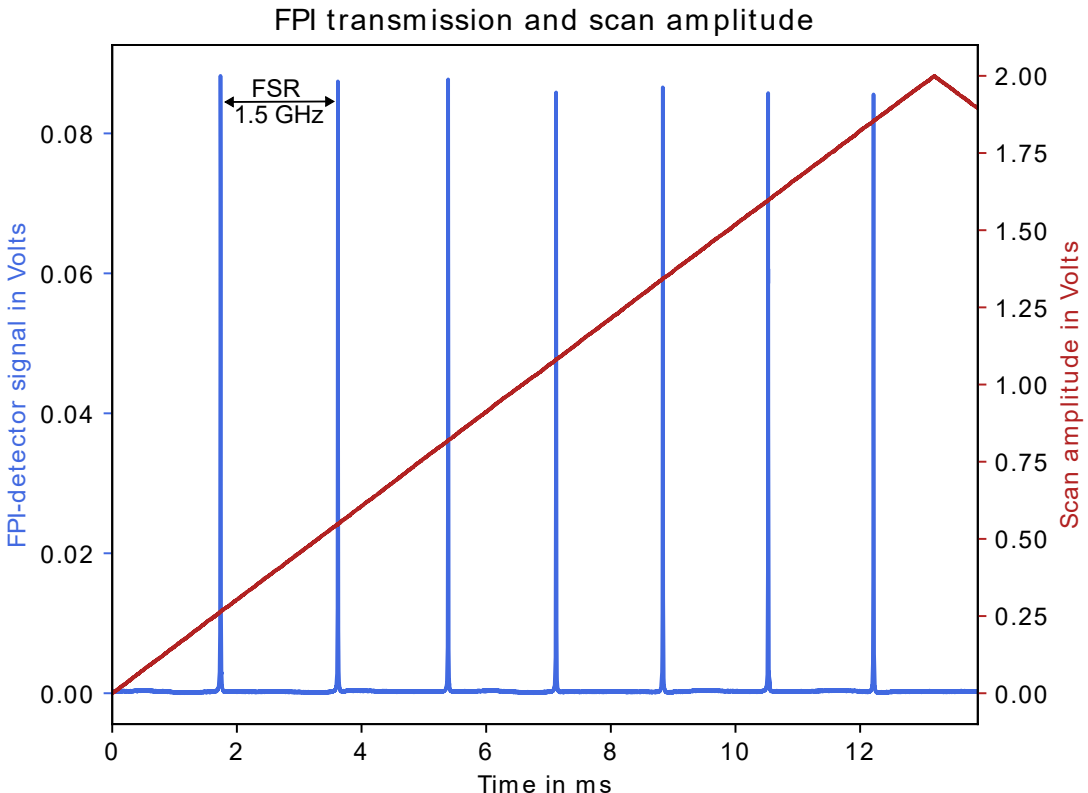


Figure 5.3: Shown is the FPI transmission, measured with a photo detector, when a periodic triangle ramp with an amplitude of 2V is applied to the modulation input of the Laser driver.

A slower method of tuning the absolute laser frequency is adjusting the Laser temperature. The semiconductor chips of QCL's are often times mounted onto a Peltier element which can be both,

heated or cooled depending on the direct current that is applied. Once the desired temperature is reached a pid controller stabilizes the current applied to the Peltier element and Laser temperature remains constant. Changes in the Laser temperature usually result in much larger changes of the absolute emission frequency of the QCL and can be used to tune the Laser to different absorption lines which can not be covered by a single Laser-current scan.

Figure 5.4 shows the transmission signal of the FPI while the temperature was decreased in  $-1^{\circ}\text{C}$  steps from  $+23^{\circ}\text{C}$  to  $-20^{\circ}\text{C}$ . The QCL was operating at a constant Laser current of 240mA, while a saw-tooth function, with an amplitude of 2V, was constantly applied to the modulation input of the Laser driver. By changing the QCL-temperature by  $1^{\circ}\text{C}$  one can tune the Laser frequency by around 4.5GHz. Which means that the last  $\text{TEM}_{00}$  mode observed in the first scan configuration with  $I=240\text{mA}$  and  $T=23^{\circ}\text{C}$  has the same frequency as the first  $\text{TEM}_{00}$  mode of the second scan with the configuration:  $I=240\text{mA}$  and  $T=22^{\circ}\text{C}$ .

The consecutive scan configurations in Figure 5.4 are indicated by different color schemes and labeled from  $n=1$  to 43, where  $n$  represents the change in temperature in degrees Celsius since the initial scan with  $T_0=23^{\circ}\text{C}$ . One can also observe a change in signal amplitude which is transmitted through the FPI. The signal amplitude on the detector directly scales with the Laser output power at different operating temperatures. For temperatures higher than  $23^{\circ}\text{C}$  lasing of the QCL is unstable and temperatures lower than  $-20^{\circ}\text{C}$  were avoided for safety reasons.

The emission frequency of the QCL (at a fixed operating current of 240mA) can be tuned by total of  $8.8 \text{ cm}^{-1}$  or 0.263 THz by changing the operating temperature.

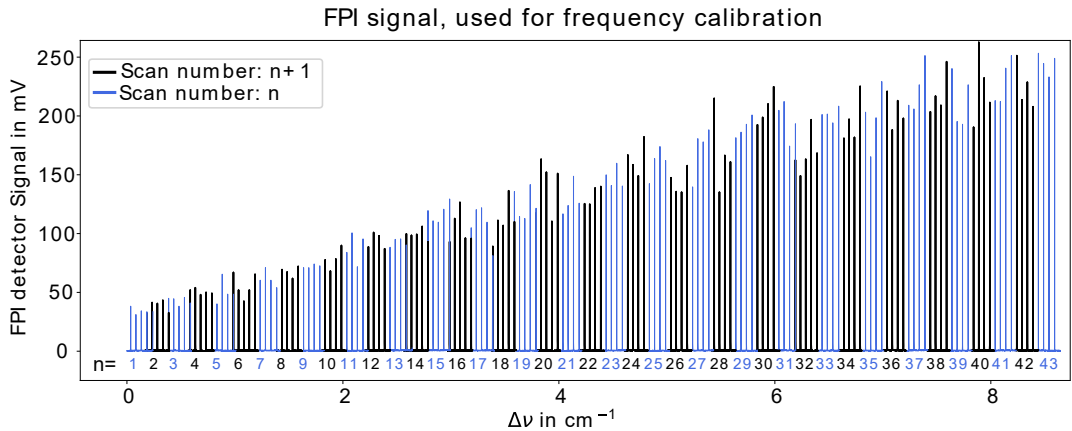


Figure 5.4: Shown is the FPI transmission signal for 43 consecutive Laser scans with a modulation amplitude of 2V. After each individual scan the Laser temperature was decreased by  $1^{\circ}\text{C}$ , with an initial and final operating temperature of  $23^{\circ}\text{C}$  and  $-20^{\circ}\text{C}$  respectively.

### 5.1.2 Absolute emission frequency

After determining the relative frequency tuning range of the QCL, one has to determine the absolute emission frequency to identify the line position of the individual absorption line.

For many diode Lasers with emission wavelength below  $2\mu\text{m}$  this can be achieved with direct comparisons to known frequencies (e.g Helium-Neon Lasers at 633nm) or interferometric

approaches like wavemeters. Since quantum cascade lasers have only been commercially available for a few years, the supply of high-quality optical components, like dielectric mirrors with high reflectivities ( $R > 99.99\%$ ) which are required for many interferometric setups, is limited or disproportionately expensive due to high development costs. One can however compare the experimental absorption measurements with existing, often theoretically determined, database entries like HITRAN and obtain the absolute frequency of all absorption lines in the Laser tuning range.

To perform such a measurement, the vacuum chamber containing the Herriott-Cell was filled with a constant Carbon monoxide pressure of 18.2 Pa. This partial pressure was chosen so that absorption lines with different linestrength can be observed simultaneously. The optical pathlengths of the Herriott-Cell was adjusted to 101m and the transmission signals were measured with a photodetector. The absorbance is obtained by:

$$A = -\ln\left(\frac{I}{I_0}\right) \quad (5.2)$$

where  $I$  is the frequency dependent transmission signal at a partial CO-pressure of 18.2 Pa and  $I_0$  the transmission signal for a fully evacuated vacuum chamber. To compare as many experimentally obtained absorption lines with the data base as possible, it is best to scan the Laser over the complete tuning range while measuring the absorbance. The upper image of Figure 5.5 illustrates a complete temperature scan of the QCL from 23°C to -20°C with the measured absorbances. As shown in the previous section, the chosen temperature scan corresponds to a relative frequency modulation of  $8.8 \text{ cm}^{-1}$ .

The lower image of Figure 5.5 shows a simulated absorbance spectrum for  $^{12}\text{C}^{16}\text{O}$  and the first three isotopologues:  $^{13}\text{C}^{16}\text{O}$ ,  $^{12}\text{C}^{18}\text{O}$ ,  $^{12}\text{C}^{17}\text{O}$  at a pressure of 18.2 Pa, a gas temperature of 296 K and an optical pathlengths of 101 m. The Hartmann-Tran lineshape profile was chosen for all absorption lines, which is an expansion of the speed dependent Voigt profile and currently has the smallest residuals when compared to the respective experimental data [41]. The additional absorption line parameters required for the simulation, such as self broadening coefficients, line positions or line strengths, can be accessed from the HITRAN database directly via an API (Application program interface) [44]. The frequency resolution was set to  $10^{-5} \text{ cm}^{-1}$  and the spectrum was simulated for absolute frequencies between 2158.2 and 2166.99  $\text{cm}^{-1}$ .

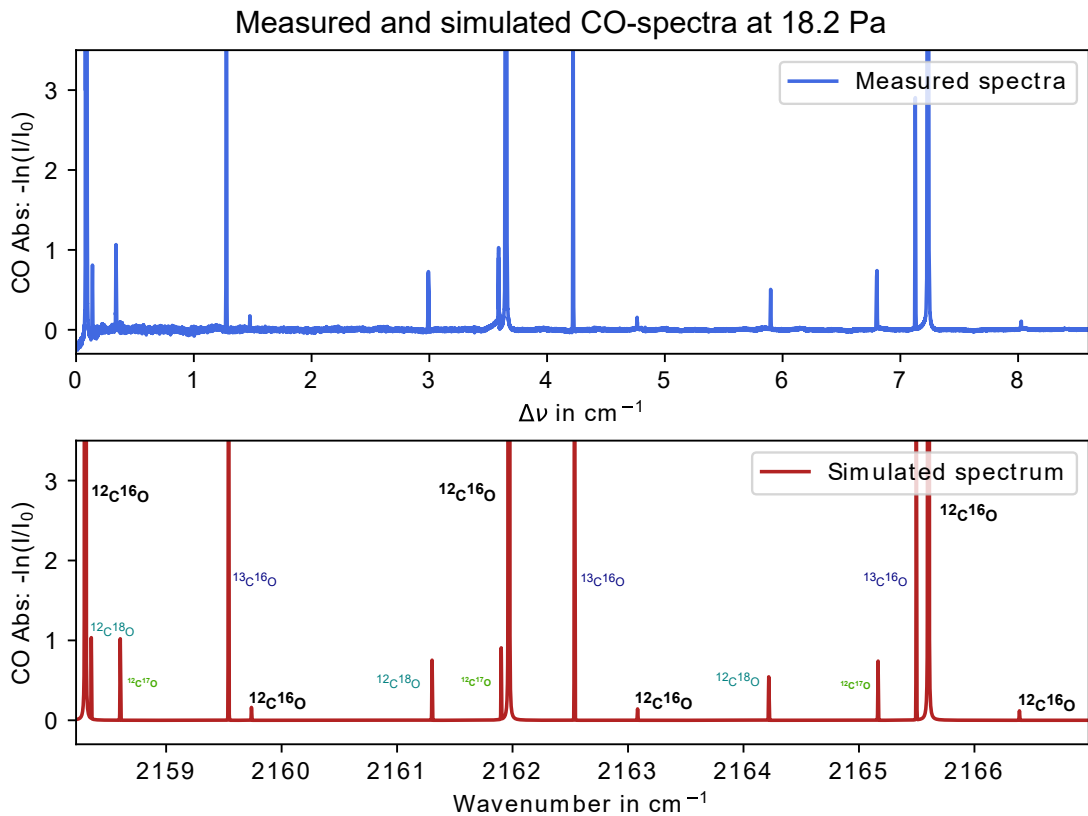


Figure 5.5: Shown on the top: Experimentally obtained Carbon monoxide spectrum after tuning the QCL over  $8.8 \text{ cm}^{-1}$  via its operating temperature. An optical pathlength of 101 m and a pressure 18.2 Pa were created inside the vacuum chamber.

Shown on the bottom: Simulated CO spectrum for an optical path lengths of 101 m and a pressure of 18.2 Pa, based on the corresponding CO-lineshape parameters of the HITRAN data base. The CO isotope responsible for the respective radiative transition is indicated and color coded.

Comparing the experimentally obtained absorption spectrum from the upper image, with the simulated Carbon monoxide spectrum from the Hitran data base on the lower image in Figure 5.5, one can see that the observed absorption line positions are nearly identical. A small deviation of the absorption signals can be observed at 2158.2 cm, where the Laser has has very little optical output power and therefore the signal to noise ratio is unfavorable.

The relative position of the experimental absorption line position can now be assigned to the theoretical position from the database, by plotting the respective experimental and theoretical line positions against each other, as is shown in Figure 5.6.

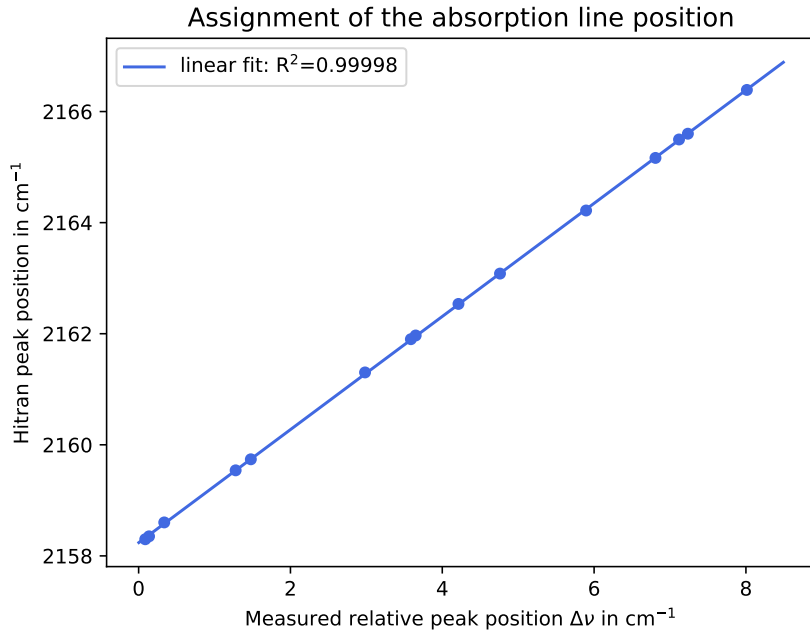


Figure 5.6: Shown is the relationship between the measured peak position of the CO absorption lines in the scanning range of the QCL with the theoretically simulated peak positions obtained from the HITRAN data base.

The linear relation indicates that the experimentally observed absorption line sequence matches with the one obtained from the HITRAN database. This observation allows for an absolute frequency assignment to all observed experimental CO-absorption lines, since a random match to another absorption line sequence can be excluded.

## 5.2 Determination of the required Laser linewidth

To perform accurate measurements of the line strength  $S$  or the partial gas pressure  $p$  with the absorption law (using TDLAS):

$$A_{\text{line}} = S \cdot n \cdot L = S \cdot \frac{p}{k_B \cdot T} \cdot L \quad (5.3)$$

it is necessary to evaluate the uncertainty contribution of the integrated absorption  $A_{\text{line}}$ , optical path-length  $L$  and the gas temperature  $T$ . While the temperature and path-length uncertainties can be accessed directly by their respective measurement device calibration, the uncertainty of the integrated absorbance has to be determined based on the measurement Laser properties. Namely the Laser-linewidth. During the measurement (using a TDLAS setup) the laser is tuned over an isolated absorption line. Since the laser has a finite linewidth the measured integrated absorbance will always deviate from the theoretically expected one.

The discrepancy between the theoretical expectation and experimental result can be simulated by comparing the two with each other. To define a theoretical value for the comparison, a CO<sub>2</sub>

## 5.2. DETERMINATION OF THE REQUIRED LASER LINewidth

---

absorption line at  $4.305 \mu\text{m}$  was taken from the HITRAN database. The absorbance and transmittance for said absorption line were determined based on the properties given in the database. The absorption-line broadening was calculated for room temperature (296K) and a pressure of  $1 \cdot 10^{-5} \text{ mbar}$ . The linewidth of the assumed Voigt profile is in the order of  $3.8 \cdot 10^{-6} \mu\text{m}$ . The theoretically expected absorbance  $A_{\text{line}}$  was then calculated by integrating over the absorption line.

The expected experimental result was generated by simulating the measurement process directly. Therefore a Gaussian Laser profile was swept over the HITRAN-CO<sub>2</sub>-absorption line. The convolution integral of the sweeping Laser ( $L_{\text{aser}}$ ) and the transmission curve of the absorption line ( $T_{\text{Hitran}}$ ) yields the expected experimental result for the transmittance ( $T_{\text{Exp}}$ ).

$$T_{\text{Exp}}(\lambda) = (L_{\text{aser}} * T_{\text{Hitran}})(\lambda) = \int_{-\infty}^{\infty} T(\tau) \cdot L(\lambda - \tau) d\tau \quad (5.4)$$

The expected experimental result for the absorbance ( $A_{\text{Exp}}$ ) can then be calculated from the determined transmittance.

$$A_{\text{Exp}} = \frac{-\log(T_{\text{Exp}})}{L \cdot c} \quad (5.5)$$

The influence of the Laser on the measurement accuracy was then determined by performing the simulation with varying Laser linewidth. The starting Laser-HWHM of:  $3.8 \cdot 10^{-6} \mu\text{m}$  was gradually reduced to its final value of  $3.8 \cdot 10^{-9} \mu\text{m}$ . The expected experimental and theoretical values of the absorbance and transmittance can then be compared and used to determine the uncertainty contribution ( $\delta A$  and  $\delta T$ ) of the Laser.

$$\begin{aligned} \delta A &= \left| \int_{-\infty}^{\infty} A_{\text{Exp}} d\lambda - \int_{-\infty}^{\infty} A_{\text{Theo}} d\lambda \right| \\ \delta T &= \left| \int_{-\infty}^{\infty} T_{\text{Exp}} d\lambda - \int_{-\infty}^{\infty} T_{\text{Theo}} d\lambda \right| \end{aligned} \quad (5.6)$$

The results of the simulation are summarized in Fig. 5.7 and Table 5.1.

## 5.2. DETERMINATION OF THE REQUIRED LASER LINewidth

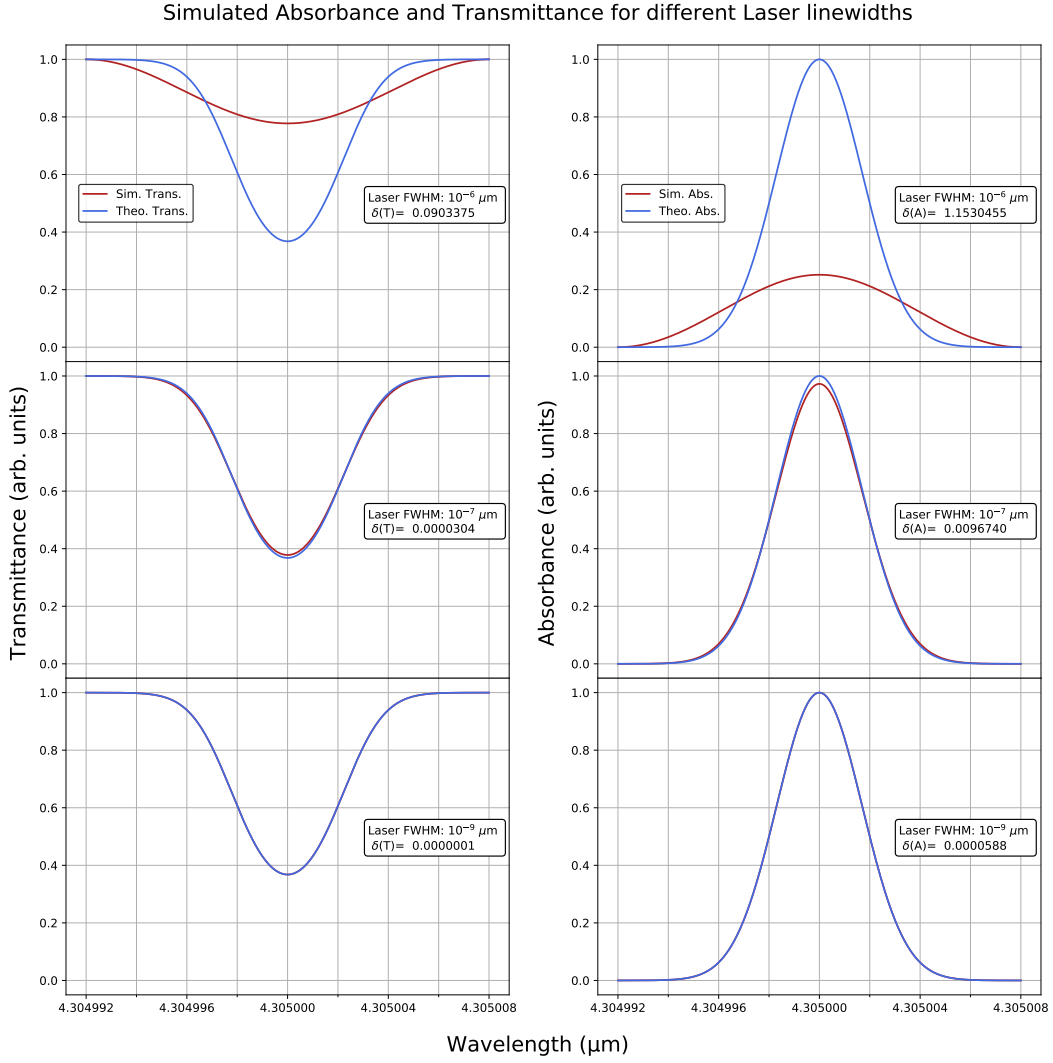


Figure 5.7: Shown are the experimentally expected (red) and the theoretically expected (blue) transmission and absorption curves of a CO<sub>2</sub> line, which is centered around 4.305  $\mu\text{m}$ . From top to bottom the corresponding Laser-linewidth are  $3.8 \cdot 10^{-6}$ ,  $3.8 \cdot 10^{-7}$  and  $3.8 \cdot 10^{-9}$ . The individual uncertainty contributions ( $\delta T$  and  $\delta A$ ) are displayed together with the Laser-linewidth that was used for the respective simulation iteration.

By reducing the linewidth of the Laser one can continuously decrease the uncertainty contribution  $\delta A$  to the integrated absorbance  $A_{\text{line}}$ . The target uncertainties for partial pressure and linestrength measurements within the QuantumPascal project are in the order of  $10^{-4}$ , when carried out with a TDLAS setup. To achieve these goals the linewidth of the quantum cascade Laser has to be at least three orders of magnitude smaller than the linewidth of the measured absorption line. Since the absorption line broadening depends on pressure, emission frequency and temperature, the exact Laser-linewidth that is required has to be calculated for each case individually. For simplicity purposes it would also be acceptable to assume a Gaussian profile for the absorption line at 4.305  $\mu\text{m}$ . Assuming that the pressure in the measurement chamber is below 1 Pa. Figure 5.8 compares

Laser HWHM ( $\mu\text{m}$ ):	$3.8 \cdot 10^{-6}$	$3.8 \cdot 10^{-7}$	$3.8 \cdot 10^{-8}$	$3.8 \cdot 10^{-9}$
$\delta T$ (arb. units):	$9.0 \cdot 10^{-2}$	$3.0 \cdot 10^{-5}$	$1.4 \cdot 10^{-6}$	$1.2 \cdot 10^{-7}$
$\delta A$ (arb. units):	$1.2 \cdot 10^0$	$9.7 \cdot 10^{-3}$	$1.6 \cdot 10^{-4}$	$5.9 \cdot 10^{-5}$

Table 5.1: Comparison of different Laser-linewidths and their influence on the uncertainty contributions  $\delta T$  and  $\delta A$ . The target uncertainty of  $10^{-4}$  for  $\delta A$  is reached with a Laser-linewidth of  $3.8 \cdot 10^{-9} \mu\text{m}$ .

the contribution of the Gaussian and Lorentzian line-broadening to the total absorption-line linewidth. Up to a pressure of 1 Pa the pressure dependent Lorentzian line broadening is at least three orders of magnitude smaller than the temperature dependent Gaussian line broadening.

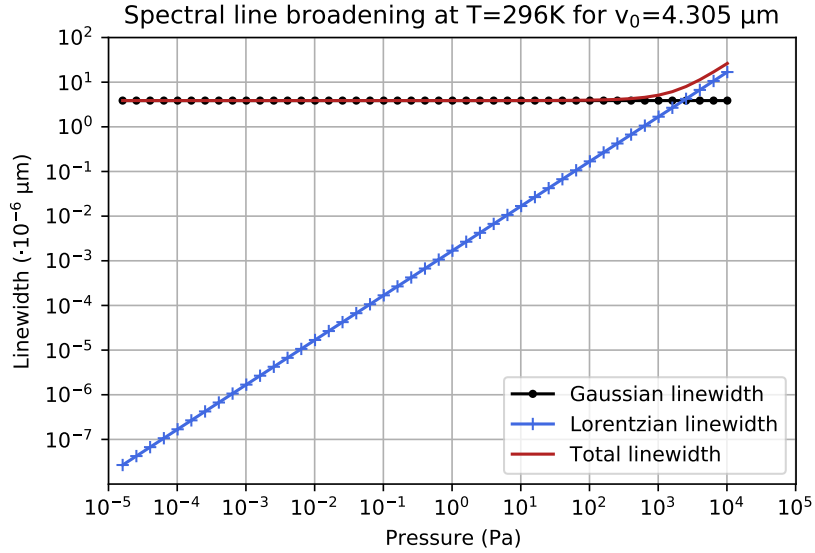


Figure 5.8: The graphic illustrates the pressure dependent absorption linewidth broadening for an exemplaric CO<sub>2</sub> line at 4.305  $\mu\text{m}$ . Shown are the Gaussian, Lorentzian and the total linewidth from the high vacuum region up to atmospheric pressure. All data was taken from the HITRAN database [47] [48].

### 5.3 Reducing Laser-linewidths and Laser locking

As shown in the previous sections, Quantum cascade Laser provide an excellent single mode tuning range at high optical output powers. The intrinsic linewidth for quantum cascade lasers is given by the Schawlow-Townes limit [51] and is caused by white noise. It can be as low as a few Hertz and depends on several factors:

$$\Delta\nu_{QCL} = \frac{4\pi h\nu(\Delta\nu_c)^2}{P_{out}} \quad (5.7)$$

The photon energy  $h\nu$ , the output power of the Laser  $P_{out}$  and the laser-resonator bandwidth  $\Delta\nu_c$ . Additional noise from other sources, like thermal or electrical noise from the Laser driver, further broaden the emission linewidth of semiconductor Lasers. If these noise sources are not addressed, the typical emission linewidth of a QCL is in the order of a few Mega Hertz, which is several orders of magnitude higher than the theoretical lower limit predicted by Schawlow and Townes. Since narrow linewidth Laser sources in the MIR are crucial for high resolution spectroscopic applications, extensive research has been performed in the last several years. Mainly with the goal to: quantify the influence of frequency noise on the Laser Linewidth [20] and reduce Laser linewidth with different experimental approaches. Such as locking a Laser to: an optical delay line [55], micro resonators like a whispering Gallery [15], V-shaped cavities [26], MIR frequency combs or sub-doppler CO<sub>2</sub> transitions [9].

The Laser linewidth optimization approach, chosen for this thesis, combines an ultra low current noise Laser driver with locking the QCL to a high finesse Fabry P  rot cavity. The low noise Laser driver is required to minimize electrical noise that is applied to the semiconductor chip when tuning or running the QCL. The optical lock to a FP-cavity is implemented to further reduce the frequency noise by stabilizing the Laser to an optical frequency reference, namely the sharp transmission peaks (TEM<sub>00</sub> modes) of the resonator.

Figure 5.9 shows the transmission signal of a single TEM<sub>00</sub> mode of the FP-cavity which is used for locking the QCL. Since the TEM<sub>00</sub>-mode transmissions are separated in frequency by 1.5 GHz (cavity length of 10 cm), one can tune the absolute emission frequency of the laser to any arbitrary value, by changing the operating temperature, and then lock it to the closest TEM<sub>00</sub>- mode of the FP-cavity.

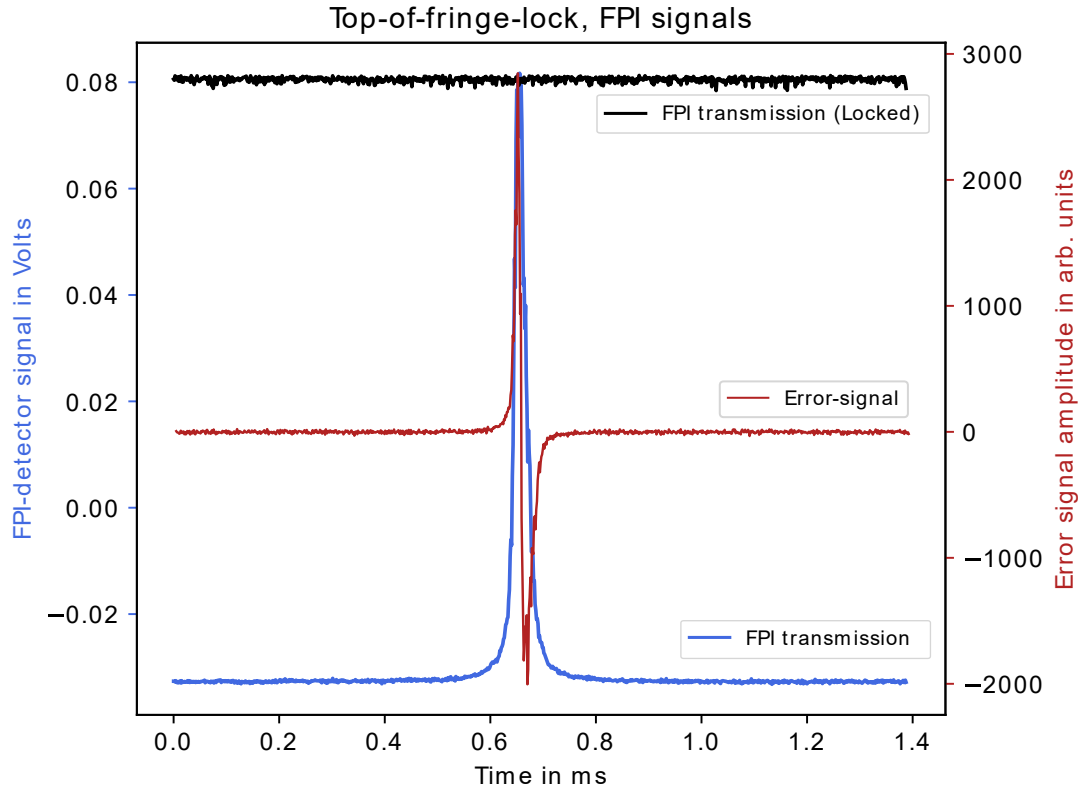


Figure 5.9: Shown are the transmission signals behind the FP-Cavity, before the lock is engaged (blue), after the lock is closed (black) and the generated error-signal (red).

To stabilize the Laser frequency to the FP-cavity reference, the Lock-In technique was used which could be implemented digitally by using a FPGA-chip (Toptica: Digilock) which itself is connected to the Laser driver. The FPGA has two modulation output channels, which allow scanning of the Laser frequency by applying voltage ramps to the modulation input of the Laser driver. On the first output channel of the FPGA a periodic triangle function with an amplitude of 0.2 V is applied. The scanning amplitude is chosen so that only one transmission peak can be observed on the detector as is shown in Figure 5.9.

For the Lock-In technique to work, a second, fast modulation channel is required. Figure 5.10 illustrates the operating principle of the Lock-In technique. The FPGA applies a fast (between 1kHz and 1 Mhz) demodulation with a very small amplitude to the second input channel of the Laser driver. By quickly demodulating the signal, one can generate the derivative of the input signal that is observed on the detector. This, experimentally obtained, derivative signal can then be used as an Error signal for a pid controller. The pid controller takes the Error signal as information input and optimizes the voltage, applied to the fast input channel of the Laser driver. So that the emission frequency of the Laser is constantly forced to the center frequency of the TEM<sub>00</sub> mode. This works since the error function has a zero crossing at the peak position of the Cavity transmission signal and the pid controller is set to stabilize the error signal to zero. Once the Lock is engaged, the slow modulation on the first channel can be turned off and instead

be used to compensate for slow frequency changes (e.g. caused by temperature changes)

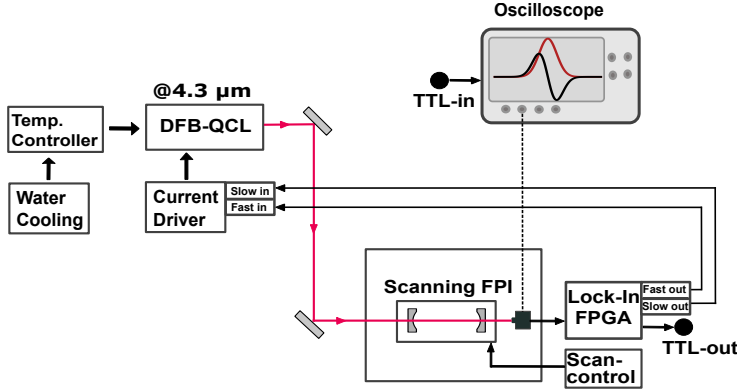


Figure 5.10: Shown is the basic operating principle of the Lock-In technique as it was implemented in this thesis, together with all optical and electrical components that were required.

The disadvantage of locking a Laser to an external frequency reference is that it can not be directly tuned in its emission frequency anymore. Since this property is important for TDLAS, one can instead tune the frequency reference to which the Laser is locked to. This allows for an indirect frequency modulation of the Laser while still benefiting from the linewidth narrowing of the Laser Lock. When using a Fabry Pérot cavity as a frequency reference this indirect tuning can be achieved by changing the length of the resonator. FP-cavities are often times used as a scanning Fabry Pérot interferometers and come with an integrated piezoelectric transducer. This transducer is used to periodically modulate the cavity length by compressing an expanding transducer with the help of periodic voltage ramps. When the QCL is locked to a  $\text{TEM}_{00}$ -mode of the FP-cavity and the cavity length is periodically modulated, the indirect modulation of the emission frequency is achieved. However, these piezoelectric transducers often times tune the Laser frequency in a non-linear fashion due to hysteresis effects during the scan. Therefore additional care is required when calibrating the emission frequency of the Laser.

## 5.4 Frequency calibration

For TDLAS, the measured absorption signals are generally integrated over the frequency, to obtain the integrated absorption:  $A_{\text{line}}$  of the signal. This requires precise knowledge of the relative frequency change while the Laser is scanned. To achieve this, a transversally coupled Herriott-Cell (TAC) was used as an optical interferometer and absolute frequency standard. The laser light enters the TAC perpendicular to the classical optical axis, as is shown in Figure 5.11 which illustrates the parts of the experimental setup that are required to calibrate the frequency axis. The laser light is coupled in and out of the TAC with the help of a very thin and highly reflective silver-plate. The silver plate is positioned, so that only 50 percent of the Laser light is coupled into the Herriott cell with an optical pathlength of 6.429589 m and the other 50 percent are sent directly onto the photodetector. During a measurement the QCL is tuned to its emission frequency and one can observe an interference pattern on the detector where the interference

fringes are separated in frequency by:

$$\Delta\nu_{TAC} = \frac{c}{n \cdot L} \quad (5.8)$$

where n is the refractive index of the gas, L is the optical pathlength of the TAC and c is the speed of light. To avoid density fluctuations and decrease vibrations, which negatively influence the interference signal, the TAC is integrated into a UH-vacuum chamber and placed on a vibration damped optical table. Assuming that the refractive index in vacuum is 1, one obtains a frequency separation of the individual interference fringes of  $\Delta\nu_{TAC} = 46.627$  MHz.

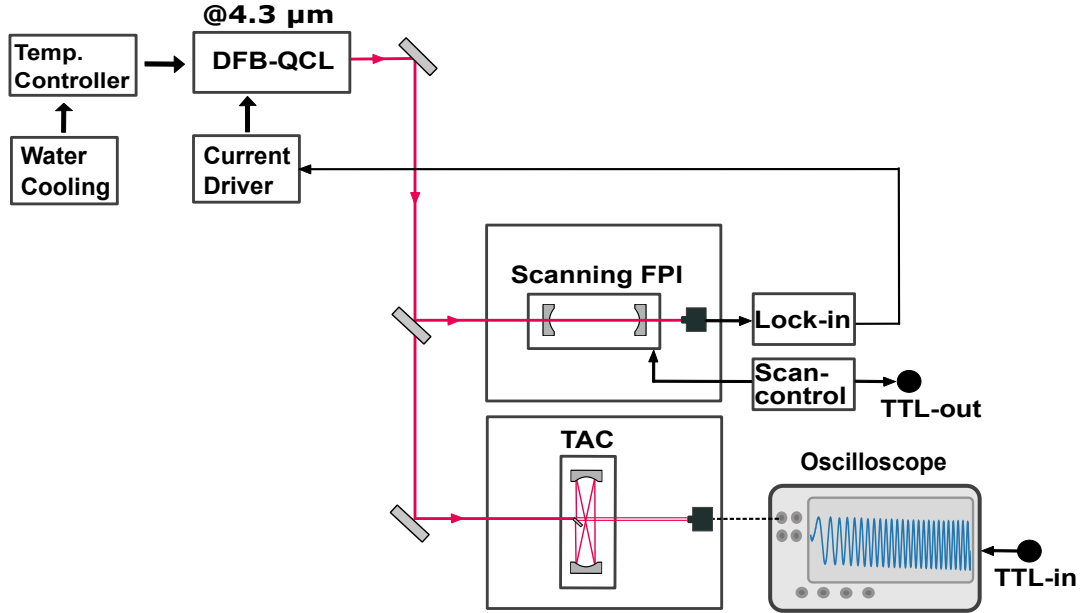


Figure 5.11

As shown in the previous section, the QCL is locked to a Fabry-Pérot resonator to narrow the Laser linewidth by reducing the frequency noise. In order to tune the Laser while it is locked, the Fabry-Pérot length is periodically modulated. This experimental approach results in a slightly nonlinear tuning of the Lasers emission frequency, which has to be considered when calibrating the frequency axis. (And should be considered even for direct tuning of the Laser since self heating effects can cause non-linear tuning as well). Figure 5.12 shows the interference signal that is obtained on the photo detector behind the TAC. The length of the FPI was modulated at a high frequency of 200 Hz and the shown signal covers the first 1.7 ms of the scan, where the non-linearity is most significant.

One can then perform a fast Fourier transformation of the interference pattern to visualize the frequency change during the QCL-scan. The result of the FFT is visualized in a spectrogram which plots the current frequency of the time series against the respective measurement time. The spectrogram reveals a clearly visible non-linear chirp of the time series. This chirp was then interpolated, rather than fitted as the functional relationship is not fully known due to many

simultaneously occurring effects (e.g self heating or hysteresis effects of the piezo). With the interpolated chirp signal one can then correct and linearize the interference signal together with the measured absorption signals. The linearized signal is shown in Figure 5.12 on the right.

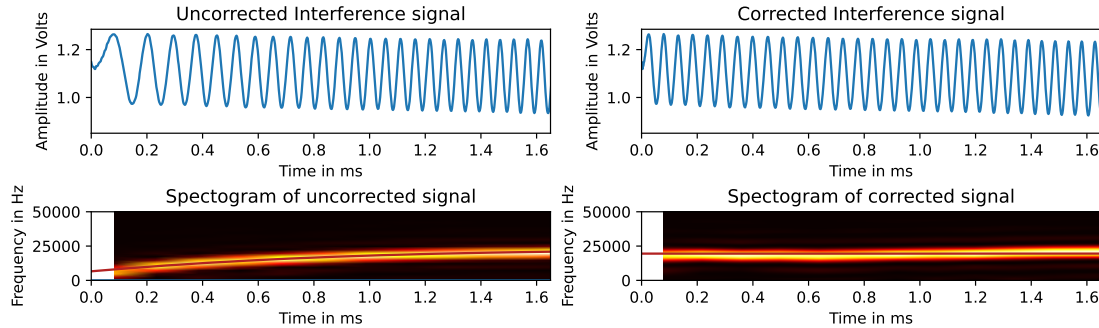
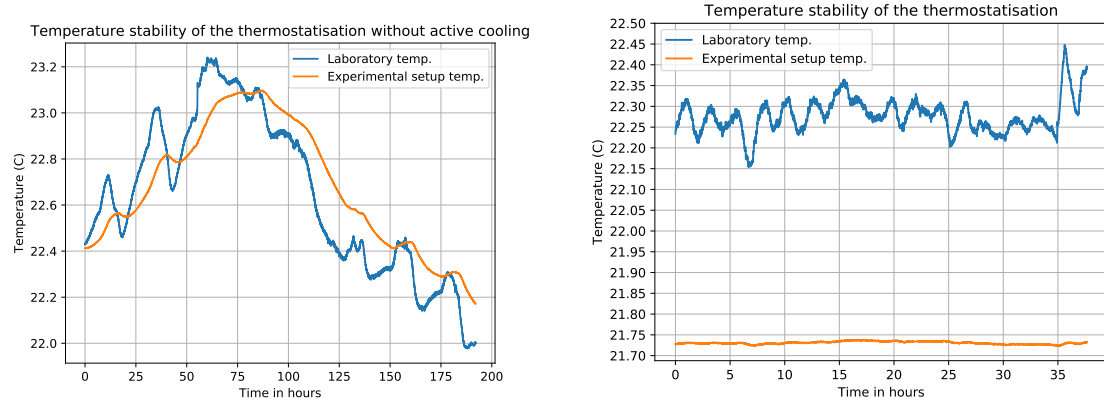


Figure 5.12: Shown on the top left: The measured interference signal for the first 1.7 ms of the scan duration.  
 Shown on the bottom left: Shown is the spectrogram of the interference signal.  
 Shown on the top right: Linearized signal after correcting for the chirp.  
 Shown on the bottom right: Spectrogram of the corrected interference signal.

An alternative method to the Fourier analysis is a direct investigation of the interference pattern. One can obtain the inverse of the correction function by plotting the interference peak distance against the respective measurement time.

## 5.5 Temperature assessment

The vacuum chamber containing the measurement gas is integrated into a fully thermostatized environment, which is shielded against room temperature fluctuations with a Styrodur enclosure. A precision water bath can be used in combination with several radiators to stabilize the temperature inside the enclosure (and inside the vacuum chamber) to any arbitrary temperature close to room temperature (between 21-24 °C). Figure 5.13 shows the temperature inside the the enclosure with and without active cooling for a several hour-long time period.



(a) No active cooling: Shown is a comparison of the room temperature in the laboratory and the temperature within the thermal insulation for the time period from 24.2.2021 to 03.03.2021. The room temperature follows the outdoor temperature since the AC is not properly adjusted. The thermal insulation results in a delayed temperature increase/decrease with significantly less total amplitude change.

(b) With active cooling: The PID control of the AC was adjusted and an active temperature control was added within the thermal insulation.

Figure 5.13: Temperature profiles within the thermally insulated enclosure.

The temperature stability within the thermal insulation was better than 25 mK (peak to peak) for a 38 hour long period.

During TDLAS measurements, the gas temperature is assessed with two 25 Ohm standard platinum resistance thermometers (SPRT) which are connected to a measurement bridge (Isotech:MircoK 70) and a reference resistor. Over a period of 2 years, the SPRTs were calibrated three times against the water triple point and the Gallium melting point in the temperature laboratory of the PTB. During the calibration, the same measurement bridge was used, which compensates for the self heating of the SPRT-sensors which require an operating current of 1 mA. The resistance of the SPRT is assessed with a four wire measurement and then internally compared to the reference resistor. The reference resistor itself is integrated into a temperature controlled box which operates at 23 °C. With the help of the calibration certificate the measured resistances of the SPRTs can then be converted into temperatures.

The SPRTs together with four additional PT100 sensors are then put in direct contact with the

vacuum chamber to assess the temperature profile of the gas during the TDLAS measurement. The PT100 sensors were calibrated against the SPRTs in a high precision calibration bath (CIK: Kambic) with a temperature stability of 1 mK.

## 5.6 Pressure assessment

During the linestrength assessment the Carbon monoxide pressure was modulated to approach and measure different pressure points. Pressure increases were adjusted using a needle valve while pressure decreases were realized with pumping out the gas with the help of a turbomolecular pump. Figure 5.14 shows an exemplaric pressure modulation for TDLAS measurement campaign.

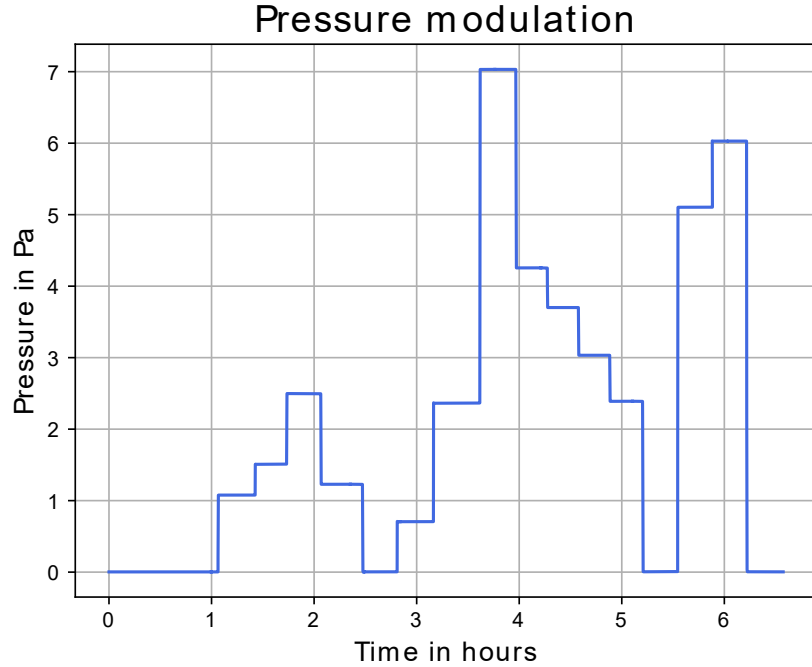


Figure 5.14: Exemplaric pressure modulation.

The pressure is increased step wise until an arbitrarily chosen maximum value is reached and then decreased again so that similar pressure values can be assessed under different experimental conditions. This is done to ensure that the pressure modulation and demodulation has no influence on the experimentally determined absorption:  $A_{line}$ . After every modulation cycle a zero measurement is performed, which is later used to determine the transmission intensity  $I_0$ , when no gas is present within the multipass absorption cell.

Pressure measurements are carried out with one of three different pressure sensors. The sensors cover different pressure regions and are chosen accordingly to achieve the lowest uncertainties and highest performance. A Spinning rotor gauge (SRG,  $10^{-5}$  to  $10^2$  Pa), Capacitive Diaphragm Gauge (CDG,  $10^{-1}$  to  $10^2$  Pa) and a quartz based pressure standard (1 and  $10^5$  Pa) were used. The CDG and the Quartz based standard were calibrated in the pressure department of the PTB and have been compared to the state of the art static expansion system.

### 5.6.1 Thermal transpiration effects

For many pressure measurements, between between  $10^{-2}$  and 100 Pa, a capacitive diaphragm gauge (CDG) was used. CDG's are sensitive to temperature variation and are therefore often times operated and stabilized to temperatures above room temperature (generally between 40 and 45 °C). Due to the temperature difference between the vacuum chamber and the pressure sensor one can observe the so called thermal transpiration effect. If the CDG is connected to the vacuum chamber via a tube, the pressure  $P_2$  of the sensor is not equal to the pressure  $P_1$  inside the vacuum chamber if the overall pressure is low enough for the system to be in the molecular regime[32].

Whether the system is in the molecular or continuous regime is defined by the Knudsen number, which is given as the ratio of the mean free path lengths of the gas particles ( $\lambda$ ) with respect to the connecting tube diameter ( $d$ ):

$$K_n = \lambda/d \quad (5.9)$$

For Knudsen numbers greater than 10, the system is in the molecular regime. Between 0.1 and 10 one can observe the transitional flow and for Knudsen numbers below 0.01 the system is in the continuous regime.

If the mean free path of the gas molecules is much greater than the tube diameter (molecular regime) the ratio of the two pressures  $P_1$  and  $P_2$  are equal to the Knudsen number:

$$K_n = \frac{P_2}{P_1} = \sqrt{\frac{T_2}{T_1}} \quad (5.10)$$

while they are equal in the continuous regime. For the intermediate region, between the molecular and the continuous region the thermal transpiration value  $\frac{P_2}{P_1}$  ranges between the two extremes [56].

For precise pressure measurements with CDGS below 10 Pa, knowledge of the thermal transpiration ratio is crucial. Knowledge of this effect can be obtained by calibrating the CDG against a pressure standard like the continuous-expansion-system, which does not operate at elevated temperatures. Figure 5.15 shows the respective calibration data which illustrates the thermal transpiration effect as well. The deviation between the two pressure values  $P_1$  and  $P_2$  can be as large as 4 %. Using the calibration data as a correction of the measured CDG-pressure allows the thermal transpiration effect to be excluded and corrected in all further measurements. The calibration was performed by the Vacuum Metrology working group of the PTB.

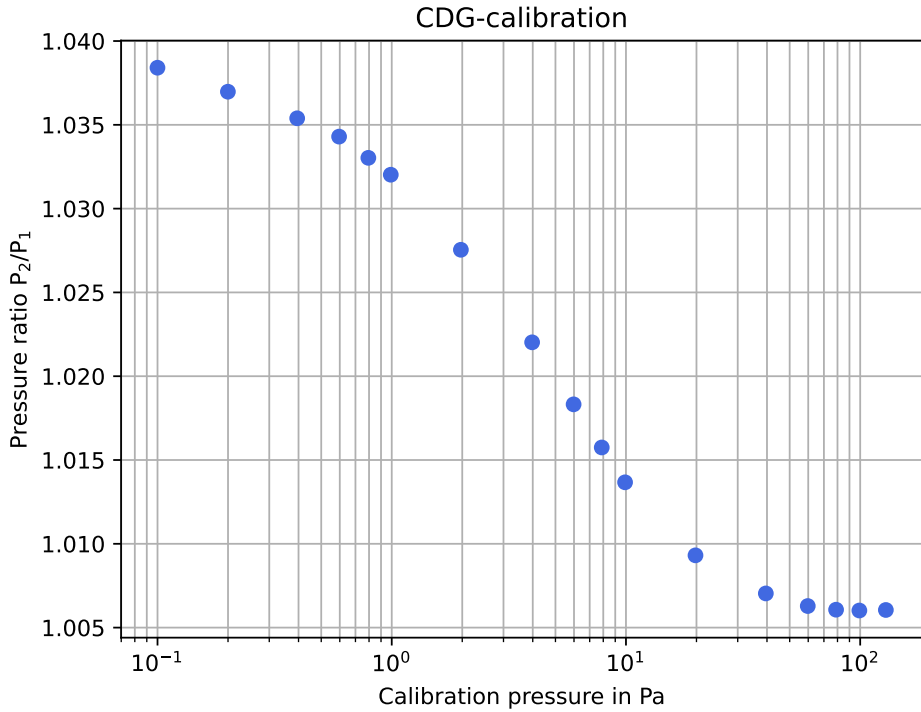


Figure 5.15: Shown is the calibration data of the CDG used for pressure measurements during this thesis. The pressure ratio  $P_2/P_1$  is plotted over the respective calibration pressure to illustrate the thermal transpiration effect over a wide pressure range.

## 5.7 TDLAS measurements

After the preliminary experiments were conducted and the experimental system was characterized, TDLAS measurements were performed to investigate the linestrength  $S$  of Carbon Monoxide in the spectral region from  $2158$  and  $2170\text{ cm}^{-1}$ , with the complete experimental setup shown in 5.1. The linestrength of any absorption line in the spectral region can be obtained by measuring the integrated absorbance  $A_{line}$  against the respective gas pressure  $p$ :

$$S = \frac{A_{line} k_B T}{p L} \quad (5.11)$$

With knowledge of the gas temperature  $T$  and the absorption pathlength  $L$ , one can obtain the linestrength  $S$  from the linear relationship of the measure parameters.

### 5.7.1 Pressure dependent transmission and absorption signals

For an initial linestrength measurement, the QCL was tuned to an emission frequency of  $2165.6\text{ cm}^{-1}$  and locked to the closest  $\text{TEM}_{00}$  mode of the Fabry Pérot cavity. The FPI was then indirectly tuned so that the emission frequency of the Laser could be scanned over  $0.062\text{ cm}^{-1}$ . The non-linear frequency tuning was compensated for by the technique described in section 5.4. The CO gas pressure was step wise increased from  $0.2$  to  $5\text{ Pa}$  during the measurements and the

respective transmission and absorption curves are shown in Figure 5.16. The transmission intensity  $I_0$  is obtained on the detector when the vacuum chamber is completely evacuated.

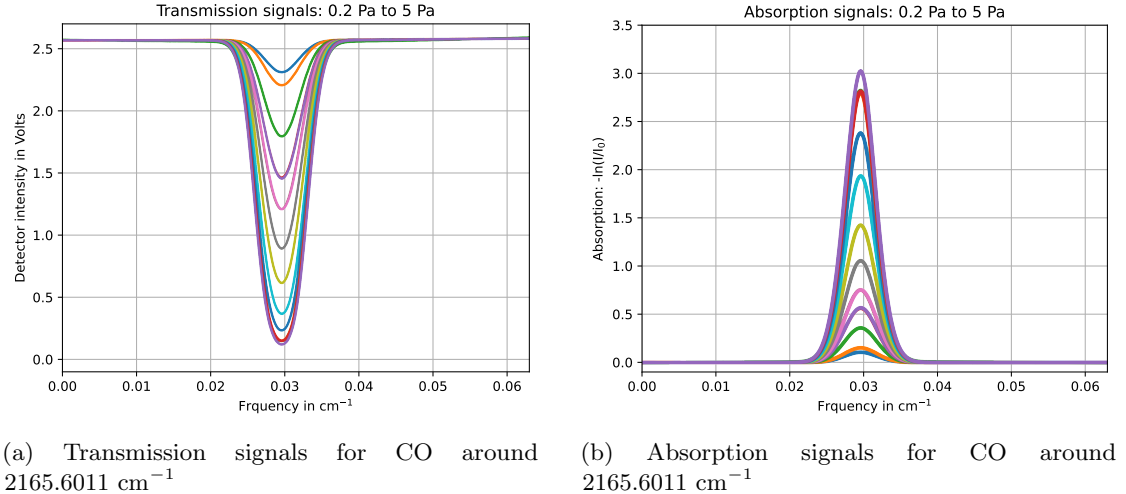


Figure 5.16

One can observe that both, the transmission and absorption signals scale with increasing pressure. However, only the absorption scales linearly with pressure due to the non-linear relationship between the transmission and absorption.

### 5.7.2 Comparison with simulation and fitting models

To obtain the integrated absorbance  $A_{line}$ , one can either directly integrate the experimental data or fit the experimental data with an appropriate line shape function e.g a Gaussian-, Lorentz-, Voigt- or Hartmann-Tran-profile. Where the Hartmann-Tran profile [41] is the currently recommended line-shape standard (e.g by the HITRAN community), as it accounts for most currently known effects that further alternate the natural line shape.

Figure 5.17 and 5.18 show the absorption signal of two individual measurements at a partial CO-pressure of 1 Pa and 5 Pa respectively. The experimentally obtained data is then compared a simulated absorption spectra utilizing the Hartmann-Tran profile and three different fitting models (Gaussian, Lorentz, Voigt). The simulated spectra were generated with the same environmental influences, that were present during the experiment: A gas temperature of 296K, a pressure of 1 (or 5) Pa and an absorption pathlength of 101 m. The remaining gas parameters, required for the simulation, could be obtained from the HITRAN database directly.

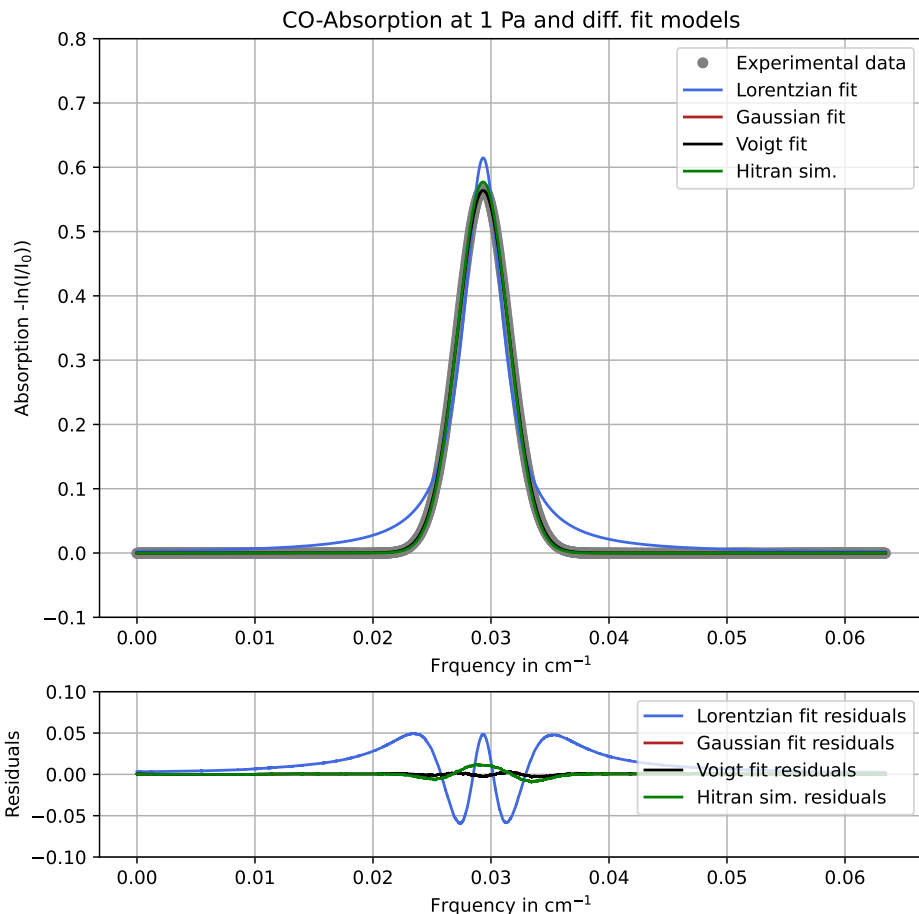


Figure 5.17: Absorption spectrum of CO at a pressure of 1 Pa in comparison with four different models.

The residuals obtained from comparing the experimental data set with the respective fits and the simulation are shown at the bottom of 5.17. As expected, for pressures far below 100 Pa, the Lorentzian broadening is small which results in the greatest residuals for the Lorentzian fitting model. At a pressure of 1 Pa the pressure induced Lorentzian broadening makes up for less than a percent of the total spectral line broadening of the absorption signal. Which means that for small pressures a Gaussian and a speed-dependent-Voigt model yield similar results and the residuals of the Voigt model are only slightly lower than that of the Gaussian fit. For higher pressures, e.g 5 Pa, as shown in Figure 5.18 the difference in the residuals between the Gaussian and Voigt fitting approach are more significant.

Fitting model / Simulation:	Lorentzian	Gaussian	SD-Voigt	Hartmann-Tran-sim.
Integrated residuals:	xx	xx	xx	xx

Table 5.2: Comparison between different fitting approaches and theoretical simulation.

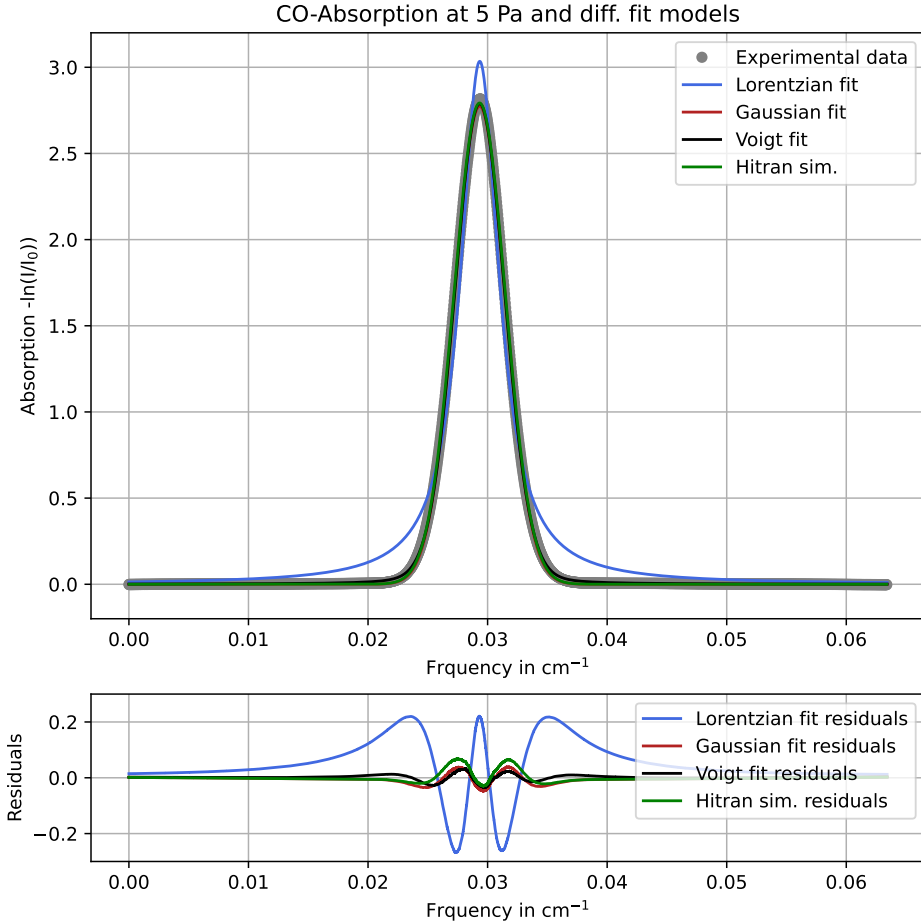


Figure 5.18: Absorption spectrum of CO at a pressure of 5 Pa in comparison with four different models.

When looking at the residuals between the experimental data and the theoretical simulation, one can observe a similar characteristic as with the Gaussian and Voigt fit. Initially it seems as the residuals are overall deficient, however when integrating over the complete spectrum the total integrated residuals of the theoretical simulation are superior to those of obtained from the two fitting models. Table 5.2 summarizes the comparison of the experimental data with the simulation ad fitting models.

After choosing the fitting model which yields the smallest deviation from the experimental

data, one can then either integrate over the respective fitting function or directly integrate the experimental data to obtain  $A_{line}$ .

### 5.7.3 Carbon monoxide line strengths

Experimental linestrength measurements for Carbon monoxide were carried out for five different absorption lines in the spectral region between 2158 and 2170 cm<sup>-1</sup>. Including three R-branch transitions of <sup>12</sup>C<sup>16</sup>O, one R-branch transition of the first isotopologue <sup>13</sup>C<sup>16</sup>O and another R-branch transition of second isotopologue <sup>12</sup>C<sup>18</sup>O.

Since the individual absorption lines, in the observed frequency region, have significantly different linestrengths (between 10<sup>-23</sup> and 10<sup>-19</sup>) one has to adjust the optical path length between measurements, to investigate different absorption lines at similar partial pressure values. This is required because often times the strong absorption lines of the spectrum are already saturated before the weak absorptions can be detected. Alternatively one could operate the Herriott-Cell at the same optical pathlength for all the different absorption lines and instead utilize different calibrated pressure sensors for the respective pressure regions. However this requires extensive calibration work, for a wide array of different pressure sensors and vacuum ranges.

During this thesis a movable, vacuum compatible Herriott cell was utilized which can be used to adjust the optical path lengths between measurements. Unfortunately the electronics required to drive the vacuum precision motor of the Herriott-Cell broke and could not be repaired in time due to consecutive global crises and the resulting supply bottlenecks. As an alternative the Herriott-Cell was tuned to an optical pathlength of 101 m and a second absorption path, with an optical pathlength of 27 cm, was created within the same vacuum chamber. These two, separate optical pathlength were chosen so that they are around four orders of magnitude apart from each other, just like the linestrength of the different absorption lines. Allowing for the observation of the strong and weak absorption line at similar partial pressures but very different optical pathlength.

For the individual linestrengths measurements, the appropriate optical path lengths was chosen, and then the CO-pressure was adjusted to various partial pressure plateaus as described in the "Pressure assessment" section 5.6. The integrated absorption  $A_{line}$  is the plotted against the respective pressure, as well as  $P \cdot L \cdot (k_b \cdot T)^{-1}$  to obtain the linestrength from the slope of the linear relation ship between the two experimentally measured properties. Figure 5.19 shows the measurement results for the <sup>13</sup>C<sup>16</sup>O absorption at 2169.198 cm<sup>-1</sup> together with the residuals to the linear fit. The optical pathlength for the measurement was set to 27 cm.

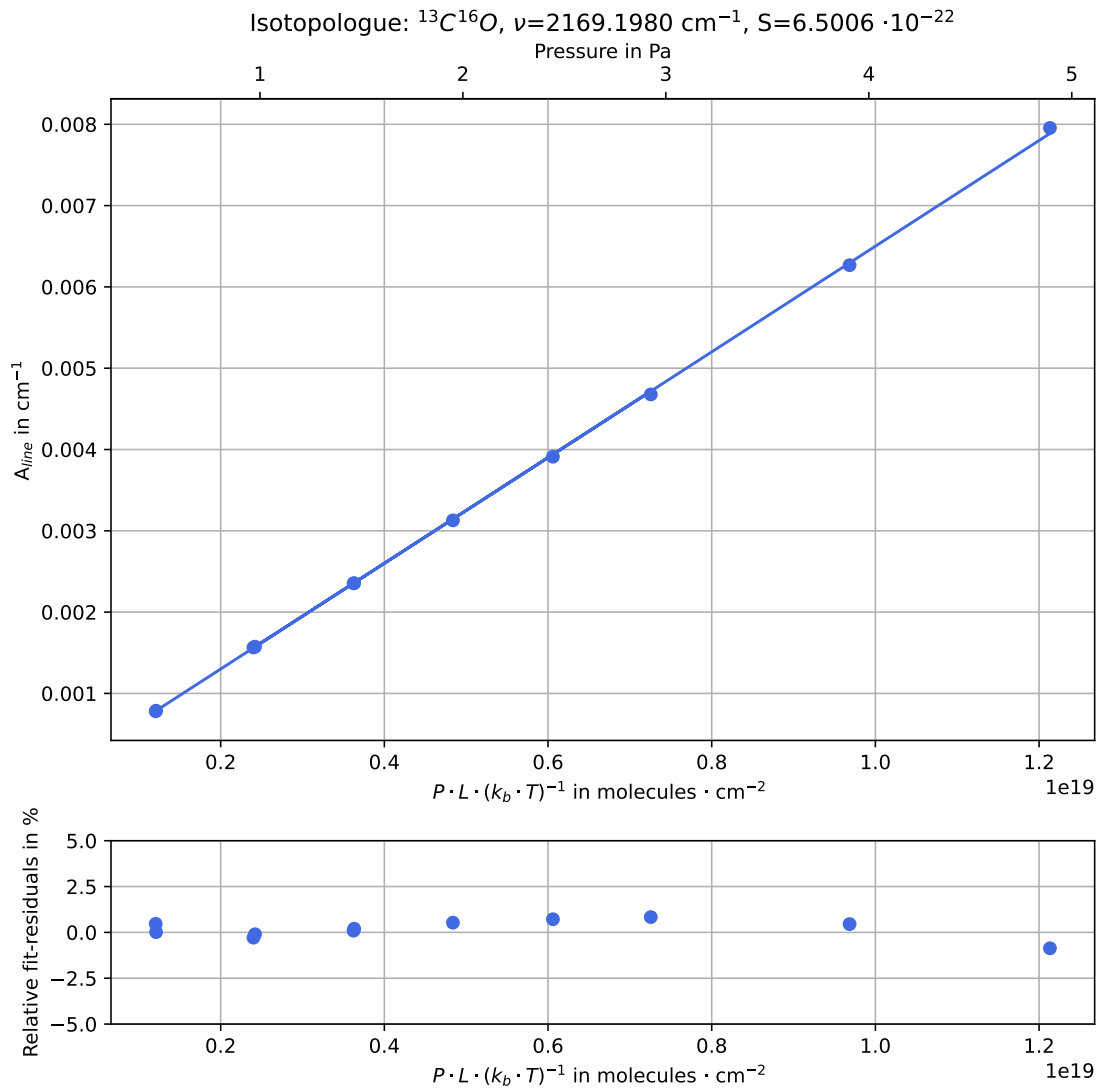


Figure 5.19: Shown is the linestrength measurement for the  $^{13}\text{C}^{16}\text{O}$  absorption at  $2169.198 \text{ cm}^{-1}$ . The second x-axis at the top shows the respective measurement pressure. Below the linear plot, the relative measurement residuals are shown in %.

The experimental results for the three R-branch transitions of  $^{12}\text{C}^{16}\text{O}$  are shown in Figure 5.20. For these strong absorption lines, the Herriott-Cell with an optical pathlength of 101 m was required and utilized.

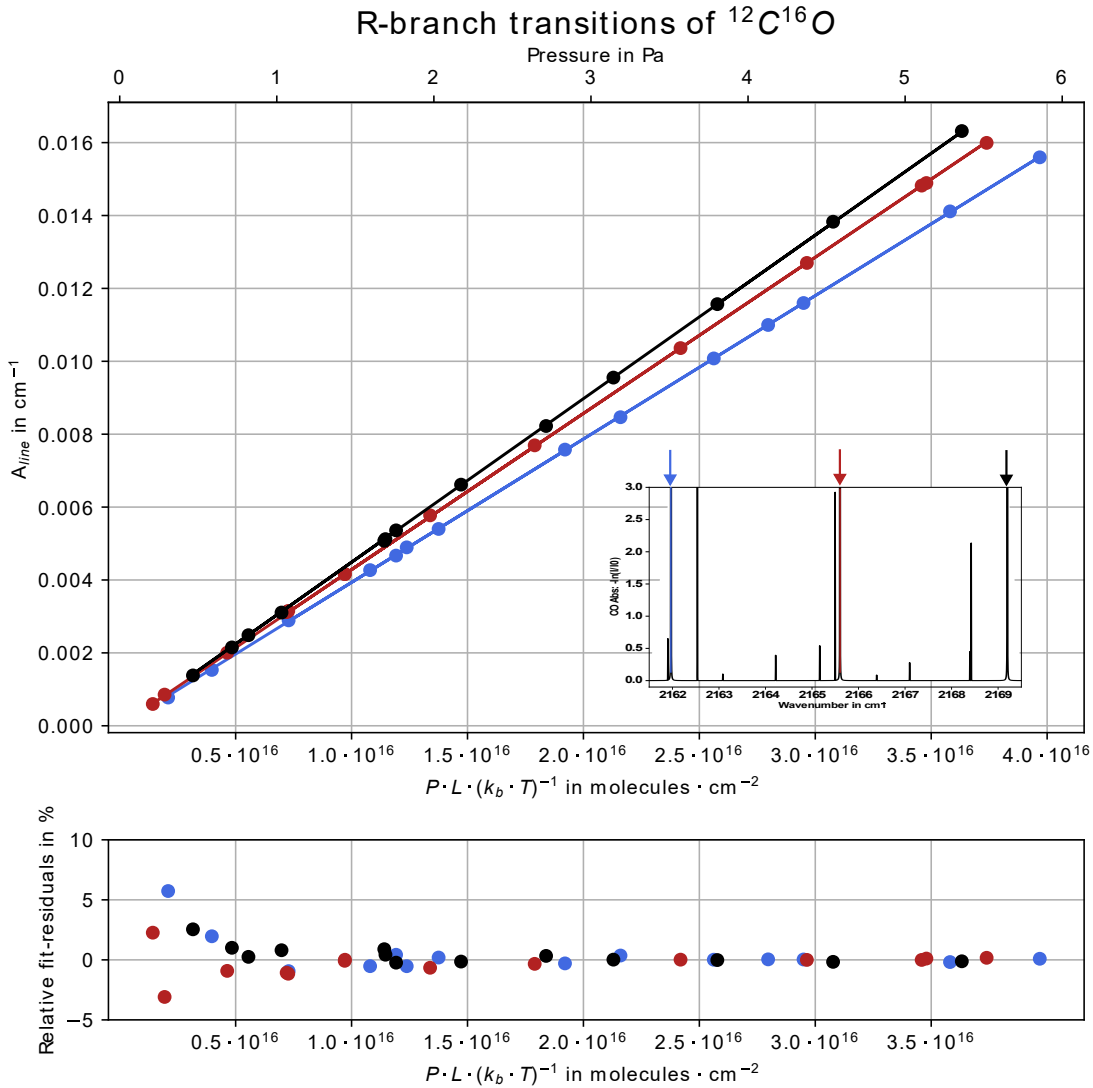


Figure 5.20: Shown are the R-branch transitions of  $^{12}\text{C}^{16}\text{O}$  in the measurement region between  $2158$  and  $2170 \text{ cm}^{-1}$ , together with the linear fit residuals in the lower graphic. The second x-axis at the top again clarifies the respective measurement pressure. The small inlet is shown to illustrate which absorption lines which were investigated.

The experimentally determined linestrengths for all measurements are compared to the Hitran values in table 5.3

Line position in $\text{cm}^{-1}$ :	2161.9682	2165.6010	2169.1980	2164.2185	2162.5364
Exp. linestrength:	xx	xx	xx	xx	xx
HITRAN linestrength:	xx	xx	xx	xx	xx

Table 5.3: Comparison experimental and HITRAN linestrengths.

## 5.8 TDLAS as a pressure standard

With the experimentally determined linestrengths one can then use the TDLAS setup as a transfer standard for CO partial pressures. The linestrength are used as an input parameter and one can utilize the measurement formula to measure pressure:

$$P = \frac{A_{\text{line}} k_B T}{SL} \quad (5.12)$$

Figure 5.21 illustrates the pressure range that can be covered with the built TDLAS system and the two different optical path lengths. Pressures as low as  $7 \cdot 10^{-4}$  Pa can still be resolved at an optical pathlength of 101 m utilizing the strong absorption lines of the given spectrum. The upper pressure range is just below 100 Pa and can be covered with a weak absorption line at  $2162.5364 \text{ cm}^{-1}$ .

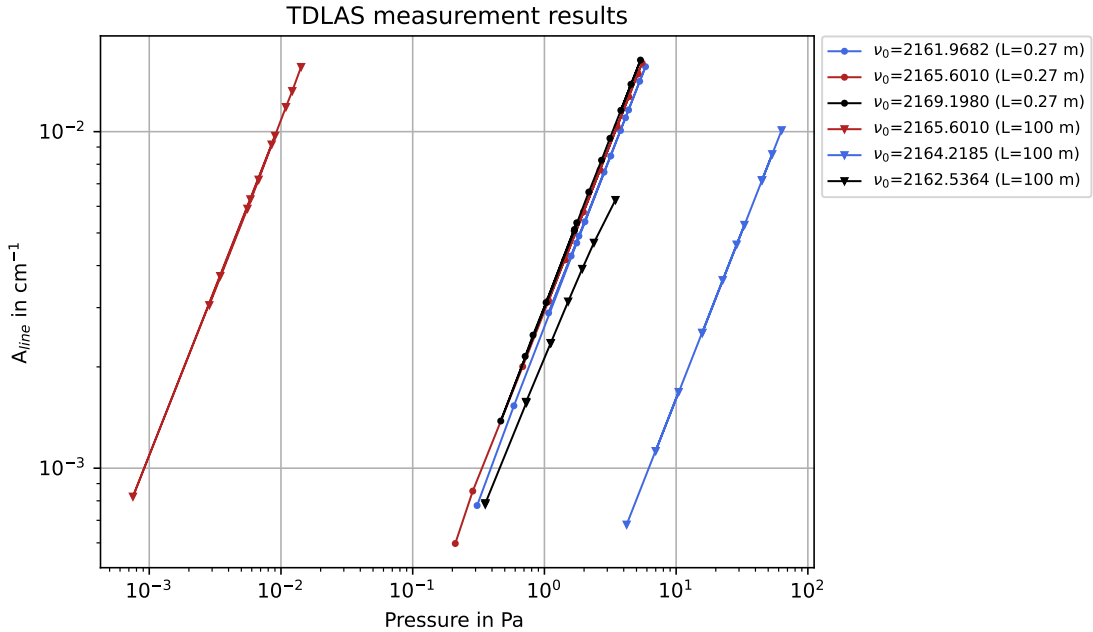


Figure 5.21: Shown is the pressure range that is covered by each individual absorption line in the given spectral region with the described optical path lengths.

### 5.8.1 Outlook and improvements

As shown in the previous section TDLAS can be utilized as a partial pressure standard for Carbon monoxide for a pressure range between  $10^{-4}$  and  $10^2$  Pa. However, not the complete pressure scale can be realized with the current setup. This is due to the inability to change the optical pathlength between more than two different values (101 and 0.27 meters). With a functioning vacuum translation stage for the Herriott-Cell the optical path length can be changed much more flexible as is shown in Figure 5.22. The graphic was made before the translation stage was damaged and illustrates the different closed configurations of the Herriott-Cell. The distance between the two mirrors was increased by translating one mirror further away from the other and the distance change was measured with a Laser interferometer. During the translation, the Laser light intensity that was transmitted through the Herriott-Cell was observed on a photo detector. The mirrors have a finite reflectivity  $R < 1$  which means that the observed detector intensities directly scale with the optical pathlengths of the Herriott-Cell configurations. Many different configurations and optical pathlengths (between 1 and 101 m) are possible, which could significantly improve the utilization of the TDLAS setup as a pressure standard. The complete pressure scale could then be covered by adjusting either the absorption line or the optical pathlengths of the Herriott-Cell or a combination of both.

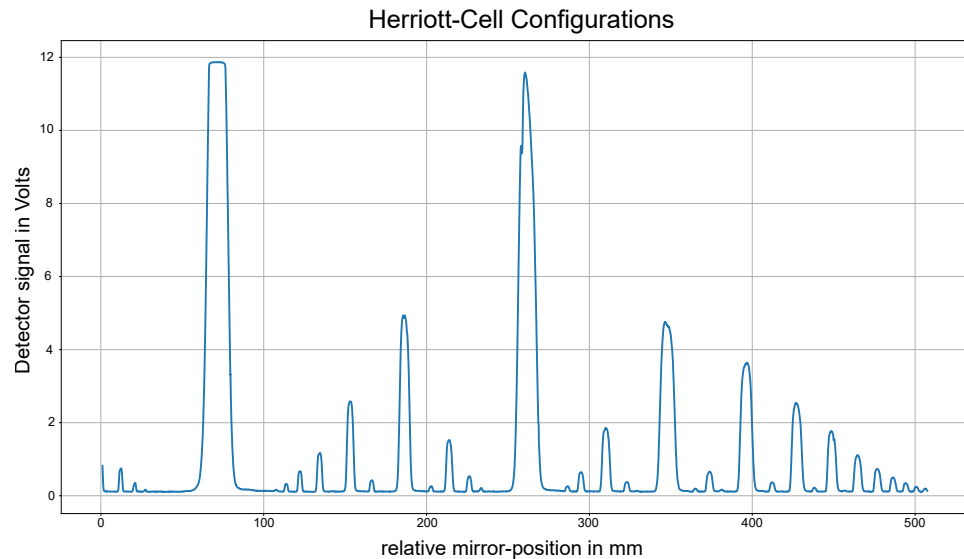


Figure 5.22: Shown are the closed configurations of the Herriott-Cell for a relative change in mirror distance between 0 and 500 mm.

### TDLAS as a total pressure standard

The presented TDLAS was so far only used as a partial pressure standard for Carbon monoxide. It is however possible to use the same experimental setup as a total pressure standard without making any adjustments. This is possible since other gases, e.g. H<sub>2</sub>O, have absorption lines with similar linestrengths ( $10^{-23}$ ) as CO in the same spectral region. If a gas mixture of H<sub>2</sub>O and CO is present, one can determine the partial pressure of the two gasses individually by tuning the QCL to the respective absorption line and then determine the total pressure as a sum of both partial pressure values.

# 6. Refractometry

In addition to the TDLAS setup, another optical pressure standard was designed, built and automated during this thesis, which is based on refractometry. The refractometer is a dual cavity Fabry-Pérot system with several unique features that have been constantly improved during the research period. One distinguishing feature of the system is the dichroic coating of the high-reflectivity cavity mirrors at 1550 and 633 nm, which allow for the investigation of the frequency dependent refractivity of different gases like: Helium, Nitrogen and Argon. After fully characterizing the system, the combined knowledge can be utilized to operate the dual-cavity refractometer as a partial pressure standard for said gasses.

## 6.1 Experimental setup: Refractometer

### 6.1.1 Optics and electronics

The following section is dedicated to list all the required optics and electronics and briefly explain why they are required for the refractivity measurements. Figure 6.1 illustrates the basic operating principle of the dual-cavity Fabry-Pérot refractometer and shows all optical and electronic devices used for the operation. The relevant vacuum components, which are required for the gas-pressure modulation, are discussed in the subsequent section.

Two 633 nm **diode Lasers** (Toptica: DLC-PRO) are used as the main light sources together with a custom built **Iodine-stabilized Helium-Neon Laser**, which serves as a stable, long time absolute-frequency reference. One of the diode Lasers (DLC-PRO I) serves as a short therm, stable frequency reference by phase-locking it to the first Fabry-Pérot Resonator with the help of the Lock-In technique.

For the **Laser-locking**, a commercial FPGA-based digital locking module is used (Toptica: Digilock) (named Lock-In I and Lock In II in Figure 6.1). The input of the module is connected to the detector behind the respective FP-cavity which measures the transmission signal of the resonator. The output of the FPGA is directly connected to the Laser-driver and can modulate the Laser current and therefore the emission frequency of the diode Laser. By slightly demodulating the emission frequency, the FPGA creates an error signal which is equal to the derivative of the Gaussian shaped  $\text{TEM}_{00}$  transmission signal on the detector. The zero crossing of the error signal/derivative is located exactly at the peak position of the  $\text{TEM}_{00}$ -mode and is used as an error-signal-input for the internal FPGA-pid controller. The pid controller then optimized the laser current so that the emission frequency of the Laser is constantly forced to be identical to the transmission peak-position of the  $\text{TEM}_{00}$ -mode of the resonator.

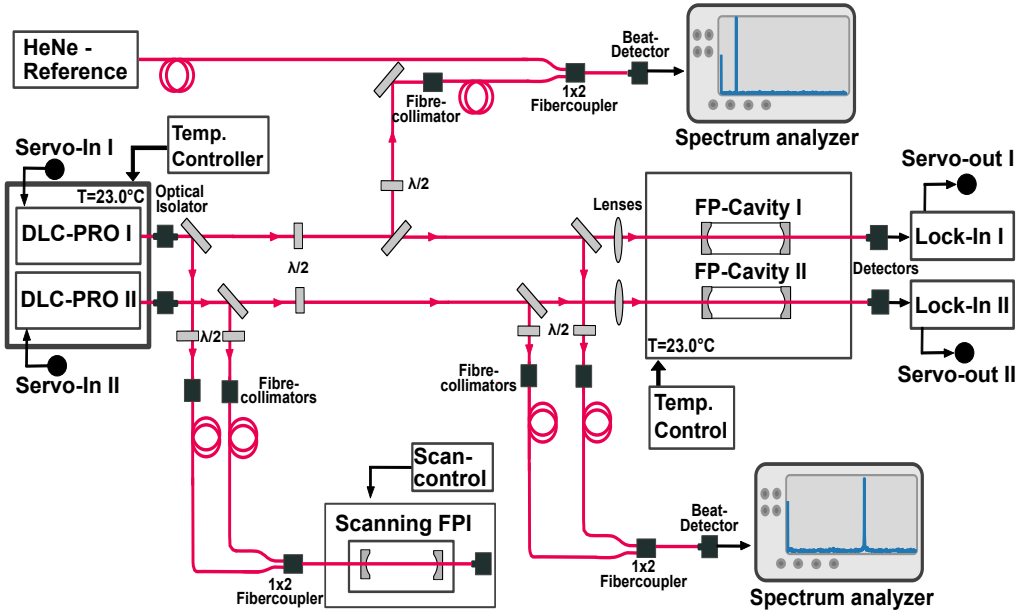


Figure 6.1: Shown is the refractometry-based experimental setup with all relevant optical and electronic devices.

The resonator to which the **reference Laser** (DLC-PRO I) is locked to will be called **reference resonator**. This resonator (FP-Cavity I) is constantly evacuated during all measurements. Locking the reference diode Laser to the evacuated cavity, stabilizes the output frequency of the Laser to the frequency of the respective, chosen  $\text{TEM}_{00}$  of the cavity. This provides a great short therm frequency reference for the measurement Laser (DLC-PRO II), since the reference resonator has a high finesse (1000 to 10000 depending on the resonator used) and is mostly influenced by external temperature fluctuations, which can result in long term drifts of the emission frequency. These short therm drifts can be visualized by measuring the beat between the stabilized HeNe-Laser and the reference Laser. This is achieved by combining the two Lasers with a 2x1 fibre coupler and then measuring the beatsignal between the two with a beat detector and spectrum analyzer.

The **measurement Laser** (DLC-PRO II) is another identical diode Laser, which is phase-locked to the **measurement Fabry-Pérot resonator** (FP-Cavity II). This, second resonator is filled with the measurement gas of choice for refractivity measurements. The refractivity is proportional to the change in beat frequency between the measurement and reference Laser and the beat frequency between the two lasers is observed on a beat detector after combining them with a 2x1 Fiber-coupler before the detector.

The absolute frequency of the HeNe-Laser is known from the theoretical hyper-fine structure of the spectrum and provides a traceable absolute frequency reference for the two diode Lasers via the two simultaneous **beat measurements**. However, the bandwidth of the **beat detector** is limited to 3 GHz, which means that beat signals between the Lasers, that are larger than 3 GHz, can not be detected. Since the two diode Laser have an extensive frequency tuning range it is

## 6.1. EXPERIMENTAL SETUP: REFRACTOMETER

---

required to adjust the Laser current and voltage so that the emission frequencies of the two diode Laser are within a detectable range of: < 3 GHz to the HeNe-Laser. This pre-adjustment of the Lasers is done by using a wavemeter (High-Finesse: WS-5) which is used to measure the emission frequency of the Laser. The Laser current, voltage, grating-angle and temperature are adjusted until the emission frequency of the diode Lasers are aligned with the HeNe reference.

Diode Lasers, especially at 633 nm, are vulnerable to switch abruptly to multi-mode operation. This can occur due to temperature changes or other external effects and results in the diode laser emitting more than one frequency at a time. However, for a refractometer a constant single mode operation is required to preserve the traceability of the laser frequencies and the beat measurements. To ensure that the Lasers are single mode at the chosen Laser configuration of: Laser- temperature, -current and -voltage, a **Scanning Fabry-Pérot** (Thorlabs: SA200-5B) is used. Both, the reference and the measurement Laser are coupled into the same Fabry-Pérot Interferometer (FPI) and the transmission of the FPI is monitored on a detector connected directly to the cavity. If the Laser abruptly switches to multi-mode operation during a measurement, it can be observed on the FPI-detector immediately since additional transmission peaks will become visible in the transmission spectrum.

To avoid external environmental influences, the two diode Lasers are integrated in a **temperature controlled** and vibration resistant enclosure. The enclosure consists of a Styrodur box with an integrated Peltier element which is set to stabilize the internal temperature to 23.0 °C. The FP-Cavities (FP-Cavity I and II) can be integrated into a water-cooled aluminum vacuum chamber, which is connected to a precision calibration bath (CIK: Kambic) with a temperature stability of 1 mk. The vacuum chamber itself is integrated into a multi-layer Sytrodur box, where each Layer contains water-cooled radiators to further stabilize the environmental temperature effects. The radiators are connected to water cooled bath (PolyScience: Mode: AP15R) and operate at 23.0 °C.

As stated earlier, a unique feature is the **dichroic coating** of two of the available resonators. Those allow for simultaneous measurements at 1550 and 633 nm. As a **1550 nm Laser** source two identical fiber Lasers (NKT photonics: Koheras ADJUSTIK X15) were used. They are not shown in Figure 6.1 intentionally, to provide a simplistic overview of the basic operating principle. For measurements however, the two fiber Lasers are spatially overlapped with the diode Lasers and separated again after the measurement and reference resonator respectively. The spatial separation is required to guide the individual lasers onto their respective wavelength-sensitive detectors. The separation is achieved with optical filters that transmit 633 nm and reflect 1550 nm light and two additional 1550 nm detectors for Laser-locking of the fiber-Lasers.

### 6.1.2 Vacuum system

The vacuum system shown in this section is required to supply the measurement cavity with a pure measurement gas, a flexible pressure modulation as well as a traceable pressure reference for the refractivity measurements. Figure 6.2 shows all the vacuum components used to construct the refractometry based pressure standard. The Fabry-Pérot Cavity I is again the reference cavity and the FP-Cavity II the measurement cavity.

The **gas supply** for the measurement cavity is realized with a pure gas bottle of either: Nitrogen, Argon or Helium with the highest possible purity (between 5.0 and 7.0). The measurement gas then has to pass through an additional **sintered metal filter**, which further purifies the gas. A **Mass Flow Controller (MFC)** with an integrated electric valve and a maximum flow rate of 5 sccm (standard cubic centimeter per minute) is used to control the gas flow into the system and the measurement cavity respectively. Before any measurement or after switching gas bottles, the vacuum system up to the Mass flow controller is flushed with the measurement gas several times. This is done by filling the tubing with the respective gas and evacuating it afterwards with the connected oil-free **Scroll pump**. Flushing the system with gas removes potential impurities in the tubing after switching bottles.

For the evacuation of the system an additional set of a **turbomolecular pump** and a scroll pump can be used. All vacuum tubing is made of full metal materials and compatible with ultra-high-vacuum conditions.

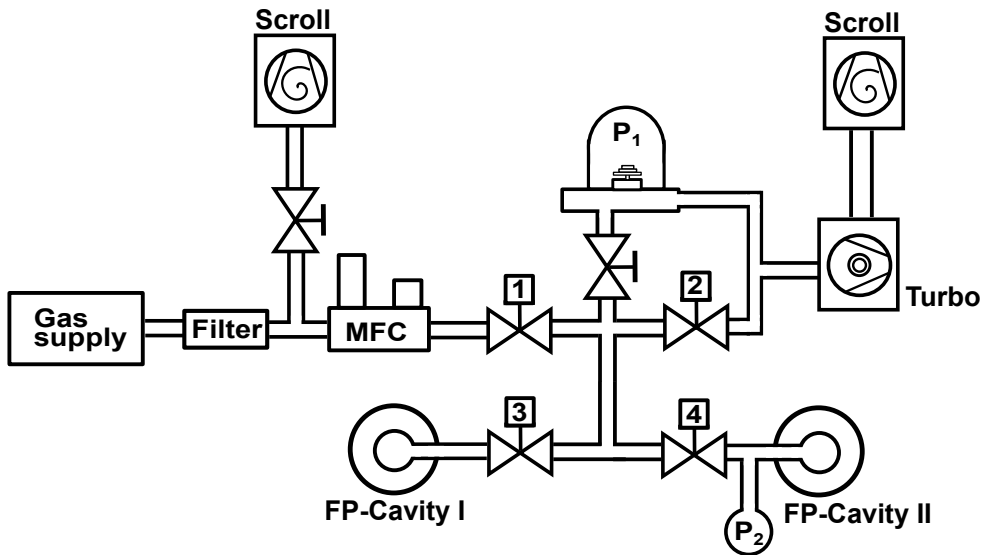


Figure 6.2: Shown are all the required vacuum components used for the optical refractometer.

A set of four **pneumatic valves** are used to control the gas flow through the vacuum system, they are labeled from 1 to 4. With open valves 2 and 3, the reference FP-Cavity-I can be evacuated. Additionally opening valve 4, allows for the simultaneous evacuation of the measurement cavity (FP-Cavity-II).

During a measurement, the gas pressure inside the measurement cavity is modulated by opening valve 1 and setting the Mass-Flow-Controller to the desired gas-flow rate. During a measurement the pneumatic valve to the reference cavity (valve 3) is generally closed, so that the resonator remains constantly evacuated and provides a stable frequency reference. However, valve 2 remains open during a measurement so that one has an equilibrium between gas flow in and out of the system. Depending on how far the needle valve of the MFC is opened one can modulate the total pressure inside the system freely. Pneumatic valves are chosen intentionally, since they do not introduce any heat (though electrical heating) inside of the temperature controlled environment of the two resonators.

To ensure SI-traceable refractivity measurements, several different pressure sensors can be used to assess the gas pressures. A set of three calibrated **resonant silicon gauges** (RSG made by WIKA, labeled as "P2" in Figure 6.2) are directly connected to the measurement chamber and are used to assess the total pressure within the measurement resonator. Additionally a calibrated **piston gauge** (labeled as "P1") can be utilized for setting the pressure in the system and performing directly traceable refractivity measurements.

## 6.2 Resonator choice

The heart of every Fabry Pérot based refractometer is the resonator, which is to be filled with measurement gas of choice. Generally speaking each resonator, used for FP-based refractometry, consists of a spacer material with a fixed length  $l$  and a pair of mirrors which are contacted to the planar end surfaces of the spacer material. The choice of spacer material has a significant influence on the performance of the system and how the cavity reacts to environmental influences like temperature fluctuations or gas modulation. Often times, glass materials like: Zerodur, Ultra-low-expansion(ULE)-glass or Clearceram are used. They have the benefit of being polishable and allow for direct optical contact bonding of the mirror substrate with the spacer material, which does not require glues or binders. In many cases the mirror substrate can be fabricated from the same material as the spacer to create a solid bond between spacer and mirror after optical contacting. The three listed spacer materials also have the benefit of having a zero-crossing of the thermal expansion coefficient ( $\alpha$ ) close to room temperature, which is the most common operating temperature in optical laboratories. In the case of Zerodur the thermal expansion coefficient is as low as :  $10^{-6}/K$ . Since the thermal expansion determines how much the size of the material changes due to temperature changes:

$$\frac{\Delta L}{L_0} = \alpha \Delta T \quad (6.1)$$

it becomes an important property when designing length sensitive Fabry Pérot refractometers. One disadvantage glass materials is their relatively high out gassing rate for Helium, which is a common calibration gas. Especially ULE-glass is known for taking up Helium rapidly when it is exposed to a Helium atmosphere and then slowly releasing the gas over time again. This characteristic of ULE (and other glasses), can result in unwanted long term drifts of the overall resonator length and require constant re-alibration.

An alternative to glass materials are metals, like stainless steel or Invar (a nickel iron alloy). These spacer materials typically have very low out gassing rates, which is one reason why they are commonly used for other vacuum applications. The trade off with stainless steel or Invar spacers is however, that the mirrors cannot be optically contacted or glued to the spacer material directly. Instead they have to be mechanically pressed against the spacer and secured in place. Due to the high mechanical forces required to create a leak tight seal between the metal spacer and the mirrors, it is not uncommon to damage the mirror substrates during the process.

Figure 6.3 shows three different resonators used by the National Metrology Institutes participating in the QuantumPascal project. A variety of different spacer materials, mirror substrates and cavity designs have been tested during the project period.

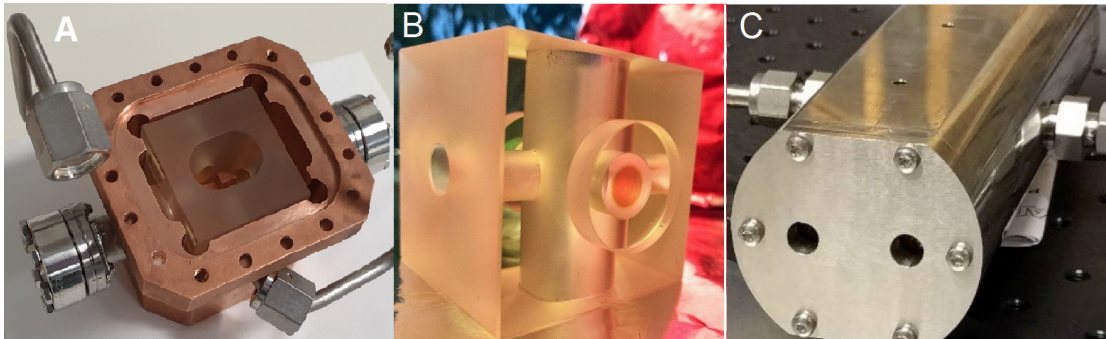


Figure 6.3: A and B: Zerodur resonator used at the LNE-CNAM in france. A) shows the copper enclosure used for thermal stabilization of the Zerodur cavity. C) Invar based Fabry Pérot cavity design used by the PTB and the Umea university in sweden.

Within this thesis, glass based spacer materials were investigated for their out gassing behavior with the intent to characterize potential long term drifts and design guides for optimal resonator design with regards to FP- based refractometry. For refractivity measurements, an initial Zerodur based dual cavity system was used and later upgraded to an invar based resonator with a dichroic set of mirrors.

### 6.2.1 Measurement of the coefficient of thermal expansion (CTE)

The coefficient of thermal expansion (CTE) is a material property that is especially relevant when working with FP-based refractometers. The CTE of the spacer material of the resonator determines how sensitive the system is to temperature fluctuations and what quality of a thermal insulation is required to reach the target uncertainty of the refractometer. The temperature induced length change of the spacer material:

$$\frac{\Delta L}{L_0} = \alpha(T)\Delta T \approx \frac{\Delta f}{f_0} \quad (6.2)$$

depends on the coefficient of thermal expansion,  $\alpha$  and the temperature change  $\Delta T$ . The CTE is a temperature dependent property but can be approximated as a constant value for a small temperature range if one wants to approximate the order of magnitude with an experimental approach. The change in cavity lengths can, in the case of a FP-based refractometer, be assessed with a beat measurement between the measurement- and a reference-Laser.

The CTE of the Invar based single cavity resonator was experimentally approximated with the setup shown in section 6.1.1. The Zerodur resonator was used as a reference resonator and the Invar cavity was utilized for the CTE measurements. However, both resonators were constantly evacuated during the complete measurement campaign to eliminate pressure induced fluctuations of the beat signal.

To determine the CTE of Invar, the beat between the locked reference and measurement Laser were detected over time, while the temperature of the measurement cavity was modulated. The beat between the two laser fields is assessed with a beat detector and a spectrum analyzer, that can track any changes in beat frequency. Both, the reference and the measurement Laser are locked to the first  $\text{TEM}_{00}$ -mode of their respective resonators with a digital, FPGA based locking module using the LOCK-IN technique. The measurement resonator is positioned inside of multi-layer, thermally insulated box where the temperature is stabilized using a calibration water bath in combination with multiple water cooled radiators. The reference resonator was positioned in an outer layer of the thermally insulated box, so that a constant operating temperature and passive shielding from room temperature fluctuations could be ensured.

The temperature induced change in beat signal is proportional to the CTE as long as the system is free of other environmental influences like pressure modulations (which is guaranteed due to evacuation of the system). To introduce a temperature increase of the system, the measurement resonator temperature was modulated by programming the calibration bath to increase and decrease the bath temperature periodically. The starting temperature was chosen to be XX, so that it is similar to room temperature and was then step wise increased by 0.2 K and decreased again to the starting temperature. After increasing the temperature by 0.2 K, the system was given several hours time to stabilize its temperature before another step wise increase had been initiated. Figure ?? shows the periodic modulation of the measurement-resonators temperature, which was induced by modulating the calibration baths temperature. One can also see the temperature of the reference resonator, which is indirectly modulated, although it is thermally and spatially shielded from the water cooled radiators (but not sufficiently). This results in a periodic and unwanted modulation of the reference Laser frequency, that will later be discussed in greater detail.

During the temperature modulation process, the beat signal was detected and Figure ?? shows the beat signal between the two Laser fields for the same time period during which the temperature of the measurement resonator was modulated. The beat shows a similar modulation as the temperature measurement but is distorted by the indirect modulation of the reference resonator temperature due to insufficient thermal shielding. The beat signal is therefore not directly proportional to the initiated temperature modulation, since the reference frequency is also periodically changed.

Assuming that the CTE is constant for the small temperature range observed, one can approximate  $\alpha$  as constant and extract it from the beat measurement. Therefore, the change in beat frequency, due to the temperature increase of 0.2 K, was extracted from Figure ?? for each step of the periodic temperature modulation. The obtained values for  $\Delta f$  where then averaged and the standard deviation was calculated to:

$$\Delta f^{T \rightarrow T \pm 0.2K} = 86.5 \text{ MHz} \pm 10 \text{ MHz} \quad (6.3)$$

The large standard deviation is due to the unwanted temperature modulation of the reference resonator and therefore the reference Laser frequency. The approximated CTE of Invar can then

be calculated using equation 6.2 :

$$\alpha = \frac{86.5 \text{ MHz}}{200 \text{ THz} \cdot 0.2 \text{ K}} = 2.1 \cdot 10^{-6}/\text{K} \quad (6.4)$$

where  $f_0 = 200 \text{ THz}$  is the operating frequency of the utilized 1550 nm Lasers.

One can now simulate the change in beat frequency due to the "constant" CTE of the Invar and subtract it from the measurement data in Figure ?? to investigate the measurement residuals. Figure ?? shows the raw data after subtracting the temperature induced change of the frequency of the measurement Laser from the measurement. What remains is the change in beat signal that was introduced by the unwanted frequency modulation of the reference Laser due to insufficient temperature shielding/ stabilization of the reference resonator. By comparing the measurement residuals with the temperature of the reference Laser (shown in Figure ??) one can observe that both signals have the same periodicity.

### 6.3 GAMOR method

The Gas modulation refractometry (GAMOR) method is a gas refractivity measurement technique, developed and popularized by the swedish metrology research groups from the RISE (Research Institute of Sweden) and the Umea university [2].

For Fabry-Pérot based measurement techniques of the refractivity, the measurement gas is introduced into the cavity, which results in a shift of the resonator mode frequencies. If a (measurement) Laser is phase-locked to one of the resonator modes, this shift can be converted to a shift in Laser frequency. By comparing the frequency of the measurement Laser with the frequency of a second (reference) Laser that is phase-locked to an evacuated reference Fabry-Pérot Cavity, one can detect a change in beat frequency between the two Lasers. The change in refractivity can thereby be directly linked down to a simple beat measurement on a photodetector that combines the two Laser fields.

For a Laser that is locked to a cavity mode of a fully evacuated resonator, its unmodified frequency  $\nu_m^{(0)}$  is given as:

$$\nu_m^{(0)} = \frac{q_m^{(0)} c}{2L_m^{(0)}} \quad (6.5)$$

where  $q_m^{(0)}$  is the longitudinal resonator mode with mode number  $m$  and  $L_m^{(0)}$  the empty resonator length. If gas is let into the resonator additional effects that modify the mode frequency and cavity length have to be accounted for and the gas filled resonator mode frequency  $\nu_m^{(g)}$  is given as:

$$\nu_m^{(g)} = \frac{\left(q_m^{(0)} + \Delta q_m^{0 \rightarrow g}\right)c}{2n_g \left(L_m^{(0)} + \delta L_m^{0 \rightarrow g}\right)} = \nu_m^{(0)} \left(\frac{1 + \frac{\Delta q_m^{0 \rightarrow g}}{q_m^{(0)}}}{n_g \left(1 + \frac{\delta L_m^{0 \rightarrow g}}{L_m^{(0)}}\right)}\right) = \nu_m^{(0)} \left(\frac{1 + \Delta \bar{q}_m^{0 \rightarrow g}}{n_g \left(1 + \delta \bar{L}_m^{0 \rightarrow g}\right)}\right) \quad (6.6)$$

where  $n_g$  is the refractive index of the measurement gas,  $\delta L^{0 \rightarrow g}$  is the change in cavity lengths by pressure induced deformation and  $\Delta q^{0 \rightarrow g}$  accounts for mode jumps during the introduction of gas into the cavity. In the last step the equation was simplified by introducing relative mode-

and lengths-change variables:  $\Delta\bar{q}_m^{0 \rightarrow g}$  and  $\delta\bar{L}_m^{0 \rightarrow g}$ .

For a beat measurement between the measurement Laser with the frequency:  $\nu_m^{(g)}$  and the reference Laser with the frequency:

$$\nu_r^{(0)} = \frac{q_r^{(0)} c}{2L_r^{(0)}} \quad (6.7)$$

the two Laser fields are spatially overlapped and a RF signal, between 0 and 4 GHz, can detected on a photodetector. The respective beat signal:  $f_{(0,g)}$  for an evacuated reference cavity and a gas filled measurement cavity, then becomes:

$$f_{(0,g)} = \nu_r^{(0)} - \nu_m^{(g)} = \nu_r^{(0)} - \nu_m^{(0)} \left( \frac{1 + \Delta\bar{q}_m^{0 \rightarrow g}}{n_g (1 + \delta\bar{L}_m^{0 \rightarrow g})} \right) \quad (6.8)$$

Although the basic operating principle of a FP-based refractometer seems simple initially, in praxis it comes with many experimental challenges. One mayor challenge are system drifts of various kinds, that influence the Fabry-Pérot cavity over the measurement period or longer time scales. These drifts usually alternate the lengths of the cavity through different physical effects like: temperature fluctuations, out gassing of the cavity spacer materials or gas leaks in the vacuum system. A change in cavity lengths or increasing gas impurities result in a change of resonator mode frequency, that is not related to a change of measurement gas refractivity.

The GAMOR methodology is able to eliminate linear drifts by periodically measuring the gas refractivity at a given pressure  $P$  with a follow up measurement of the base line at a pressure  $P \approx 0$ , at an evacuated state of the measurement resonator. Constantly tracking the baseline drift of the resonator allows for a simple correction by interpolating the zero measurements. Since the drifts are linear, on a short time scale, one can use the interpolated correction of the baseline to also correct the actual refractivity measurements that were carried out in between the baseline measurements.

Figure 6.4 shows an example of two consecutive GAMOR cycles, were the measured beat signal between a 1550 nm, phase locked reference- and measurement-Laser is plotted against time. Each GAMOR cycle starts and ends with a baseline measurement to track baseline drifts, which in this case are introduced by temperature fluctuations of the system, as can be seen in the respective resonator-temperature profile at the bottom of Figure 6.4. The temperature was observed during the beat measurements with an SPRT that was integrated into the measurement cavity. After the zero measurements, several refractivity measurements were performed at different pressures, by introducing or removing Nitrogen gas into the measurement resonator through an automated needle valve. The modulation of the gas pressure inside the measurement resonator results in the expected shift in the beat signal between the reference- and measurement-Laser.

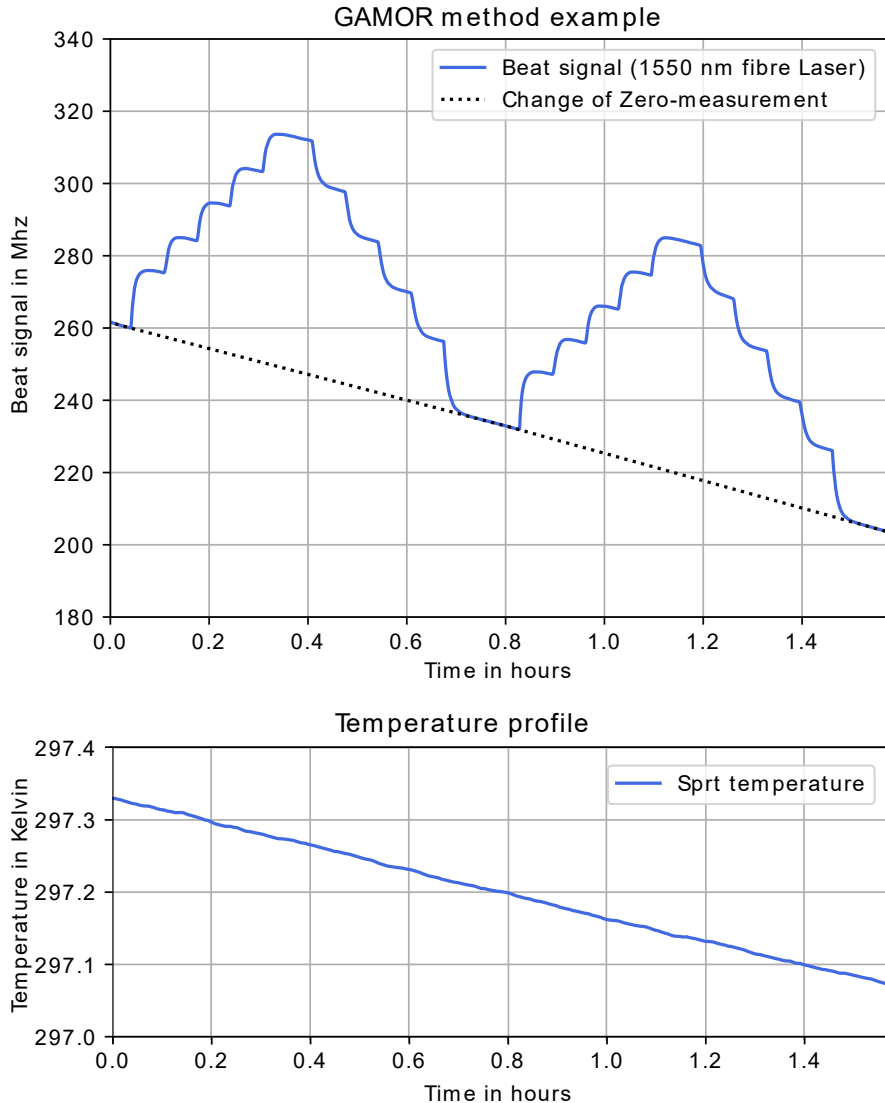


Figure 6.4: **Top:** Exemplaric GAMOR cycle with a baseline drift of the beat signal, due to temperature fluctuations inside the measurement resonator. **Bottom:** Temperature change within the measurement resonator during the measurement time period.

The interpolated baseline drift can then be used to correct the beat signal for drifts, in this case introduced by cooling down the measurement resonator by 0.2 K over a time period of 90 minutes. Figure 6.5 shows a comparison between the corrected beat-signal-measurement and a pressure measurement that was performed simultaneously with a group standard of three calibrated resonant silicon gauges. The modulation of the Nitrogen pressure inside the resonator directly results in a change in gas refractivity that can be detected with the refractometer and both, the beat signal and cavity gas pressure are proportional to each other.

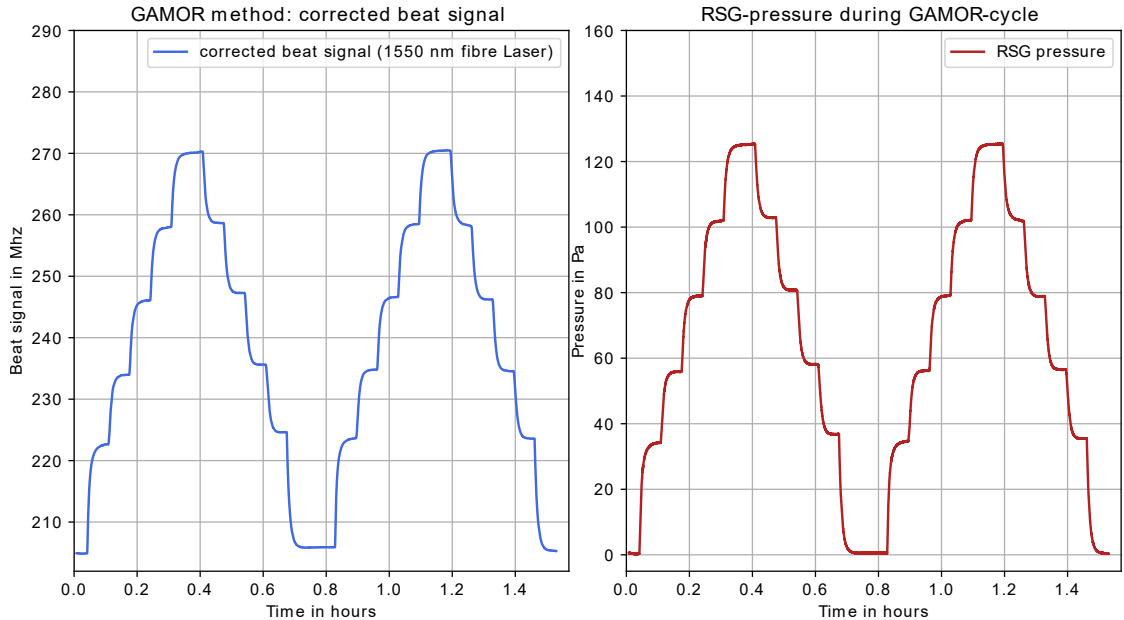


Figure 6.5: **Left:** Corrected beat signal during a measurement cycle. **Right:** Measurement of the Nitrogen pressure inside the measurement-resonator.

## 6.4 Free-Spectral-Range of the Invar resonator

The free-spectral-range (FSR) of a resonator is an important property that can be determined experimentally with different approaches. It is defined as:

$$\Delta\nu = \frac{c}{2nL} \quad (6.9)$$

where  $\Delta\nu$  is the frequency difference between two consecutive  $\text{TEM}_{00}$  modes of the cavity,  $L$  is the length of the resonator and  $n$  is the refractive index of the investigated gas.

With respect to FP-based refractometry, precise knowledge of the FSR is required to determine the change in beat frequency during a refractivity measurement. When filling the measurement resonator of a dual Fabry Pérot cavity with gas, the beat frequency between the detected reference- and measurement-Laser fields is given by:

$$f_{0,g} = \nu_r^0 - \nu_m^g = \nu_r^0 - \nu_m^0 \left( \frac{1 + \Delta q_m^{0 \rightarrow g}}{n_g(1 + \delta L^{0 \rightarrow g})} \right) \quad (6.10)$$

as it was shown in the previous section. Whenever the relative mode number  $\Delta q_m^{0 \rightarrow g}$  changes by one, due to the introduction of gas into the system, the beat frequency changes by the exact value of the FSR of the measurement resonator. It is possible to determine the FSR of any resonator by measuring its length or by directly determining the frequency difference between two consecutive  $\text{TEM}_{00}$ -modes of the cavity. Both methods are valid but generally frequency measurements can be carried out with greater precision and are therefore often times preferred.

To determine the FSR, the 1550 nm measurement Laser is phase locked to the first  $\text{TEM}_{00}$ - mode

of the measurement resonator, same as the reference Laser with its respective cavity. An initial beat measurement is carried out between the two Laser fields, while both cavities are positioned in the same temperature controlled environment. The lock of the measurement laser is then released from the first  $\text{TEM}_{00}$ -mode and is instead locked to the next adjacent  $\text{TEM}_{00}$ -mode. This can be achieved by adjusting the operating-voltage, -current or -temperature of the measurement Laser, so that its emission frequency is closer to the frequency of the second  $\text{TEM}_{00}$ -mode of the resonator. The lock can then be re-engaged and the Laser emission frequency is stabilized to the respective frequency of the adjacent resonator mode.

The lock of the reference Laser remains unchanged and a second beat measurement between the two Laser fields is performed. For stable environmental conditions, the detected change in beat frequency between the two system configuration is equal to the FSR of the measurement resonator. Figure 6.6 shows the beat measurement between the two laser fields of the 1550 nm Laser systems before and after changing the lock of the measurement cavity mode by  $\Delta q_m^{0 \rightarrow 1}$ .

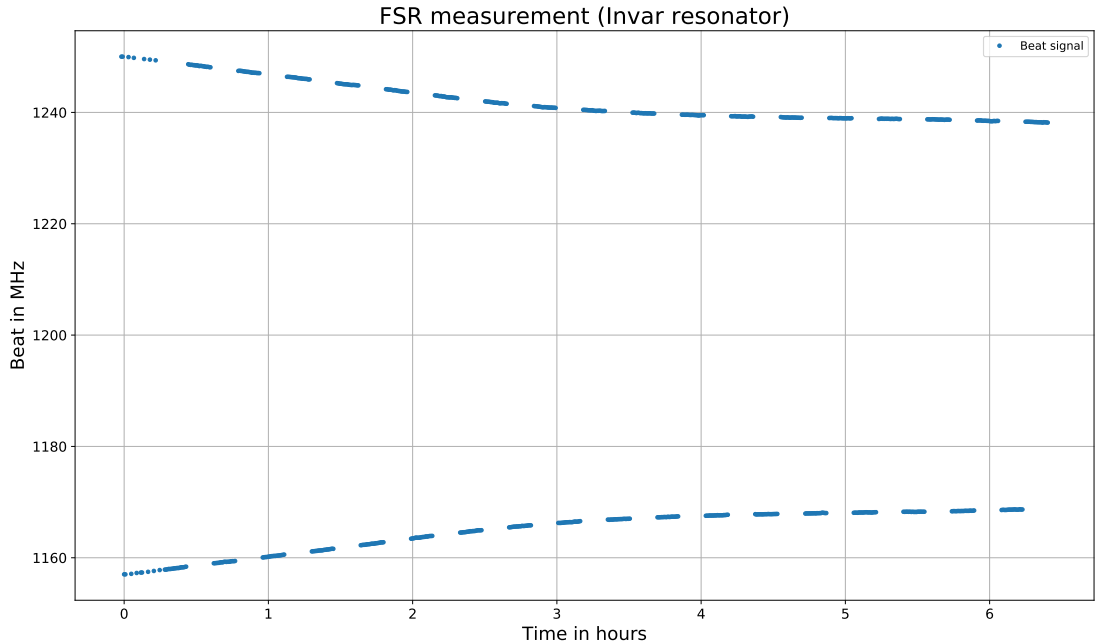


Figure 6.6: .

To improve the measurement uncertainty of the FSR, the described lock and re-lock of the measurement Laser was repeated several times. The beat signal for each system configuration, was measured for ten minutes and the signal was then averaged over time to account for eventual temperature instabilities during the ten minute period. Two consecutive measurements can then be compared to each other to determine the FSR of the resonator. The beat signal, where both Laser are locked to their respective first  $\text{TEM}_{00}$ - modes, are around 1.24 GHz. While the beat signal measurement of the second configuration yields around 1.16 GHz.

By adjusting the measurement Lasers operating Voltage, to lock it to the second  $\text{TEM}_{00}$ , the beat signal reaches zero and increases again (up to a value of 1.16 GHz). Resulting in an initial estimated FSR value of: 2.4 GHz. Since the beat signal "crossed" zero both configurations

react anti proportional to the temperature fluctuations during the measurement. Fluctuations of the temperature where measured with an SPRT and could be corrected for. Within the raw measurement data, in Figure 6.6, they are visible as an overall trend that results in a slow change of the detected beat frequency, which is in the order of 1.5 MHz per hour.

The results of the individual FSR-measurements were then averaged again and the FSR of the measurement cavity could be determined as:

$$\Delta\nu_{meas} = 2.407 \text{ GHz} \pm xxxx \quad (6.11)$$

## 6.5 Temperature and pressure assessment

FP-based refractometers are highly sensitive to temperature fluctuations of the gas, which potentially allows them to be used as thermometers as well, if the respective gas pressure is known instead. The temperature stability requirements during a gas density measurement are therefore high and often times require a multi layered temperature stabilization of the system. During this thesis the refractometer could be integrated into a water cooled, aluminum based vacuum chamber which was connected to a calibration bath with a temperature stability of 1 mk (CIK: Kambic). The vacuum chamber was integrated into a multilayered, temperature controlled enclosure made of Styrodur. Radiators, that are connected to the same calibration bath are used to control the air temperature of the enclosure to the same value as the vacuum chamber.

During a refractometry measurement, the gas temperature is assessed with two 25 Ohm standard platinum resistance thermometers (SPRT) which are connected to a measurement bridge (Isotech:MircoK 70) and a reference resistor. Depending on the resonator used, the SPRTs are either directly integrated into the Cavity itself (inserted into a drilled bore) or in direct contact with the cavity. Over a period of 2 years, the SPRTs were calibrated three times against the water triple point and the Gallium melting point in the temperature laboratory of the PTB. During the calibration, the same measurement bridge was used, which compensates for the self heating of the SPRT-sensors which require an operating current of 1 mA. The resistance of the SPRT is assessed with a four wire measurement and then internally compared to the reference resistor. The reference resistor itself is integrated into a temperature controlled box which operates at 23 °C. With the help of the calibration certificate the measured resistances of the SPRTs can then be converted into temperatures. Figure 6.7 shows the stability of the calibration bath that is used for thermostatisation of the resonator and experimental enclosure. The temperature was assessed with the two SPRTs over a time period of 140 hours.

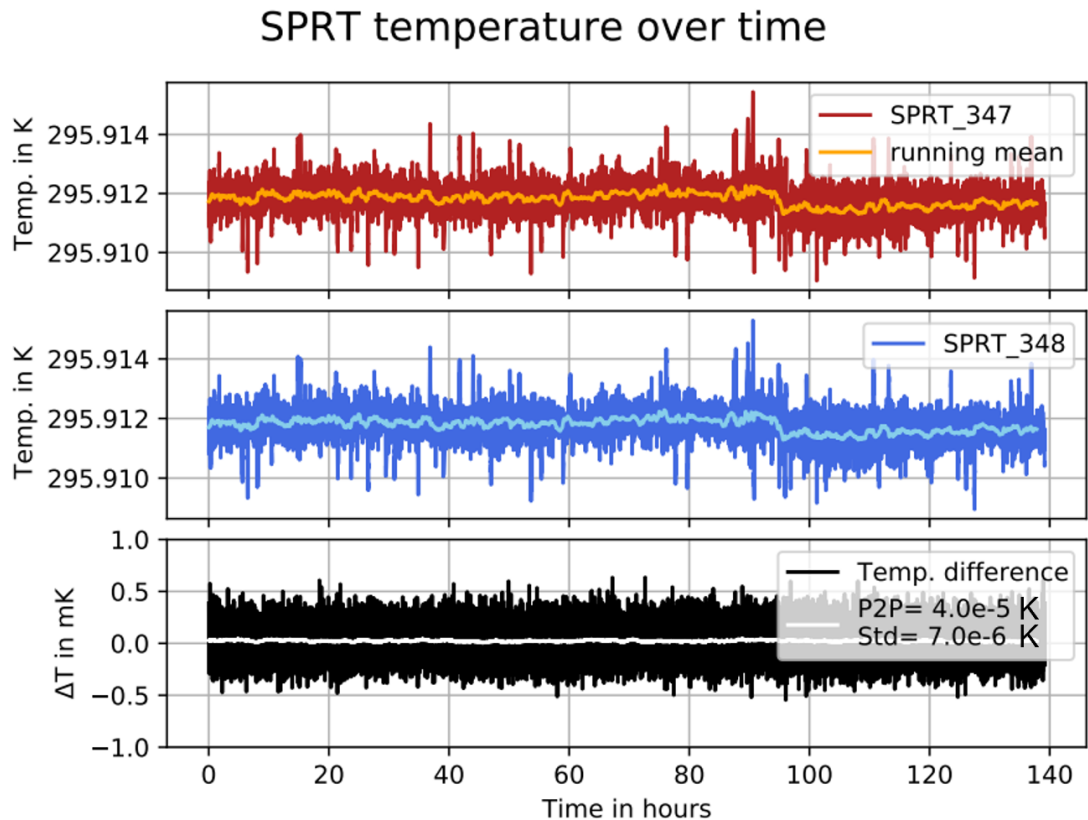


Figure 6.7: Temperature stability of the calibration bath assessed with two calibrated SPRTs labeled: 347 and 348. Shown is the respective measurement data together with a running mean over 100 seconds. At the bottom, the temperature difference  $\Delta T$  between the two sensors is shown. For the running mean it is in the order of  $4 \cdot 10^{-5} \text{ K}$  with a standard deviation of  $7 \cdot 10^{-6} \text{ K}$ .

If a gas **pressure** assessment was required for a refractivity measurement, a group standard of three identical resonant silicon gauges (RSG) could be used for pressure ranges from 1 Pa to 100 kPa. Over the course of this thesis the sensors were calibrated three times against the static expansion system 3 of the vacuum metrology working group at the PTB. Alternatively, two calibrated piston gauges could be used to set the measurement pressure in the cavities between 1 kPa and 100 kPa.

## 6.6 Refractivities of Helium, Nitrogen and Argon

The refractivity of a gas is not only pressure dependent, which allows for the design and construction of FP-based pressure standards, but it is also frequency dependent. A Fabry-Pérot cavity with dichroic mirrors can therefore be used to investigate the frequency dependence of the refractivity by performing the same refractivity measurements simultaneously at two (or more) Laser wavelengths e.g 633 and 1550 nm.

During this thesis, the refractivities of the three gases: Helium, Argon and Nitrogen were investigated.

**Helium** is chosen as a calibration gas for the refractivity measurements since it is one of the few gases where precise calculations of gas parameters, like the refractivity and density virials, can be carried out in a reasonable time frame. This is due to its molecular properties as a noble gas and low number of atoms involved. **Nitrogen** is chosen since almost all industrial pressure sensors are calibrated with Nitrogen gas at national metrology institutes and it is one of the most abundantly available gases. Theoretical calculations for gas parameters of **Argon** are more challenging but comparisons with experimental research can improve the overall understanding and future calculations. Argon is therefore chosen as a third gas.

To investigate and measure the refractivity of the three aforementioned gases, the dual cavity Fabry-Pérot system was used (see Figure 6.1 of the experimental setup section)s. The dichroic **Invar resonator** was chosen as a measurement resonator, while the Zerodur cavity was used as a reference. Two sets of two Lasers were used to investigate the frequency dependence of the individual gas refractivities, where one **set of Lasers** operates at 633 nm and the other one at 1550 nm. Experimentally, the two measurement Lasers were spatially overlapped and separated using selective optical filters. The filters are reflective for 633 nm and transmit 1550 nm laser light. Both wavelengths were then sent through the Invar resonator and locked to a TEM<sub>00</sub>-mode of the cavity. The beat signals to their individual reference Lasers, at 633 and 1550 nm respectively, was detected with two sets of beat detectors. Any change in beat frequency was visualized and tracked with a spectrum analyzer. The pressure in the measurement resonator was controlled using a fully automatic needle valve. If the pressure is modulated adequately, one can count the TEM<sub>00</sub>-modes and obtain the required change in modenumber  $\Delta q^{P_1 \rightarrow P_2}$  in between measurements at the arbitrary set pressures  $P_1$  and  $P_2$ .

At all points during the measurement, the reference cavity was fully evacuated using a turbomolecular pump. The pressure in the measurement cavity was modulated using the GAMOR methodology and tracked with a set of three, calibrated resonant silicon gauges. The gas pressure in the resonator was step wise modulated between 0.1 and 360 Pa. To avoid cross contamination and preserve the respective gas purity, measurements with different gases were carried out successively. In between measurements the **vacuum system** was fully evacuated and flushed several times with the new measurement gas to get rid of potential residual gases in the vacuum system and resonator.

The obtained change in beat frequency  $\frac{\Delta\nu}{\nu_0}$  can then be used to determine the gas refractivity for the given pressure range via:

$$(n - 1) = \frac{\frac{\Delta\nu}{\nu_0} + \frac{\Delta_q}{q_0}}{1 - \frac{\Delta\nu}{\nu_0} + \epsilon_m} \quad (6.12)$$

where  $\epsilon_m$  is a deformation coefficient, the calculation of which is explained in more detail in the following chapter. Figure 6.8 illustrates the experimental results for all three gases and the two chosen Laser wavelengths.

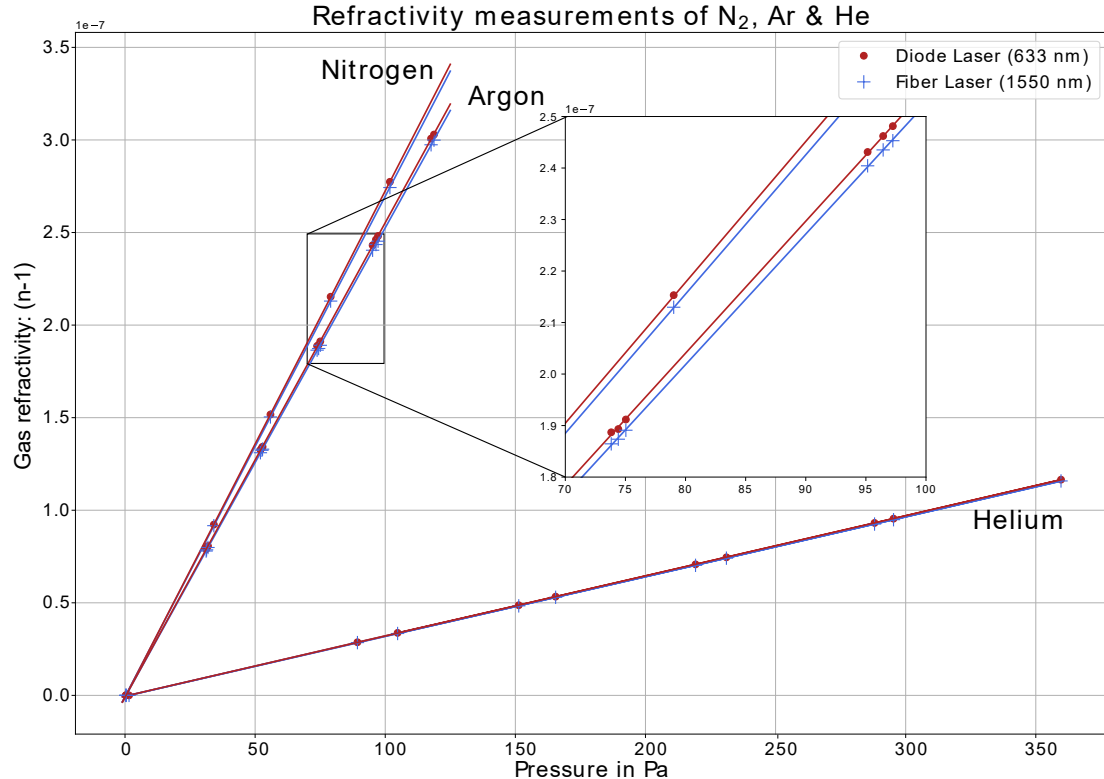


Figure 6.8: Shown are the combined refractivity measurements for Helium, Argon and Nitrogen for a pressure range between 1 and 350 Pa. Measurements were performed simultaneously at two different wavelengths (633 and 1550 nm).

The measurement effect for Helium is around 8 times smaller than that of Nitrogen and 7.1-times smaller than that of Argon. One can also observe the clear frequency dependence of the refractivity in the zoomed-in section of Figure 6.8. The measured refractivity, at identical pressures but different Laser wavelengths, is always smaller for greater wavelengths. At 1 Pa, the fractions  $\delta(n - 1) = \frac{(n-1)_{1550 \text{ nm}}}{(n-1)_{633 \text{ nm}}}$  are given as:

Gas :	Helium:	Argon:	Nitrogen
$\frac{(n-1)_{1550 \text{ nm}}}{(n-1)_{633 \text{ nm}}}$ :	0.994	0.989	0.988

Table 6.1: Frequency dependence of the refractivity

The measured refractivity can now be used to determine the gas density, if the one wants to utilize the refractometer as a pressure standard. By using the theoretical values for the refractivity

virials: A and B, together with the density virial  $B_\rho$  as shown in the theory part of this thesis:

$$\rho = \frac{2(n-1)}{3A} \cdot \left( 1 - \frac{1+4B}{A^2}(n-1) \right) \quad (6.13)$$

$$P = RT\rho(1 + \rho B_\rho) \quad (6.14)$$

It is however required to further analyze the system with respect to its pressure dependent deformation before it can be utilized as a pressure standard. The deformation results in a pressure dependent lengths change of the cavity that results in an additional measurement effect.

## 6.7 Pressure induced cavity deformation

Within the QuantumPascal project, many pressure standards are developed at the individual National metrology institutes (NMIs) of which many utilize external cavities. The resonators are either integrated directly into the measurement unit (e.g in the case of a refractometer or for cavity ring down spectroscopy) or function as a frequency reference for the Pound-Drever-Hall or Lock-In technique. A simple Fabry-Perot resonator consists of a spacer material and two mirrors, which are attached to the end surfaces of the spacer substrate. The spacer ensures a constant distance between the mirrors and prevents them from tilting. The distance between the mirrors defines the standing wave that is formed inside the resonator and has to be well known for accurate measurements of the refractivity. The distance between the mirrors can deviate significantly due to environmental influences such as temperature changes or mechanical deformations due to pressure. This cavity deformation can be accessed with finite element simulations, using commercial programs like COMSOL or ANSYS, for a given set of spacer and mirror materials.

### 6.7.1 Deformation of a specific cavity with COMSOL

As preparatory work to simulating the deformation of a cavity used for CRDS, the pressure dependent deformation of a Fabry-Perot resonator, designed by the LNE-Cnam (Laboratoire commun de métrologie), was investigated with the commercial program COMSOL. The examined resonator consists of a 100 mm long Zerodur spacer to which two fused-silica mirrors, with a diameter of 50 mm and a thickness of 15 mm, were optically contacted. The spacer material itself has an inner diameter of 34 mm and an outer diameter of 54 mm. The material properties of Zerodur and fused silica, which are needed to determine the mechanical deformation of the mirrors, are listed in table 6.2. Figure 6.9 (a and b) show a 3D-model of the resonator and its symmetry planes.

Material:	Zerodur	Fused Silica
Density (kg/m <sup>3</sup> ):	2530	2195
Poisson number:	0.240	0.155
Thermal conductivity (W/ m K):	1.46	1.25
Youngs modulus (GPa):	90.3	73.0
Thermal expansion coef. (1/ K):	$2.00 \cdot 10^{-8}$	$5.55 \cdot 10^{-7}$

Table 6.2: Material properties of Zerodur and fused silica.

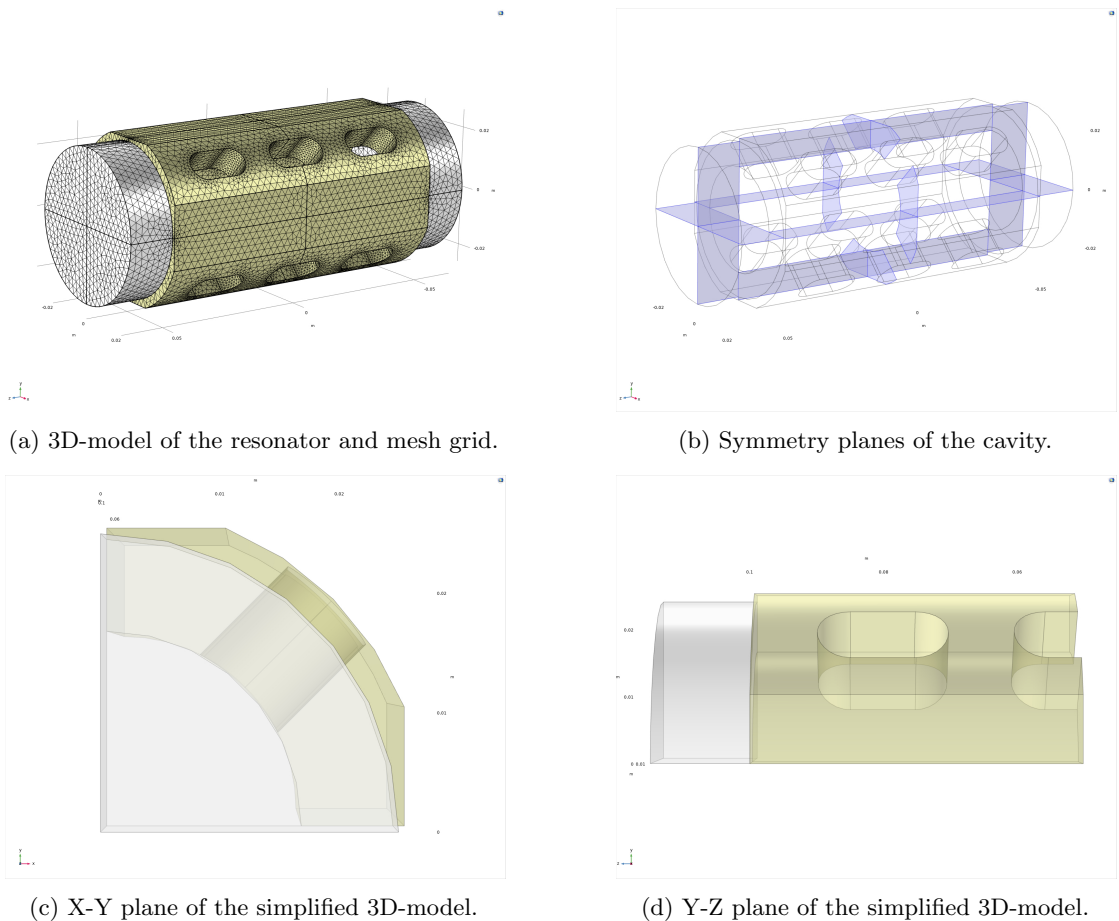


Figure 6.9: Shown is the complete 3D-model of the simulated resonator (a), the three symmetry planes of the object (b), aswell as the simplified 3D-model which was used to minimize computation time (c and d).

The 3D object was created within COMSOL using the linear elastic model and assuming that both materials are joined together, forming one solid object without a junction area. The 3D-model of the cavity is divided into small mesh elements with a user defined size. Depending on the size of these mesh elements, the simulation accuracy and computation time can be enhanced or decreased. For the first iteration of the simulation a minimal element size of  $1.3 \cdot 10^{-3}\text{m}$  and a maximum element size of  $1.3 \cdot 10^{-5}\text{m}$  were defined. In this configuration the resonator was separated into a total number of 190.000 mesh elements. It is possible to reduce the required computation time further by utilizing the symmetry planes of the resonator. Since the cavity is symmetric around three planes, it is sufficient to simulate only 1/8th of the object (see Figure 6.9 (c and d)) without losing any information.

After the modeling process is complete one can apply a fixed force per area to all external surfaces of the resonator in order to estimate the pressure induced deformation with the finite element simulation. In the case of a refractometer the deformation of the mirrors along the z-axis (optical axis) is most important. Fig.6.10 shows a displacement map of the spacer and mirror surfaces after a pressure of 1 Pa was applied to the system. The displacement of the materials increases quadratically from the center point of the mirror to the edges for the given pressure value. The absolute deformation of the mirror center is in the order of  $-3 \cdot 10^{-13}\text{m}$ . The relative length change of the complete resonator:  $\frac{\delta L}{L}$  can be calculated and was determined to be:  $-6.39 \cdot 10^{-12}$ .

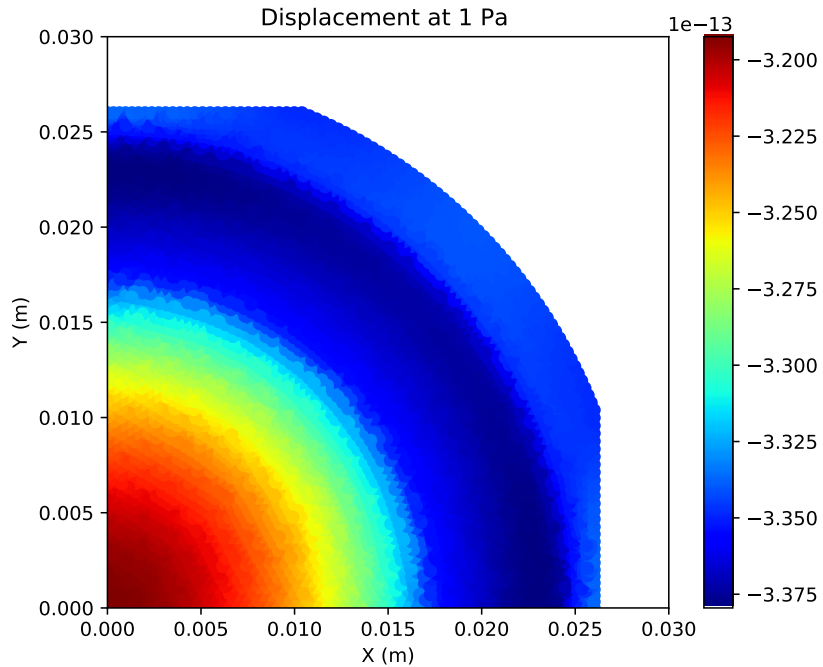


Figure 6.10: Shown is the displacement of the X-Y-Plane in the direction of the optical pathway (z-axis). The surface includes the mirror and the spacer materials.

To determine the pressure dependent deformation, the simulation was repeated several times for additional pressure values in the range of 1 Pa to 1 kPa. As a reference point the center of the mirrors was chosen. The relative displacement of the center points is then plotted against the simulated pressure value (see Figure6.11). A linear correlation between the simulated pressure and the relative deformation can be observed and the corresponding fit function was determined to be:

$$f(x) = (-6.39 \cdot 10^{-12} \pm 3.9 \cdot 10^{-22}) \cdot x \quad (6.15)$$

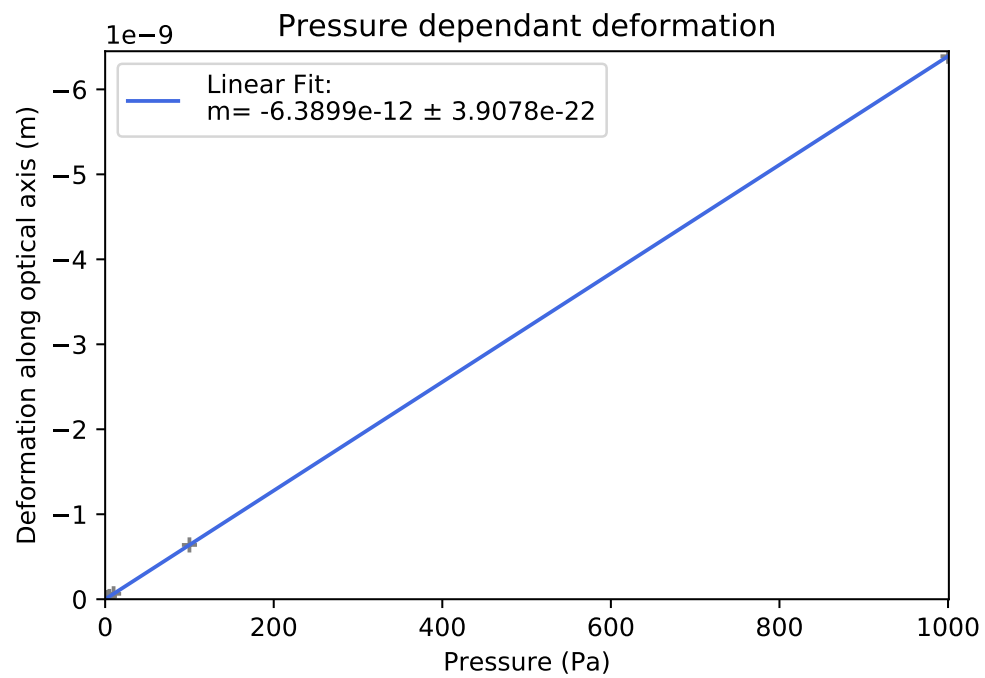


Figure 6.11: Shown is the pressure dependent displacement of the central mirror-point along the optical axis.

### 6.7.2 Experimental determination of the deformation

The pressure induced deformation of a FP-cavity based refractometer is a highly specific to the respective system. It greatly depends on the cavity materials used, potential material defects, the contacting of the mirrors to the resonator and other environmental effects. A theoretical FEM simulation of a pressure induced deformation of the chosen system can therefore only ever be a rough approximation of the actual, physically observable deformation. For a refractometry based pressure standard it is therefore required to experimentally determine the deformation of the system to account for these highly specific effects and not to rely on a FEM-simulation.

The pressure induced deformation of the resonator can be determined experimentally with the so called: Two-gas-method and the following section will be used to illustrate the experimental approach of the method.

A FP based refractometer is used to perform two individual pressure measurements with Helium and Nitrogen. These two gases are chosen because their respective measurement effects (change in beat frequency due to pressure modulation) are different by almost one order of magnitude. The deformation of the cavity mirror however, is independent of the gas species and scales linear with pressure. This observation allows for a clever method to extract the deformation coefficient  $\epsilon_m = \frac{\Delta L}{L_0} / (n - 1)$ , by comparing the two partial pressure measurements of Helium and Nitrogen with each other over a fixed pressure range.

Additionally, Helium and Nitrogen are chosen as measurement gases because their refractivity and density virial coefficients can be theoretically calculated with the uncertainties required for a high precision refractometry based pressure standard. This allows for a comparison of the theoretically expected partial pressure values with the experimentally obtained result for gas pressure and gas density measurements. Since the cavity-length-deformation along the optical axis of the resonator scales linearly with pressure, one can obtain the deformation of the system by looking at the measurement residuals or rather the difference between theory and experiment. Figure 6.12 shows a comparison of the (theoretical) set pressure and the difference:  $\Delta P$  between the set pressure  $P_{set}$  and the experimentally obtained pressure  $P_{meas}$ . If the measurement pressure is not corrected for the deformation of the system, a clear pressure dependent difference between theoretical and experimental pressure can be observed.

The difference  $\Delta P$  increases linearly with pressure for both, Nitrogen and Helium. The deviation originates from the linear deformation of the cavity mirrors due to an increase in measurement pressure. However, the difference  $\Delta P$  between the experimental and theoretical result are around 8 times higher for Helium than for Nitrogen. This is due to the measurement effect being 8 times stronger for Nitrogen than for Helium (see Figure 6.8). As a result, the relative error for Helium is larger in comparison to Nitrogen, since the deformation has a greater relative effect for a smaller overall measurement effect.

To obtain the experimentally determined gas density and pressure from the refractivity measure-

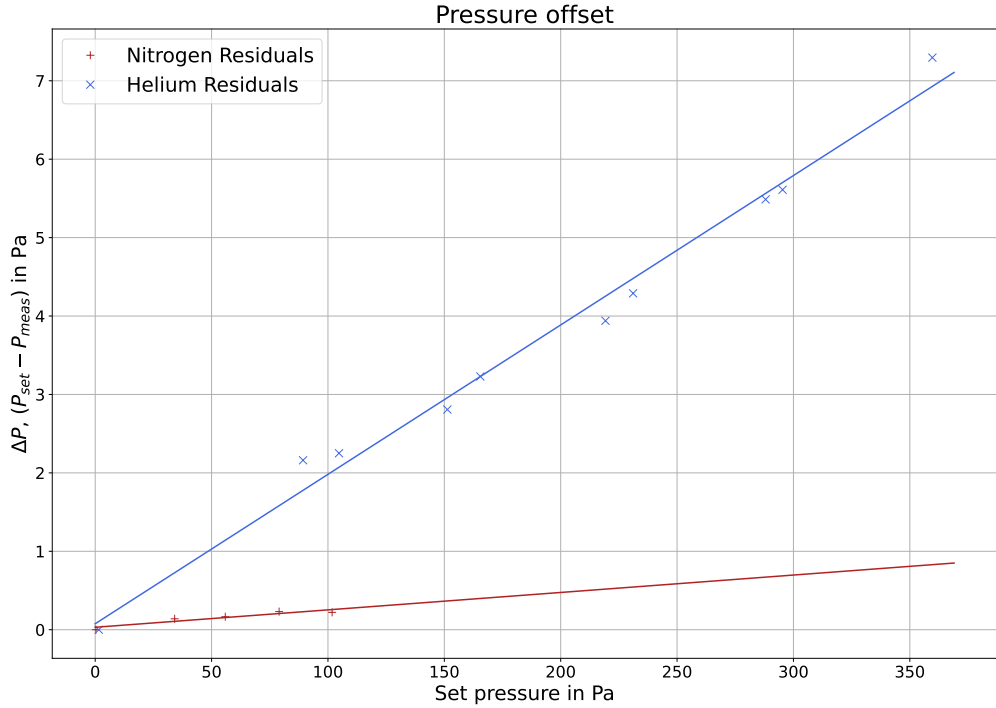


Figure 6.12: Shown is the difference  $\Delta P$  between the experimental and theoretical pressures with respect to the chosen set pressures. This was done for Helium (blue) and Nitrogen gas for set pressures between 0 and 350 Pa.

ments shown in Figure 6.12 the following relations were used:

$$(n-1) = \frac{\frac{\Delta\nu}{\nu_0} + \frac{\Delta q}{q_0}}{1 - \frac{\Delta\nu}{\nu_0} + \epsilon_m} \quad (6.16)$$

$$\rho_{exp} = \frac{2(n-1)}{3A} \cdot \left(1 - \frac{1+4B}{A^2}(n-1)\right) \quad (6.17)$$

$$P_{exp} = RT\rho_{exp} (1 + \rho_{exp} B_\rho) \quad (6.18)$$

with the refractivity virials  $A$  and  $B$ , the density virial  $B_\rho$ , the change in beat frequency:  $\frac{\Delta\nu}{\nu_0}$  and the mode number change:  $\frac{\Delta q}{q_0}$ . The deformation coefficient  $\epsilon_m = \frac{\Delta L}{L_0}/(n-1)$  is unknown at this point and will be determined through the two-gas method.

The theoretical refractivity is determined from the chosen set-pressure and the resulting gas density as follows:

$$P_{set} = \text{const.} \quad (6.19)$$

$$\rho_{theo} = \frac{\sqrt{\frac{4B_\rho P_{set} + RT}{RT}} - 1}{2B_\rho} \quad (6.20)$$

$$(n-1)_{theo} = \frac{A^2 - \sqrt{A^3(-6A^2\rho_{theo} + A - 24B\rho_{theo})}}{2A^2 + 4B} \quad (6.21)$$

To obtain the deformation of the resonator:  $\epsilon_m = \frac{\Delta L}{L_0} / (n - 1)$ , the data from Figure 6.12 is fitted with a linear model for each individual gas. The respective slopes of the linear fits, named  $k_{N_2}$  and  $k_{He}$ , are used to extract the deformation coefficient  $\epsilon_m$  by comparing the two results with each other:

$$\epsilon_m(N_2) = \frac{A_{He}}{A_{N_2}} \left( \frac{k_{He} - k_{N_2}}{1 - \frac{A_{He}}{A_{N_2}}} \right) \quad (6.22)$$

$$\epsilon_m(He) = \frac{k_{He} - k_{N_2}}{1 - \frac{A_{He}}{A_{N_2}}} \quad (6.23)$$

$$\frac{\Delta L}{L_0} = \epsilon_m \cdot (n - 1) \quad (6.24)$$

The following theoretically determined gas parameters were used for the calculation of  $\frac{\Delta L}{L_0}$ :

Gas property:	Helium:	Nitrogen:
Refractivity virial (A) :	$0.52025865 \cdot 10^{-6}$	$4.446107 \cdot 10^{-6}$
Refractivity virial (B):	$15.239 \cdot 10^{-12}$	$0.81 \cdot 10^{-12}$
Density virial ( $B_\rho$ ):	$11.835 \cdot 10^{-6}$	$-5.34 \cdot 10^{-6}$
Gas temperature in Kelvin:	296.15	296.15

Table 6.3: Gas properties of Helium and Nitrogen

and together with the previously obtained mode number shift and Free-Spectral-Range of the cavity, the experimentally determined deformation of the resonator yields:

$$\frac{\Delta L}{L_0} = 7.47 \cdot 10^{-12} m/Pa \quad (6.25)$$

For all future pressure measurements with the given system this experimentally determined deformation factor can be utilized to correct the respective partial pressure measurements. The correction factor can be applied to all partial pressure measurements, independent of the gas species.

## 6.8 Temperature effects: PV-work

aaaa

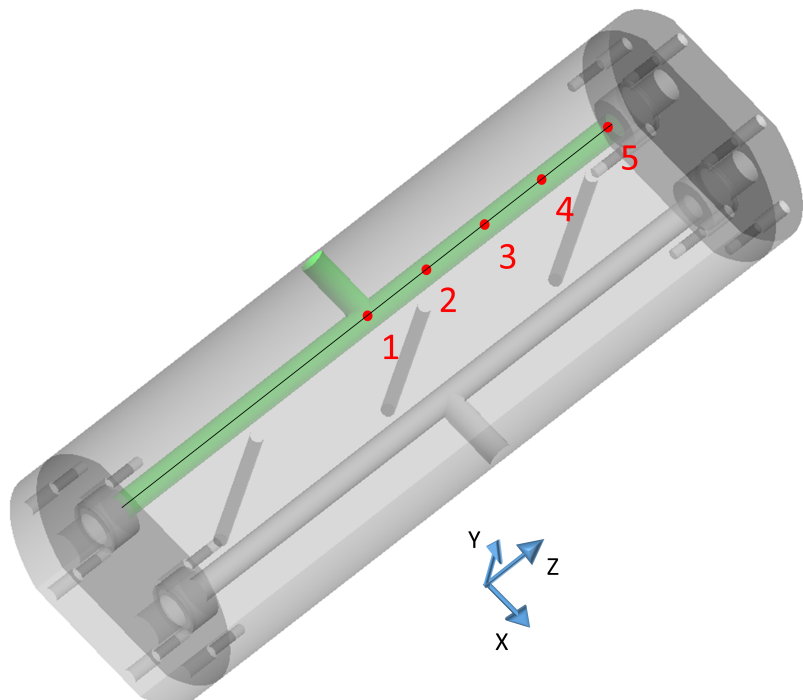


Figure 6.13: .

aaa

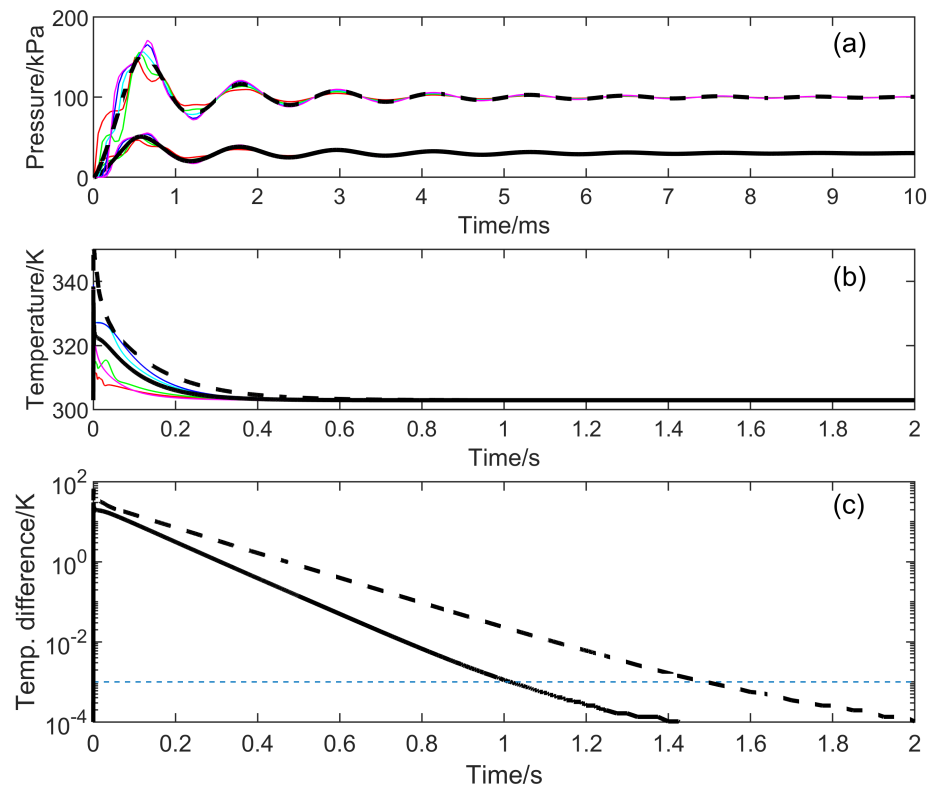


Figure 6.14: .

aaa

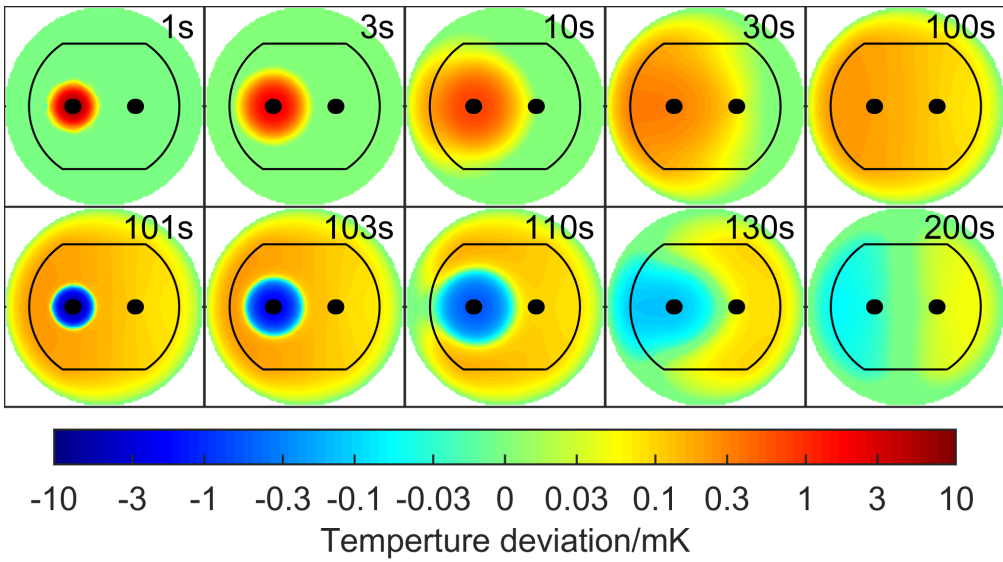


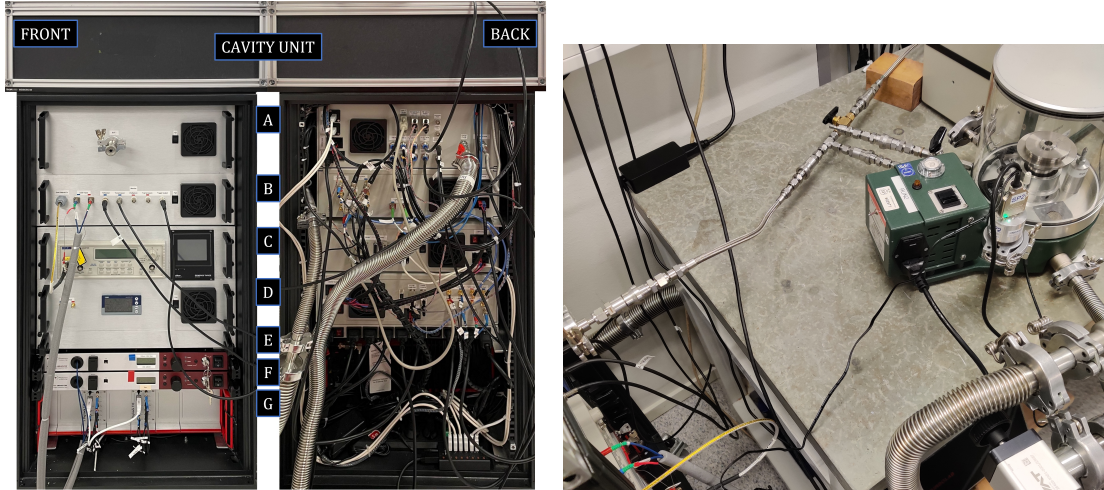
Figure 6.15: .

## 6.9 Ring comparison

Circular comparisons are a tool in metrology to assess the repeatability, longtime performance and measurement uncertainty of pressure standards and other unit defining standards. The comparisons are generally performed internationally between multiple national metrology institutes. One, often times transportable, standard is chosen and directly compared to multiple other stationary standards which are present in the individual NMI's. A pre-defined measurement routine is agreed upon, and the staff members at each institute performs the respective measurements independently. Ultimately, the data is gathered and one can asses if the measurements agree with each other within the set boundaries.

Within the QuantumPascal project, the National metrology institute of Sweden together with the Umea university designed and built a transportable optical pressure standard. To assess the performance of this newly developed, state of the art optical standard a circular comparison was performed. Therefore the transportable optical standard was shipped to all participating NMI's and compared to the local, calibrated piston gauges of the pressure and vacuum laboratories. The combined data was then published in a project report [label] and open access journal [label].

The operating principle of the transportable, optical pressure standard is based on a dual Fabry-Pérot resonator made of Invar combined with a mirror coating for a single wavelengths at 1550 nm. The GAMOR methodology was implemented and the system is able to assess vacuum from 1 Pa up to atmospheric pressure. To accommodate the refractometer for transportation, it was built to fit into a compact 19 inch rack with a 60x60 cm foot print at a height of 120 cm. Figure 6.16a shows a picture of the transportable optical pressure standard (TOP) and Figure 6.16b illustrates the measurement procedure when it is connected to a pressure balance at a NMI.



(a) Transportable optical pressure standard (TOP). (b) Transportable optical pressure standard connected to a pressure balance at a NMI.  
 A) Vacuum connections. B) Measurement unit including beat signals, triggers and Laser lock input.  
 C) Residual pressure monitor. D) Temperature control unit. E and F) 1550 nm fiber Lasers. G) Laser locking electronics.

For the actual comparisons, the TOP was connected to the local piston gauges using ultra high vacuum connectors and the system was flushed with Nitrogen to remove residual gases to preserve gas purity within the resonator. 24 hours of time were required to thermally stabilize the cavity unit before gas density measurements could be performed with the TOP. The piston gauge was then used to set a Nitrogen gas pressure in the cavity by adding weights on top of the piston cylinder. Nine different configurations were chosen to generate pressures between 30 and 80 kPa. After setting the pressure with the piston gauge, several beat measurement were performed with the TOP and converted to gas pressures. Between measurements the system was fully evacuated again.

The upper graphic in Figure 6.17 shows the measurement results for the piston gauges that was available at the optical laboratory of the PTB, while the bottom graphic in 6.17 shows the combined results of all participating members. The set pressure of the piston gauge is plotted against the difference in pressure obtained with the optical refractometer. For a large part of the observed pressure range the agreement is within  $\pm 10$  ppm only at pressures below 10 kPa there are individual outliers for a few systems.

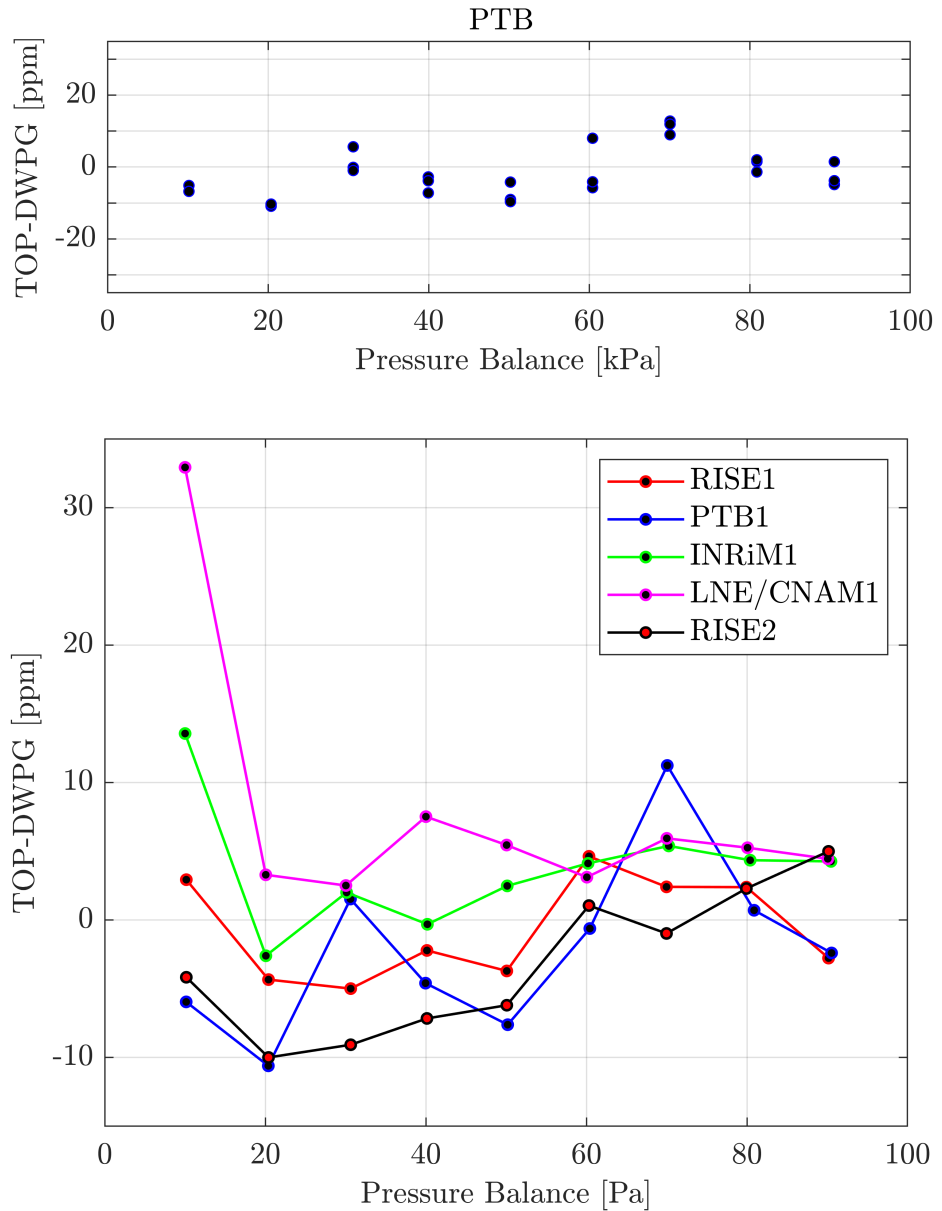


Figure 6.17: At the top: Measurement results obtained at the PTB. At the bottom: combined measurement results of all participating European NMI's.

## 7. Gas permeability measurements of cavity-spacer materials

When high precision measurements of gas refractivities and gas pressures are performed with Fabry-Perot-Cavity based methods, one has to account for the deformation and out gassing of the spacer materials. Often times glass materials like: Ultra-Low-Expansion (ULE) Glass or Zerodur are used as Cavity spacer materials, due to their coefficient of thermal expansion (CTE) having a zero crossing close to room temperature and thus minimizing the temperature dependent deformation of the Cavity at the most common operating temperatures. Glass materials are also easily processed and can be polished effectively to allow direct optical contacting of the mirror substrate and the spacer material. Unfortunately many glasses are often prone to Helium permeation which results in an unwanted, slow change of the overall cavity length depending on the Helium concentration that the system was exposed to, during and before measurements.

### 7.1 Theory

The specific out gassing rate of an approximated infinite plane with  $d \ll a, b$  at a given temperature  $T$ , decays exponentially with time:

$$q_{out} = \frac{4 \cdot D}{d} \cdot c_0 \cdot e^{-\frac{t}{t_{out}}} \quad (7.1)$$

D is a temperature dependent diffusion constant, d is the sample thickness,  $c_0$  describes the initial Helium concentration in the sample and  $t_0$  is a sample specific constant:

$$t_{out} = \frac{d^2}{\pi^2 \cdot D} \quad (7.2)$$

Since gas is released from all sample surfaces simultaneously, the total out gassing rate  $Q_{out}$  can be written as:

$$Q_{out} = 2 \cdot A \cdot q_{out} \quad (7.3)$$

And finally the solubility  $S$  of the material can be determined with Henry's law:

$$S = \frac{c_0}{P_{load}} \quad (7.4)$$

where  $P_{load}$  is the pressure of the gas atmosphere used to load the sample with the respective gas.

## 7.2 Experimental setup and procedure

To measure the out gassing of Zerodur and ULE glass a fully automatic system was build, which allows the simultaneous measurement and loading (gas filling) of different glass samples. The out gassing rates can be determined at different temperature, since all individual sample chambers can be temperature controlled between 0 and 100°Celsius.

Fig.(7.1) shows the basic experimental setup and measurement principle. The system is centered around four compact vacuum chambers which contain the glass samples under investigation. The chambers are integrated into temperature controlled and thermally insulated boxes which can be used to generate measurement environments between 0 and 100°Celsius. The sample chambers are connected to an ionization pressure gauge and a quadrupole mass spectrometer, which is operated to detect the partial Helium pressure inside the vacuum system. A traceable Helium-reference leak is used to calibrate the system. It has an Helium out gassing rate of  $9 \cdot 10^{-9} \frac{\text{mbar}\cdot\text{l}}{\text{s}}$  at 296 Kelvin and therefore the respective thermalised box (Box 2) is kept at room temperature at all times.

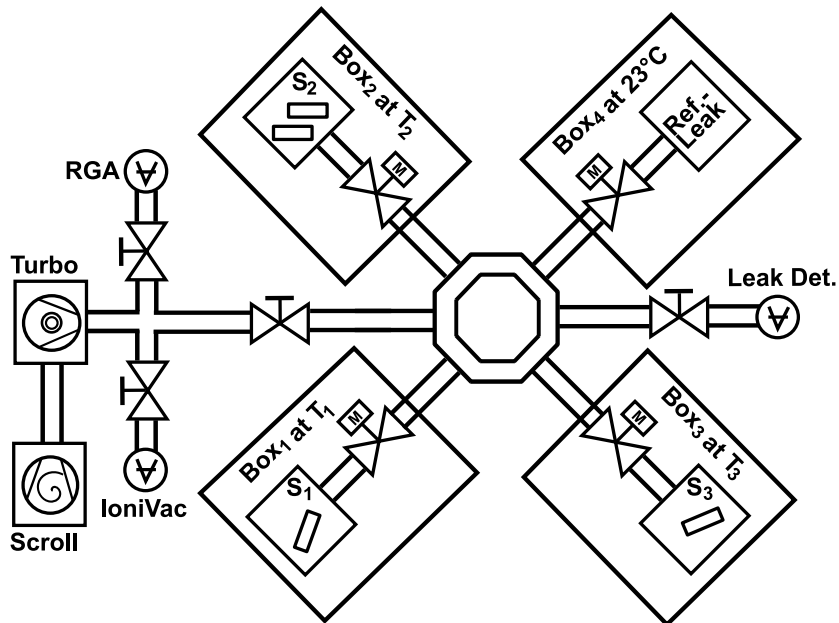


Figure 7.1: .

The remaining three vacuum chambers are used to investigate the out gassing rate of different glass samples. The stainless-steel chambers are conically shaped to minimize the contact between the glass-sample surfaces and the steel of the vacuum chamber. This allows the detection of Helium out gassing from all sample surfaces. The samples, together with the Helium-reference leak, are periodically exposed to the rest of the vacuum system and the quadrupole mass spectrometer by opening and closing electric valves which are directly connected to the individual sample vacuum chambers. By cycling through the measurement chambers one can detect very small out

gassing rates since the gas accumulates inside the sample chamber while the electric valves are closed. The pent-up gas is then released into the vacuum system and can be smoothly detected by the mass spectrometer once the respective electric valve is opened. The periodicity can be adjusted to the individual out gassing rates of the sample as well as the sample size, which both greatly influence the measurement signal detected by the Quadruple mass spectrometer. A greater accumulation time (or measurement period) would generally result in a much higher detected signal and the optimal accumulation time was adjusted before the measurement campaign by trial and error and turned out to be in the order of 200 seconds for the given Zerodur samples.

### 7.2.1 Sample preparation

To load the Zerodur samples with Helium a secondary experimental setup is required (see Fig.7.2). To allow for a throughout permeation of Helium into the glass, the sample chamber is kept under a Helium atmosphere of 5 bars for six weeks before the actual measurement campaign begins. The loading time was chosen based on the out gassing time constant of Zerodur, which was on the order of two weeks. The time constant was experimentally determined in a preliminary experiment. Loading the the glass sample for more than three time constant ensures a fully loaded sample with a small Helium concentration gradient within the sample.

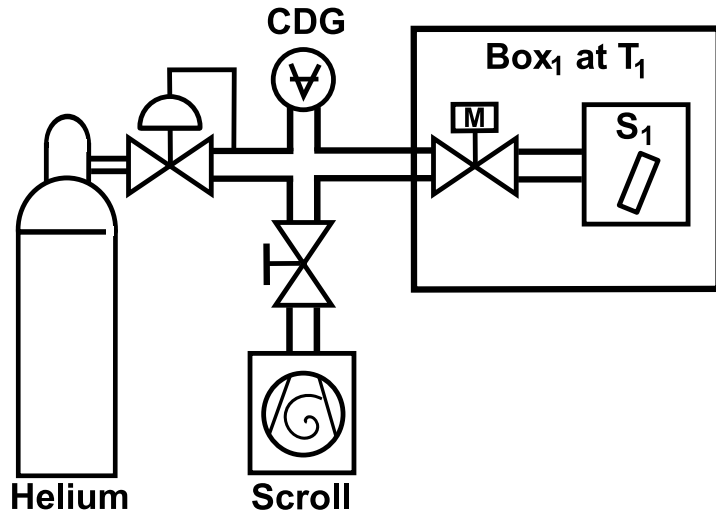


Figure 7.2: .

## 7.3 Experimental results

Fig.7.3 shows the partial Helium pressure (in mbars) measured with the QMS for two consecutive measurement cycles, 50 days after the measurement campaign has begun. One can observe three distinct peaks which indicate the release of the pent-up Helium gas, from the individual sample chambers, into the evacuated vacuum system. The Turbo pump removes the access gas from the

system within 20 seconds and a plateau can be observed, which depends on the individual out gassing rate of the sample (or calibrated Helium Leak) and the pumping speed of the turbo pump which is continuously operating during the experiment. The partial pressure of each plateau is measured for roughly 60 seconds before the respective valve is closed and another sample chamber is opened. After opening the first sample chamber, which contains two identical Zerodur samples, an empty reference chamber is unlocked to determine the out gassing rate of an empty chamber for later offset correction of the measurement signal. The cycle continues with the second measurement chamber opening, which contains one Zerodur sample. The valve is closed and the empty reference chamber is measured again before the cycle concludes with an observation of the reference chamber. Each individual measurement cycle takes 320 seconds to complete and is periodically repeated.

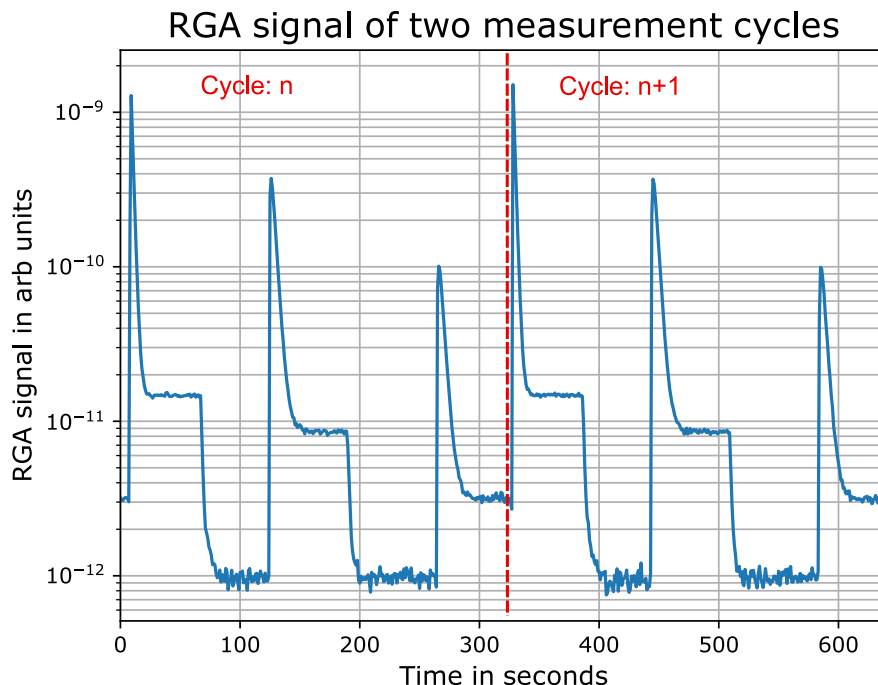


Figure 7.3: .

To determine the out gassing rate of the samples, the measured plateaus were averaged over their respective measurement period and then plotted over time. Fig.7.4 shows the result and the time dependent evolution of the QMS signal for the four connected sample or reference chambers. The second measurement chamber, which contains two identical Zerodur samples, was connected 38 ( one time constant) days after the beginning of the overall measurement campaign. An initial multi-exponential decline of the RGA-signal is observed, while the signal of the chamber containing only one Zerodur-glass sample reached the characteristic mono-exponential He-out-gassing, which can generally be observed after more than one time constants has passed since the beginning of the experiment.

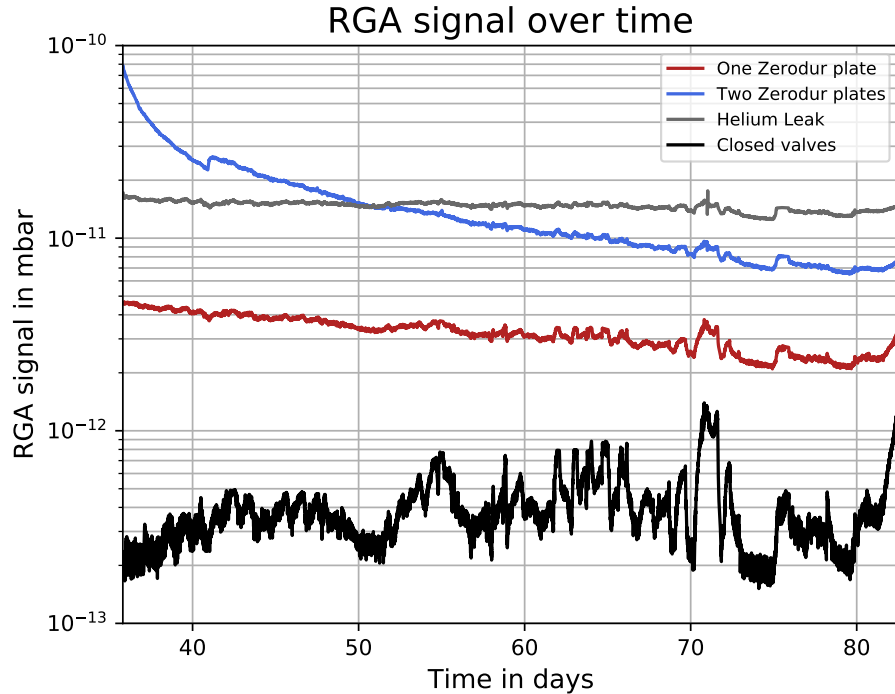


Figure 7.4: .

The respective He-out-gassing rate of the samples can be assessed from the RGA-signals after a normalization and offset correction was performed. The signal of the empty reference chamber was subtracted from the two sample-chamber QMS signals and afterwards normalized with the detected Helium reference leak signal for the respective measurement cycle. The offset-corrected and normalized signal can then be multiplied with the known He-out-gassing rate of the He-Leak to determine the overall He-out-gassing rates of the two respective sample chambers.

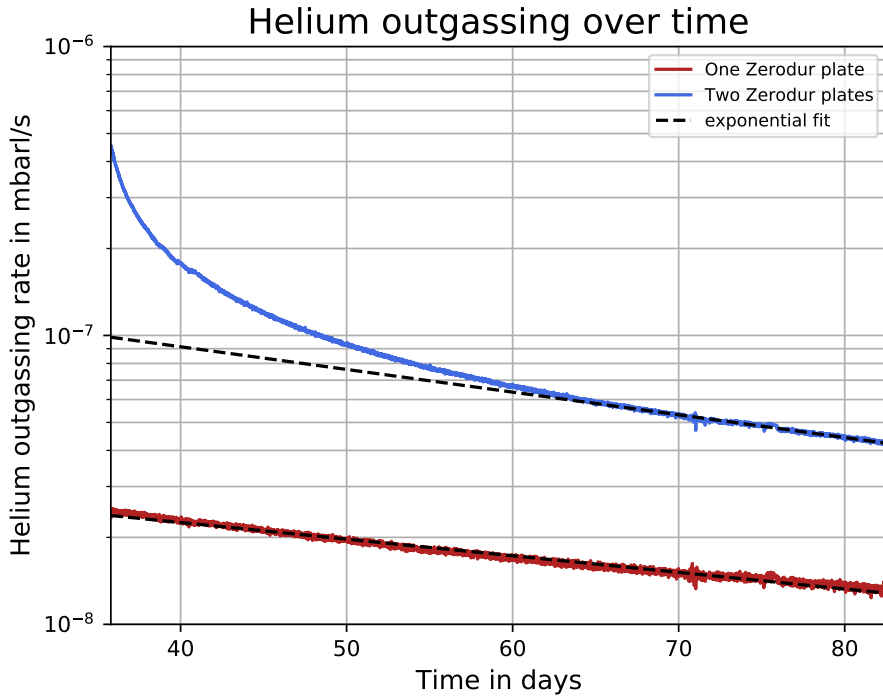


Figure 7.5: .

The exponentially decaying data set can be fitted to determine the time constant  $t_{out}$  and together with eq.(7.2) one can calculate the diffusion constant  $D$  of Zerodur at 23°C. Using eq.(7.1) in combination with the results for  $D$  one can calculate the initial Helium concentration  $c_0$  of the sample and the Solubility  $S$  of the material. Table(7.1) shows the combined results for the Zerodur samples investigated within the first measurement campaign.

Sample name :	$t_{out}$ in days	$Q_{out,(t=0)}$ in Pa m <sup>3</sup> /s	$c_0$ Pa m <sup>3</sup> /m <sup>3</sup>	S in ppm
One Zerodur plate:	35.57	$1.31 \cdot 10^{-5}$	7.144	14.28
Two Zerodur plates:	X	X	X	X

Table 7.1: .

# Bibliography

- [1] B. Argence, C. Daussy, and Y. Coq. “Quantum cascade laser frequency stabilization at the sub-Hz level”. In: *Nature Photonics* (2015). DOI: [10.1038/nphoton201593](https://doi.org/10.1038/nphoton201593).
- [2] Ove Axner et al. “Ability of gas modulation to reduce the pickup of drifts in refractometry”. In: *Journal of the Optical Society of America B* Vol. 38, Issue 8, (2021). DOI: <https://doi.org/10.1364/JOSAB.420982>.
- [3] S. Bartalini et al. “Frequency-comb-referenced quantum-cascade laser at  $4.4 \mu\text{m}$ ”. In: *Optics Letters* 32, No. 8 (2007). DOI: [10.1364/OL.32.000988](https://doi.org/10.1364/OL.32.000988).
- [4] S. Bartalini et al. “Measuring frequency noise and intrinsic linewidth of a room-temperature DFB quantum cascade laser”. In: *Optical Society of America, Optics Express* Vol. 19, Nr. 19 (2011). DOI: <https://doi.org/10.1364/OE.19.017996>.
- [5] Eric D. Black. “An introduction to Pound–Drever–Hall laser frequency stabilization”. In: *American Journal of Physics* 69, 79 (2001). DOI: <https://doi.org/10.1119/1.1286663>.
- [6] Max Born and Emil Wolf. *Principles of Optics*. 1980. ISBN: ISBN0-08-026481-6.
- [7] S. Borri et al. “Tunable Microcavity-Stabilized Quantum Cascade Laser for Mid-IR High-Resolution Spectroscopy and Sensing”. In: *Sensors* 16(2) (2016). DOI: <https://doi.org/10.3390/s16020238>.
- [8] N. Bucalovic, V. Dolgovskiy, and C. Schori. “Experimental validation of a simple approximation to determine the linewidth of a laser from its frequency noise spectrum”. In: *Applied Optics* Vol.51, issue 20 (2014). DOI: <https://doi.org/10.1364/AO.51.004582>.
- [9] F. Cappelli, I. Galli, and S. Borri. “Subkilohertz linewidth room-temperature mid-infrared quantum cascade laser using a molecular sub-Doppler reference”. In: *Optics Letters* Vol.37 No. 23 (2012). DOI: <https://doi.org/10.1364/OL.37.004811>.
- [10] F. Cappelli, I.Galli, and S.Borri. “Subkilohertz linewidth room-temperaturemid-infrared quantum cascade laserusing a molecular sub-Doppler reference”. In: *Optics Letters* Vol. 37, Nr. 23 (2012). DOI: <https://doi.org/10.1364/OL.37.004811>.
- [11] M. Cardilli, M.Dabicco, and F.Mezzapesa. “Linewidth measurement of mid infrared quantum cascade laser by optical feedback interferometry”. In: *Appl. Phys. Lett.* Vol. 108 (2016). DOI: <https://doi.org/10.1063/1.4940116>.
- [12] Shang-Yi Ch'en and Makoto Takeo. “Broadening and Shift of Spectral Lines due to the Pressence of Foreign Gases”. In: *Reviews of Modern Physics* 29.1 (1957). DOI: <https://doi.org/10.1103/RevModPhys.29.20>.
- [13] Antonio Chiarugi et al. “Diode laser-based gas analyser for the simultaneous measurement of CO<sub>2</sub> and HF in volcanic plumes”. In: *Athmospheric Measurement Techniques* 11, 329–339 (2018). DOI: <https://doi.org/10.5194/amt-11-329-2018>.

- 
- [14] M. Siciliani de Cumis et al. "Microcavity-Stabilized Quantum Cascade Laser". In: *Laser and Photonics Reviews* 10, No. 1, 153-157 (2016). DOI: 0.1002/lpor.201500214.
  - [15] Mario Siciliani de Cumis, Simone Borri, and Giacomo Insero. "Microcavity-Stabilized Quantum Cascade Laser". In: *Laser Photonics Rev.* Vol.10 No. 1 (2016). DOI: DOI10.1002/lpor.201500214.
  - [16] W. Demtröder. *Laserspektroskopie 1*. 2011. DOI: 10.1007/978-3-642-21306-9.
  - [17] W. Demtroeder. *Experimentalphysik 3 Atome, Moleküle und Festkörper (5.Auflage)*. 2015. DOI: 10.1007/978-3-662-49094-5.
  - [18] Y. Deng et al. "Narrow linewidth characteristics of interband cascade lasers". In: *Applied Physics Letters* Vol.116 (2020). DOI: <https://doi.org/10.1063/5.0006823>.
  - [19] G. Di Domenico, S. Schilt, and P. Thomann. "Simple approach to the relation between laser frequency noise and laser line shape". In: *Applied Optics* Vol. 49, issue 25 (2010). DOI: <https://doi.org/10.1364/AO.49.004801>.
  - [20] Gianni Di Domenico, Stéphane Schilt, and Pierre Thomann. "Simple approach to the relation between laser frequency noise and laser line shape". In: *Applied Optics* Vol.49 issue 25 (2010). DOI: <https://doi.org/10.1364/AO.49.004801>.
  - [21] R.W.P. Drever et al. "Laser Phase and Frequency Stabilization Using an Optical Resonator". In: *Applied Physics B Photophysics and Laser Chemistry* 31, 97-105 (1983). DOI: 10.1007/BF00702605.
  - [22] Richard Engeln et al. "Cavity enhanced absorption and cavity enhanced magnetic rotation spectroscopy". In: *Review of Scientific Instruments* 69 (1998). DOI: <https://doi.org/10.1063/1.1149176>.
  - [23] Jerome Faist. *Quantum Cascade Lasers*. 2018. DOI: 10.1093/acprof:oso/9780198528241.001.0001.
  - [24] Jerome Faist et al. "Quantum Cascade Laser". In: *Science* 264.5158, 553-556 (1994). DOI: 10.1126/science.264.5158.553.
  - [25] E. Faschi et al. "Narrow-linewidth quantum cascade laser at 8.6  $\mu\text{m}$ ". In: *Optics Letters* 39, No. 16 (2014). DOI: <http://dx.doi.org/10.1364/OL.39.004946>.
  - [26] Eugenio Faschi, Nicola Coluccelli, and Marco Cassinero. "Narrow-linewidth quantum cascade laser at 8.6  $\mu\text{m}$ ". In: *Optics Letters* Vol.39 No. 16 (2014). DOI: <https://doi.org/10.1364/OL.39.004946>.
  - [27] Adam J. Fleisher et al. "Twenty-five-fold reduction in measurement uncertainty for a molecular line intensity". In: *IEEE Transactions on Instrumentation and Measurement* 123.4 (2019). DOI: 10.1103/PhysRevLett.123.043001.
  - [28] S. Haefner et al. "8 \* 10e17 fractional laser frequency instability with a long room-temperature cavity". In: *Optics Letters* Vol. 40, No. 9 (2015). DOI: <https://doi.org/10.1364/OL.40.002112>.
  - [29] Jean-Michel Hartmann, Ha Tran, and Raymond Armante. "Recent advances in collisional effects on spectra of molecular gases and their practical consequences". In: *Journal of Quantitative Spectroscopy and Radiative Transfer* (2018). DOI: <https://doi.org/10.1016/j.jqsrt.2018.03.016>.
  - [30] H. Haug and S.W.Koch. *Quantum theory of the optical and electronical properties of semiconductors*. 2009. DOI: <https://doi.org/10.1142/7184>.

- [31] A. Hugi et al. “Mid-infrared frequency comb based on a quantum cascade laser”. In: *Nature* 492, pages 229–233 (2012). DOI: doi:10.1038/nature11620.
- [32] J. Setina. “New approach to corrections for thermal transpiration effects in capacitance diaphragm gauges”. In: *Metrologia* Volume 36, No.6 (1999). DOI: DOI10 . 1088 / 0026 - 1394/36/6/27.
- [33] K. Jousten. *Handbook of Vacuum Technology*. 2016. DOI: <https://doi.org/10.1002/9783527688265.ch11>.
- [34] K. Jousten, J. Hendricks, and D. Barker. “Perspective for a new realization of the Pascal by optical methods”. In: *Metrologia* Volume 54, No.6 (2017). DOI: doi:10.1088/1681-7575/aa8a4d.
- [35] J. Kischkat et al. “Mid-infrared optical properties of thin films of aluminum oxide, titanium dioxide, silicon dioxide, aluminum nitride, and silicon nitride”. In: *Applied Optics* 51,28, 6789-6798 (2015). DOI: 10.1364/AO.51.006789.
- [36] W. Lauterborn. *Coherent Optics - Fundamentals and Applications*. 2003. ISBN: 3-540-43933-1.
- [37] Henry Margenau and William W. Watson. “Pressure Effects on Spectral Lines”. In: *Reviews of Modern Physics* 8 (1936). DOI: <https://doi.org/10.1103/RevModPhys.8.22>.
- [38] S. Mathonniere et al. “External cavity quantum cascade laser emitting from 12.3 to 13.2  $\mu\text{m}$ ”. In: *Applied Physics B Lasers and Optics* 124:149 (2018). DOI: <https://doi.org/10.1007/s00340-018-7017-7>.
- [39] N. Mukherjee, R. Go, and C. Patel. “Linewidth measurement of external grating cavity quantum cascade laser using saturation spectroscopy”. In: *Applied Physics Letters* Vol. 92 (2008). DOI: <https://doi.org/10.1063/1.2901038>.
- [40] H. Ngo et al. “Spectral shapes of rovibrational lines of CO broadened by He, Ar, Kr and SF<sub>6</sub>: A test case of the Hartmann-Tran profile”. In: *Journal of Quantitative Spectroscopy and Radiative Transfer* 203 (2017). DOI: <https://doi.org/10.1016/j.jqsrt.2017.03.001>.
- [41] N.H. Ngo, D. Lisak, and H. Tran. “An isolated line-shape model to go beyond the Voigt profile in spectroscopic databases and radiative transfer codes”. In: *Journal of Quantitative Spectroscopy and Radiative Transfer* Vol.129 (2013). DOI: <https://doi.org/10.1016/j.jqsrt.2013.05.034>.
- [42] Gerardo J. Padilla-Víquez et al. “Traceable CO<sub>2</sub>-R(12) Line Intensity for Laser-Spectroscopy-Based Gas Analysis Near 2  $\mu\text{m}$ ”. In: *IEEE Transactions on Instrumentation and Measurement* 56.2 (2007). DOI: 10.1109/TIM.2007.891160.
- [43] Edson R. Peck and Baij Nath Khanna. “Dispersion of Nitrogen”. In: *Journal of the Optical Society of America* Volume 56, Issue 8 (1966). DOI: <https://doi.org/10.1364/JOSA.56.001059>.
- [44] L.S. Rothman R.V. Kochanov I.E. Gordon. “HITRAN Application Programming Interface (HAPI): A comprehensive approach to working with spectroscopic data”. In: *J. Quant. Spectrosc. Radiat. Transfer* Vol.177 (2016). DOI: <https://doi.org/10.1016/j.jqsrt.2016.03.005>.
- [45] D. Romanini and K. K. Lehmann. “Ring-down cavity absorption spectroscopy of the very weak HeN overtone bands with six, seven, and eight stretching quanta”. In: *The Journal of Chemical Physics* 264, 316-322 (1993). DOI: <http://dx.doi.org/10.1063/1.465866>.
- [46] D. Romanini et al. “CW cavity ring down spectroscopy”. In: *Chemical Physics Letters* 264, 316-322 (1997). DOI: 10.1016/S0009-2614(96)01351-6.

- [47] L.S. Rothman et al. “The HITRAN2012 molecular spectroscopic database”. In: *Journal of Quantitative Spectroscopy and Radiative Transfer* 130, 4-50 (2013). DOI: <https://doi.org/10.1016/j.jqsrt.2013.07.002>.
- [48] L.S. Rothman et al. “The HITRAN2016 molecular spectroscopic database”. In: *Journal of Quantitative Spectroscopy and Radiative Transfer* 203, 3-69 (2017). DOI: <https://doi.org/10.1016/j.jqsrt.2017.06.038>.
- [49] I. Sergachev. Rubin. “High-Power and Narrow-Linewidth Optimizations of Mid-Infrared Quantum Cascade Lasers”. 2017. DOI: doi:10.5451/unibas-006771214.
- [50] T. Rubin. “Praezise Partialdruckbestimmung bei der Atemgasanalyse und in der Metrologie”. 2016. DOI: <http://dx.doi.org/10.17169/refubium-6520>.
- [51] A. L. Schawlow and C. H. Townes. “Infrared and Optical Masers”. In: *Physical Review* Vol.112 (1940). DOI: <https://doi.org/10.1103/PhysRev.112.1940>.
- [52] I. Sergachev et al. “All-electrical frequency noise reduction and linewidth narrowing in quantum cascade lasers”. In: *Optics Letters* Vol. 39, issue 23 (2014). DOI: DOI:10.1364/OL.39.006411.
- [53] R. M. Sevast'yanov and R. A. Chernyavskaya. “Virial coefficients of nitrogen, oxygen, and air at temperatures from 75 to 2500 K”. In: *Journal of engineering physics* Volume 51 (1986). DOI: <https://doi.org/10.1007/BF00871372>.
- [54] A. Shehzad, P. Brochard, and R. Matthey. “10 kHz linewidth mid-infrared quantum cascade laser by stabilization to an optical delay line”. In: *Optics Letters* 44,14/15 (2019). DOI: <https://doi.org/10.1364/OL.44.003470>.
- [55] Atif Shezad, Pierre Brochard, and Renaud Matthey. “10 kHz linewidth mid-infrared quantum cascade laser by stabilization to an optical delay line”. In: *Optics Letters* Vol.44 No. 14 (2019). DOI: <https://doi.org/10.1364/OL.44.003470>.
- [56] T. Takaishi and Y. Sensui. “Thermal Transpiration Effect of Hydrogen, Rare Gases and Methane”. In: *Transactions of the Faraday Society* Volume 59 (1963). DOI: <https://doi.org/10.1039/TF9635902503>.
- [57] M.S. Taubman et al. “Frequency stabilization of quantum-cascade lasers by use of optical cavities”. In: *Optics Letters* 27, No. 24 (2002). DOI: 10.1364/OL.27.002164.
- [58] L. Tombez et al. “Linewidth of a quantum-cascade laser assessed from its frequency noise spectrum and impact of the current driver”. In: *Applied Physics B: Lasers and optics* 109.3, 407-414 (2012). DOI: <https://doi.org/10.1007/s00340-012-5005-x>.
- [59] L. Tombez et al. *Physical Origin of Frequency Noise and Linewidth in Mid-IR DFB Quantum Cascade Lasers*. 2013. DOI: [https://doi.org/10.1364/CLEO\\_SI.2013.CM1K.3](https://doi.org/10.1364/CLEO_SI.2013.CM1K.3).
- [60] V. Weisskopf. “Zur Theorie der Kopplungsbreite und der Stoßdämpfung.” In: *Zeitschrift für Physik* 75, 287–301 (1932). DOI: <https://doi.org/10.1007/BF01341858>.
- [61] John U. White. “Long Optical Paths of Large Aperture”. In: *Journal of the Optical Society of America* Vol. 32, Issue 5, (1942). DOI: <https://doi.org/10.1364/JOSA.32.000285>.
- [62] Piotr Zalicki and Richard N. Zare. “Cavity ring-down spectroscopy for quantitative absorption measurements”. In: *Journal of Chemical Physics* 102, 2708 (1998). DOI: <https://doi.org/10.1063/1.468647>.